2018

Trochoidal Milling of AlSiCp with CVD Diamond Coated End Mills

Tony Nguyen
University of the Pacific, t.nguyen9419@gmail.com

Recommended Citation

TROCHOIDAL MILLING OF AlSiC$_p$ WITH CVD DIAMOND COATED END MILLS

by

Tony Nguyen

A Thesis Submitted to the

Graduate School

In Partial Fulfillment of the

Requirements for the Degree of

MASTER OF SCIENCE

School of Engineering and Computer Science
Engineering Science

University of the Pacific
Stockton, CA

2018

TROCHOIDAL MILLING OF AlSiC$_p$ WITH CVD DIAMOND COATED END MILLS

by

Tony Nguyen

APPROVED BY:

Dissertation Advisor: Jiancheng Liu, Ph. D

Committee Member: JuEun Lee, Ph.D.

Committee Member: Kyle Watson, Ph.D.

Department Chair: Chi-Wook Lee, Ph.D.

Interim Dean of Graduate School: Thomas H. Naehr, Ph.D.

TROCHOIDAL MILLING OF AlSiC$_p$ WITH CVD DIAMOND COATED END MILLS

Copyright 2018

by

Tony Nguyen

DEDICATION

This thesis is dedicated to my parents who supported me throughout my academic career and who instilled me with the necessary work ethic to accomplish all my goals. Mr. Evans, my high school Physics teacher, who inspired me to become an engineer and seek lifelong learning.

ACKNOWLEDGMENTS

Trochoidal Milling of AlSiC$_p$ with CVD Diamond Coated End Mills

Abstract

by Tony Nguyen

University of the Pacific
2018

Metal matrix composites have seen a rise in demand within the last decade. Aluminum alloy reinforced with silicon carbide particles is a type of particle metal matrix composite that has seen applications in the aerospace, ground transportation, and electronics industry. However, the abrasive SiC particles have made this material difficult to machine through conventional machining strategies. This research will focus on using computer aided manufacturing with trochoidal tool paths to maximize machining productivity and extend the tool life of CVD diamond coated end mills. The focus of this research will be on AlSiC$_p$ with a high volume fraction of reinforcement (30%) to expand the potential applications of this pMMC. The cutting experiments are divided into three parts: cutting test, confirmation test, and endurance test. Taguchi method will be used to perform an analysis of variance and signal-to-noise ratio to optimize a combination of material removal rate, average cutting forces, and surface roughness values. The optimal cutting conditions were found to be 254 mm/min, 30°, and 9500 r/min for

MRR+AvgFxy+Ra, 1524 mm/min, 30°, and 9500 r/min for MRR+AvgFxy, and 1524 mm/min, 90°, and 9500 r/min. The cutting conditions for MRR+AvgFx+Ra was not considered for the endurance tests as the machining productivity was too low to be considered a feasible option in the industry. It was concluded that trochoidal milling under wet cutting conditions produced nearly half the tool wear as previous research with conventional milling strategies. However, the longer the CVD diamond coated end mills were engaged in the $AlSiC_p$ workpiece, the more dominant the abrasive wear mechanisms appear and cause tool damage. It was concluded that square end mills may not be suitable for machining $AlSiC_p$ and that future research should focus on varying the tool geometry or utilizing ball end mills.

TABLE OF CONTENTS

LIST OF TABLES

LIST OF FIGURES

Chapter 1: Introduction

1.1. Research Motivation

There is high demand for new materials that can satisfy many application requirements and still be cost effective. Metal matrix composites (MMC) is one of the solutions that was created out of this high demand. Metal matrix composites first began in the Cold War era where advanced military systems saw a need for research in new materials for improved performance. This research produced materials that had high strength-to-weight ratio, enhanced mechanical and thermal properties, improved fatigue and creep resistance, higher wear resistance, and tailorable properties. However, MMCs saw a decline in interest in the 1970's due to the recession, which limited funding for research and development; a time when MMCs was still in its infancy. There was a shift from a military concentration to a more fiscally constrained strategy to improve and rebuild existing systems. Fortunately, particle reinforced metal matrix composites (pMMC) renewed the interest in MMCs because of its affordability and ease of processing compared to fiber reinforced metal matrix composites. This allowed many commercial applications to process and experiment with a variety of different products. This interest continued throughout the decades until the MMC market in 1999 accounted for 2500 metric tons valued at $100 M [1,2]. Chawla et al. discusses the growing usage of MMCs from 2001 to 2010 across different market sectors, as shown in Figure 1. It was estimated in a 2006 study that the MMC market will grow from 3.6 million kg in 2005 to 4.9 million kg in 2010 [2].
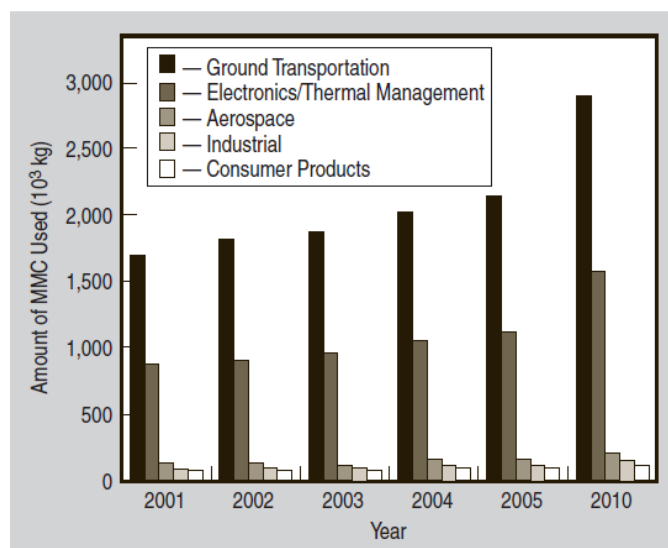
Figure 1. The use of MMCs used across different market sectors from 2001 to 2010 [2].

The continued rise in popularity of pMMCs have yielded extensive studies for the applications in the aerospace, ground transportation, and electronics industries, as discussed by [1−10]. These applications have given rise to many different processing methods. In most cases, these processing methods can be split up into two categories: casting processes and machining processes. Casting processes for aluminum alloy reinforced with silicon carbide particles (AlSiC$_p$) are mainly done via powder metallurgy, high-pressure infiltration, and stir casting. These casting processes can produce complex geometries and near net shape products. The goals of these casting processes is to produce a uniform distribution of silicon carbide (SiC) particle reinforcement, have good wettability between the Al and SiC, eliminate or minimize porosity, and eliminate or minimize excess compounds from chemical reactions [1,11]. However, casting processes creates deformations that have varying geometries and unwanted dimensional stability. This product would need machining to obtain dimensional and geometrical precision as well as

a good surface finish. Machining processes are essential for this type of material in order to be successfully applied in the industry [12–16].

Machining processes can be divided into three categories: turning, non-conventional machining, and end milling operations. Turning operation is the oldest type of machining process and the simplest because it involves a single point contact between the cutting tool and the workpiece. Non-conventional machining methods includes electro discharge machining (EDM), laser cutting, and abrasive water jet (AWJ) machining. These methods were created to produce more complex geometries with higher dimensional tolerances than the conventional machining practices. End milling is a more recent machining process that evolved from turning operations. This process uses multi-tooth cutting tools to produce complex geometries through interrupted cuts. A majority of research on machining AlSiC$_p$ is through orthogonal cutting or non-conventional machining at low volume fractions of SiC reinforcement. Research on milling AlSiC$_p$ at high volume fractions (>25%) of particle reinforcement is limited. Milling is an important machining process to study because many complex geometries require a milling operation to create the desired features that cannot be obtained through turning or non-conventional methods.

There has been some success in milling AlSiC$_p$ with 30% volume fraction of SiC reinforcement performed at University of the Pacific by Vargas et al.. Their research concluded that AlSiC$_p$ with 30% volume fraction of SiC particles can be machined with chemical vapor deposition (CVD) diamond coated tools. However, when machining this type of pMMC, extreme flank wear was observed due to the abrasive particles hitting the cutting edge. Additionally, when milling AlSiC$_p$ for an extended period of time, built up

edge (BUE) was observed, which led to early tool failure [17]. Vargas et al. attributed their machinability of $AlSiC_p$ to their cutting parameters and the CVD diamond coated end mills. The type of cutting tool used is an important factor for machining this type of material. Traditional cutting tools like high speed steel (HSS) and carbide have been shown to experience rapid tool wear when machining the abrasive particles in the pMMC. Most researchers recommend using diamond cutting tools because of its high hardness and abrasion resistance [12,14]. On the Mohs Hardness Scale, diamond is the hardest material with a rating of 10, whereas silicon carbide has a rating of 9.5. In order to effectively machine $AlSiC_p$, diamond cutting tools are required.

There is a need for further research on milling $AlSiC_p$ with a high volume fraction of SiC reinforcement (>25%). The results from Vargas et al. has set a premise for developing a more efficient machining process for milling operations on pMMCs. It has been proven that CVD diamond coated end mills have the ability to machine high volume fractions of $AlSiC_p$. However, to improve the process, the tool geometry, coating thickness, and machining strategy must be changed to extend the tool life. Additionally, all cutting operations will be performed under wet-cutting conditions. Even though, many researchers have described coolant as a detrimental factor in machining pMMCs, coolant has been known to extend tool life for many monolithic materials. The change in tool geometry, coating thickness, and machining strategy opens the possibility of maximizing the coolant's capabilities.

1.2. Research Objective

In order to expand the potential applications of $AlSiC_p$, more research is needed on high volume fractions of SiC reinforcement through the milling process. As a result, understanding the interactions of the workpiece and cutting tool is essential. Based on previous research performed by Vargas et al., CVD diamond coated end mills were determined to be suitable for machining $AlSiC_p$. However, more research is needed to understand the cutting interaction between CVD diamond coated end mills and $AlSiC_p$ at high volume fractions.

The purpose of this study it to improve the machining efficiency and the quality of products by utilizing high speed machining (HSM). High speed machining uses a reduced width of cut with increased chip load, higher cutting speeds, and higher feed rate for improved productivity, while maintaining low tool wear [18]. One particular strategy from HSM is to change the tool path from a linear cutting motion to a trochoidal tool path. Then, Vargas et al.'s data can be analyzed and used as a guideline to create a design of experiment. Aluminum alloy reinforced with silicon carbide particles at 30% volume fraction will be use as samples and milled with CVD diamond coated end mills under wet-cutting conditions.

The feed rate, engagement angle, and cutting speed will be varied and the cutting forces will be recorded via a dynamometer. After the cutting tests, the cutting tools and samples will be examined under a 3D microscope and surface roughness tester. The cutting forces will be compared to chipload, material removal rate, and surface roughness. Taguchi method will be used to provide a comprehensive analysis on the influence of each cutting parameter with respect to productivity, cutting forces, and surface integrity by using

analysis of variance (ANOVA) and signal-to-noise (S/N) ratio. The following objectives are:

1. Provide background on $AlSiC_p$.

2. Determine the machining conditions.

3. Experiment using DOE and trochoidal milling.

4. Analyze cutting forces, tool wear, and surface quality.

5. Perform endurance experiments under wet cutting conditions.

This research aims to extend the tool life of CVD diamond coated end mills and make them a more cost effective method to traditional and other diamond cutting tools. Research is conducted at University of the Pacific's Computer Integrated Manufacturing Systems (CIMS) laboratory.

Chapter 2: Background

2.1. Metal Matrix Composites

Metal matrix composites have been known to give improved strength, stiffness, thermal conductivity, abrasion resistance, creep resistance, or dimensional stability in comparison to many monolithic materials. Additionally, unlike resin-matrix composites, they are nonflammable, unaffected in a vacuum chamber, and suffer minimal organic attacks [19]. The major benefit of MMCs is its ability to be tailored to specific applications by changing its constituent materials. Metal matrix composites is categorized as fiber reinforced or particle reinforced which is also known as continuously or discontinuously reinforced, respectively. The most common metal matrix used includes aluminum, titanium, magnesium, or copper. This metal matrix imparts metallic properties such as thermal and electrical conductivity. The reinforcement usually consists of a ceramic or polymer material that aims to reduce weight or improve material properties. For fiber reinforced MMCs, reinforcements can include graphite, silicon carbide, boron, aluminum oxide, or refractory metals. Particle reinforced MMCs can include silicon carbide whiskers or particles, Al_2O_3, titanium diboride, or graphite [19]. Figure 2 illustrates both fiber and particle reinforced MMCs with varying sizes and volume fractions.
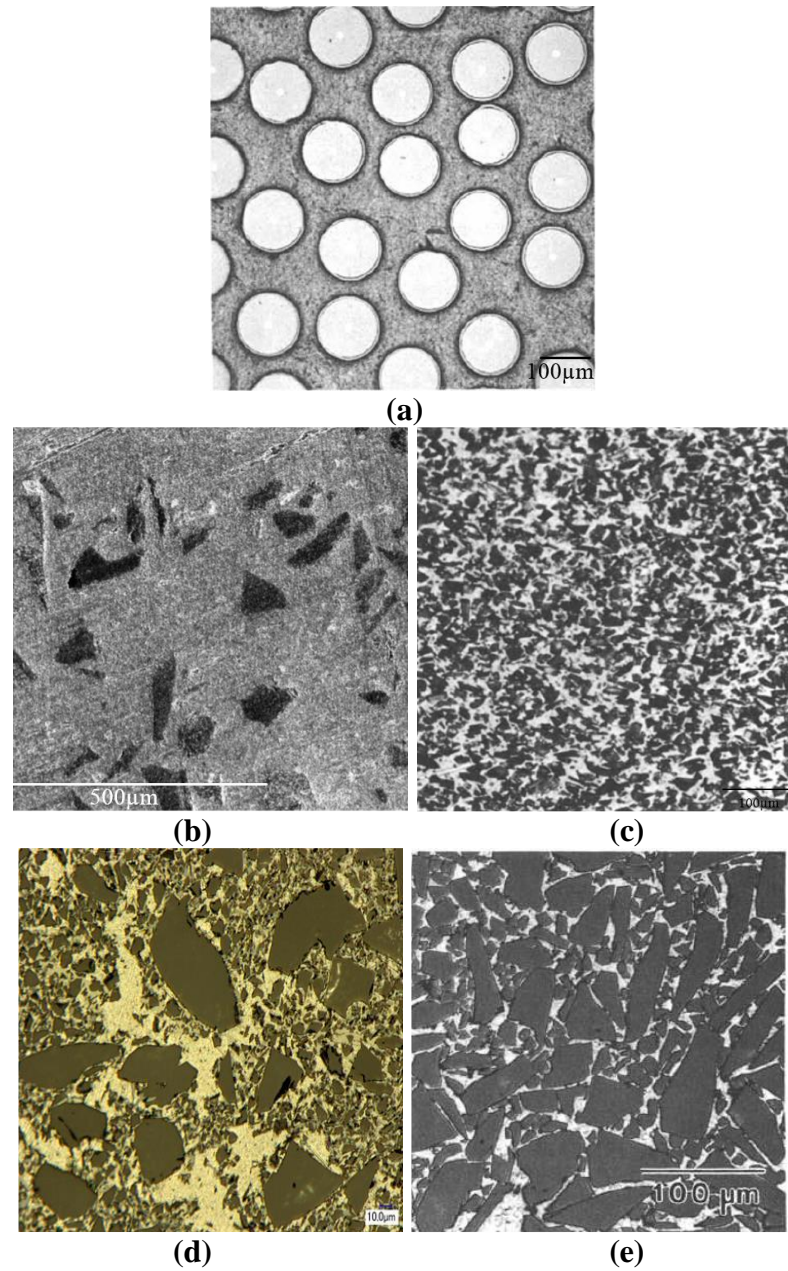
Figure 2. (a) Cross section of fiber reinforced MMC (b) AlSiC$_p$ 30% vol. fraction (c) AlSiC$_p$ 40% vol. fraction (d) AlSiC$_p$ 60% vol. fraction (e) AlSiC$_p$ 81% vol. fraction [19].

Aluminum alloy reinforced with SiC particles will be the focus of this research because pMMCs have been shown to be competitive in specific strength and affordability [1]. Moreover, aluminum is a popular material that is replacing many steel and cast iron based applications. The melting point of aluminum makes it convenient for processing and

high enough to satisfy many application requirements. It is also compatible with many different types of reinforcements, such as SiC particles [19].

2.2. AlSiC$_p$ Material Properties

Table 1. Comparison of AlSiC$_p$ MMC material properties, courtesy of Ferrotec. Shaded area represents desired properties.

Material & Material Code		MMC		Silicon Carbide	Comparisons		
		Casting	Infiltration				
		SA301 and AlSiC 9	SA701	SC902	Aluminum	Cast Iron	Stainless Steel
Composition	Vol.%	30-60% SiC	70% SiC	Purity: 97%	7075	FC250	SUS304
Density	g/cm^3	2.8-3.01	3.0	3.1	2.8	7.3	7.9
Flexural Strength	MPa	471-488	340	490	-	-	-
Young's Modulus	GPa	125-188	260	420	70	210	210
Poisson's Ratio	-	0.29	0.20	-	0.34	0.33	0.33
Thermal Expansion	10^{-6}/K	14-8	7	4.3	23.3	17.3	17.3
Thermal Conductivity	W/m · K	150-190	160	170	130	15	15
Specific Heat	J/g · K	0.8-0.741	0.6	-	1	0.6	0.6
Electrical Resistivity	Ohm · cm	1e^{-5}	1e^{-5}	1e^{-4}	3e^{-6}	7e^{-5}	7e^{-5}
Shear Modulus	GPa	69-76	x	x	x	x	x

Aluminum alloy reinforced with SiC particles has a unique set of material properties that makes it ideal for various applications that require high dimensional stability and good specific strength. Table 1 shows a comparison of AlSiC$_p$ material properties to aluminum 7075, cast iron FC250, and stainless steel SUS304, provided courtesy of Ferrotec. This set of data shows AlSiC$_p$ produced by two different processing methods which resulted in different material properties. The infiltration process had a higher SiC volume content but had a lower flexural strength than the casted AlSiC$_p$ with a 30% SiC

volume fraction. This is important for manufacturers as it determines the preferred processing method for their applications.

When comparing $AlSiC_p$ to aluminum, cast iron, and stainless steel, $AlSiC_p$ has been shown to have a higher strength-to-weight ratio. The two properties that are the most important for $AlSiC_p$ are the coefficient of thermal expansion (CTE) and thermal conductivity, which are in the shaded region. These properties show that $AlSiC_p$ has a CTE of 14×10^{-6}/K or less and a thermal conductivity of 150 W/m·K or more. Aluminum alloy reinforced with SiC particles has a CTE that is nearly more than half of many of its competing materials and has a higher thermal conductivity. This shows $AlSiC_p$ being ideal for heat dispersion in high heated areas while maintaining dimensional stability.

A study from Foltz et al. found that if the size, volume fraction, distribution of the particle reinforcement, and bonding with the matrix were the same, then the strength of the $AlSiC_p$ between different casting processes would be the same. However, this is not the case for many current casting methods. It is important to determine the differences between each processing method to properly analyze the workpiece samples. What determines the strengthening mechanisms in a MMC is direct and indirect strengthening. Under an applied load, the load is transferred from the weaker matrix across the matrix-reinforcement interface and into the reinforcement [20]. This can be considered dispersion strengthening as the SiC particles are strengthening the composite by carrying most of the load. Indirect strengthening develops from the cooling of the MMC which forms dislocations at the matrix-reinforcement interface due to thermal mismatch. These dislocations allows for precipitation and strain hardening and increases with increasing SiC content [20]. However, increasing the SiC content has also been shown to create more pores which

weaken the material's strength. These pores usually develop due to trapped air or imperfections during the casting process of $AlSiC_p$ [21]. Additionally, it was shown through finite element analysis that areas of high clusters tended to have more local stresses which could lead to early particle fracture [22].

2.3. Applications for $AlSiC_p$

2.3.1. Aerospace, Ground Transportation, and Electronics. It has been estimated that the aerospace industry accounted for 5% by mass and 14% by value of the worldwide MMC market in 1999 [1]. One major demand came from the International Space Station which demanded lightweight space structures with high pointing accuracy and dimensional stability [3]. However, interest in MMCs was also in high demand in many of the commercial sectors. Aluminum alloy reinforced with SiC particles became an important material for aerospace applications because of its ability to disperse heat and maintain high dimensional stability. The demand for $AlSiC_p$ can be observed in products such as F-16 ventral fins and fuel access door covers, rotor blade sleeves on the Eurocopter, and fan exit guide vanes. These applications for $AlSiC_p$ was not limited to external features but also to secondary products in the aircraft such as avionic racks, ammunition racks, and hydraulic manifolds [1]. Joints and attached fittings for truss structures were also developed, as shown in Figure 3. Other products that may not be limited to aerospace but was potentially used in aircrafts also included longerons, electronic packages, thermal places, mechanism housings, and bushings [3].
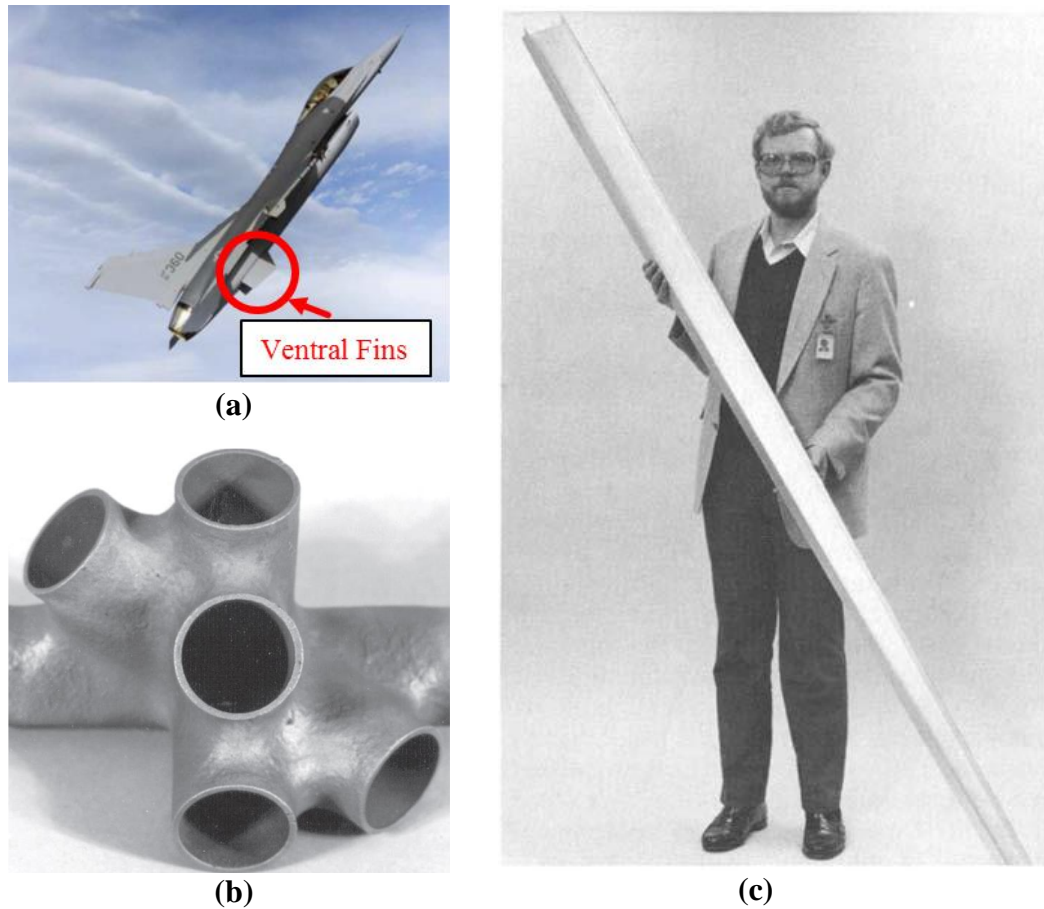
Figure 3. (a) F-16 pMMC Ventral fins (b) Cast AlSiC$_p$ Multi-inlet fitting for a truss node (c) Advanced aircraft stabilator spar [1,3,19].

The high strength-to-weight ratio of AlSiC$_p$ is important for many ground transportation applications as there is a need for a reduction in fuel consumption and an increase in fuel economy [2]. The ground transportation market was estimated to account for 62% by mass and 7% by value of the MMC market in 1999. Although this market sector represented a majority of the MMC market, its value was low because of its concentration on pMMCs which are generally produced through low-cost processing methods [1]. Its applications in the ground transportation industry is expansive and has included intake and exhaust valves, driveshafts and propshafts, connecting rods, brake components, and

selectively reinforced pistons and cylinder bores that can be seen in the Toyota diesel engines, as shown in Figure 4 [1,2,4].
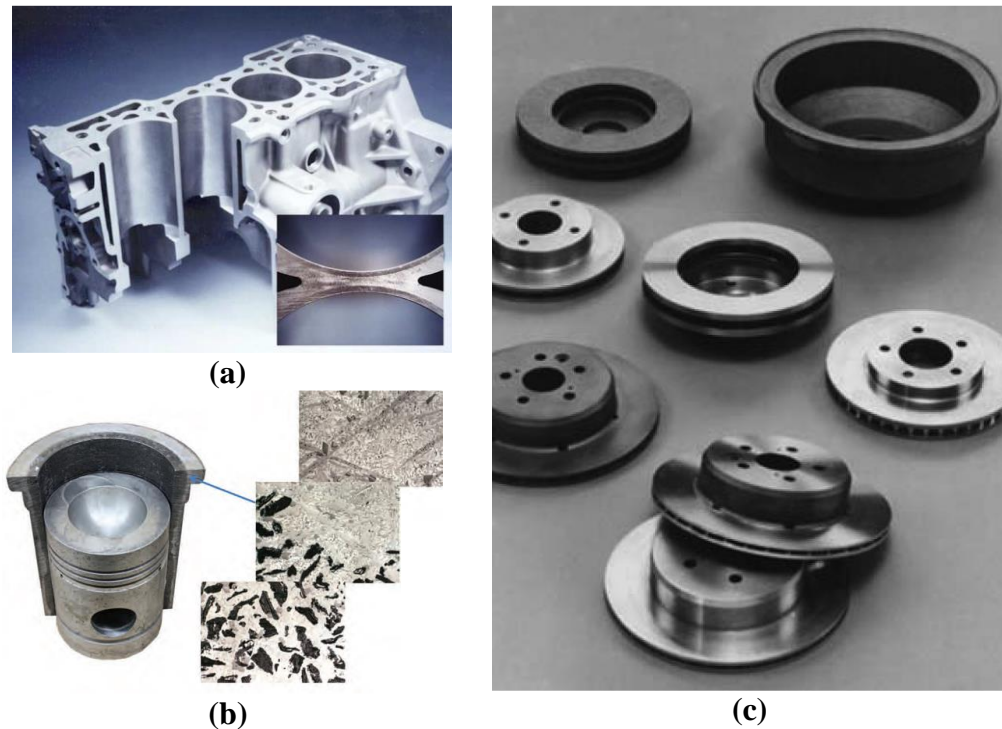
Figure 4. (a) Engline block with MMC cylinder liner (b) Toyota diesel piston with particle reinforcement (c) MMC brake drums and rotors [1,4,20].

The use of $AlSiC_p$ in pistons allowed for reduced clearances between the piston and the cylinder wall due to its low CTE which allowed for high dimensional stability. This lead to improved performances that can be seen in drag race cars. The application of $AlSiC_p$ in driveshafts and propshafts has seen success because of its high specific modulus. The main limitations of driveshafts made with monolithic materials is its dynamic instability at high rpms. However, the critical speed can be increased due to the higher specific modulus of $AlSiC_p$. Aluminum alloy reinforced with SiC particles has also been used in connecting rods because it allows for a 12-20% reduction in secondary shaking forces which improve

fuel economy and increases peak rpm ranges by 15-20%. The durability is also increased and has been proven to have high fatigue resistance as high as 150°C [2]. The ability to handle continuous loads with low wear rates is also appealing in spur gears. The wear rate that spur gears experience can be improved with increasing SiC ceramic content. The stresses that spur gears encounter is especially critical at the gear teeth [5]. Lastly, AlSiCp brakes have been proven to reduce weight while offering high thermal conductivity, good wear resistance and reduced noise. This application is especially important in railroad brakes where the brakes make up 20% of the total weight [2].

The electronics industry is also known as the thermal management industry because of the popularity of MMCs for managing heat. This material property is especially important as electronics become smaller and more compact and will need better thermal management. The thermal management market was estimated to account for 27% by mass and 66% by value of the MMC market [1]. This large value percentage confirms the high demand for thermal management in electronics. Products that need a low CTE and high thermal conductivity include radio frequency (RF) microwave packaging, insulated gate bipolar transistor (IGBT) power modules, and thermal management for high-end microprocessors that include power amplifiers, heat sinks, PCB cores, cold plates, chip carriers, heat spreaders, and rectifier packaging [1,6,7]. Figure 5 illustrates some of the electronic applications of AlSiC$_p$.
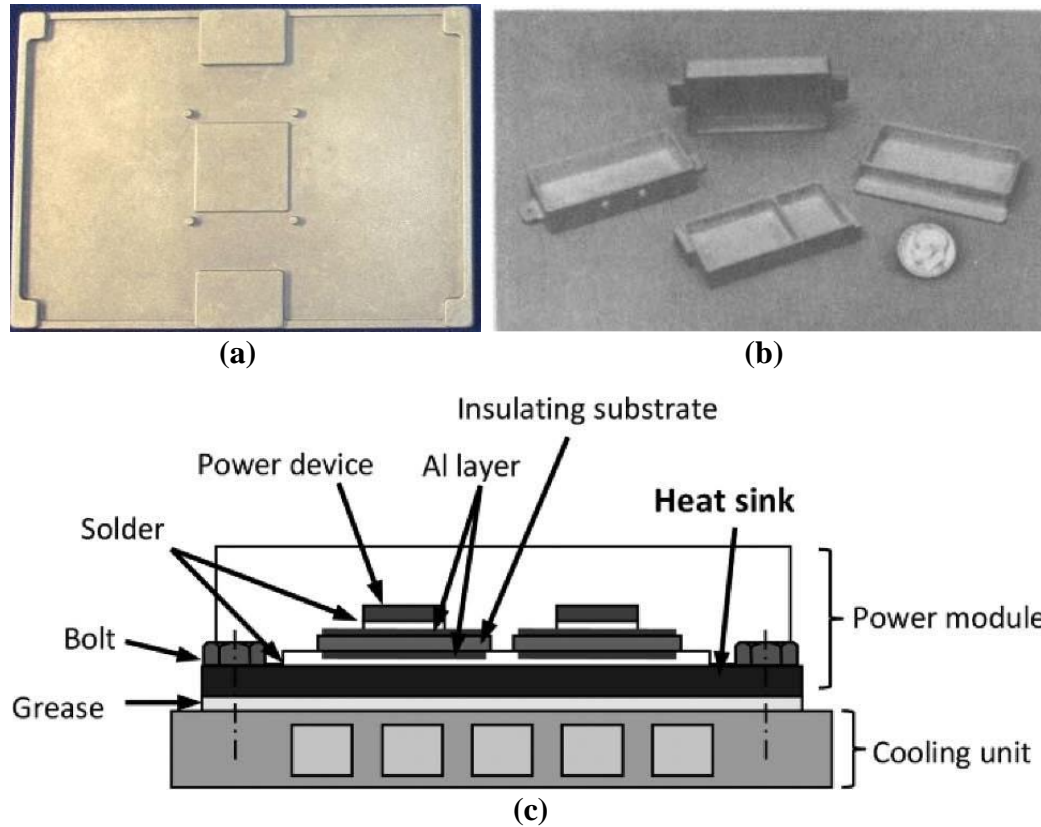
Figure 5. (a) Microprocessor chip lid courtesy of CPS Technologies (b) AlSiC$_p$ electronic packages (c) IGBT power modules with AlSiC$_p$ heat sinks [7,19].

The demand for AlSiC$_p$ in telecommunications and radar systems with RF microwave packaging is ever rising as the need for lightweight materials become more important. Aluminum alloy reinforced with SiC particles is an excellent material that maintains low weight while having high strength. Additionally, most processing methods produce a near net shape that allows for hermetic microwave packaging [1]. Insulated gate bipolar transistor power modules have been found to be used in electric and hybrid vehicles and are in high demand for thermal management [1]. An illustration of IGBT power modules can be seen in Figure 5c. These types of vehicles produce a great amount of heat and require high reliability to function properly. The heat generated by these vehicles cause thermal fatigue in the soft solder due to different the CTEs and lower the reliability of the

IGBT. Thermal fatigue is further worsened by the temperature cycles which cause crack propagation and reduce heat transfer. Metal matrix composites like AlSiC$_p$ provide a controlled linear CTE with high thermal conductivity that allows IGBT power modules to function without high thermal stresses [7,9]. Furthermore, laptops and cellphones have become a huge market for AlSiC$_p$ as manufacturers seek to pack and compact more electronics in their products while reducing the weight and cost. It has been predicted that using pMMCs can have a weight savings up to 80% and a cost reduction as high as 65% [6]. The material used is especially important to maintain peak performance and reliability in electronics. If the electronic device exceeds its maximum temperature the life of the product could be seriously affected [10].

2.4. Casting Processes of AlSiC$_p$

The casting process is important to understand as it determines the material properties of AlSiC$_p$. Figure 6 shows an assortment of SiC particles that are used in the casting processes. The particles have a rectangular and jagged shape and vary with size. This can influence the interaction between the SiC particles and Al matrix during the casting process.
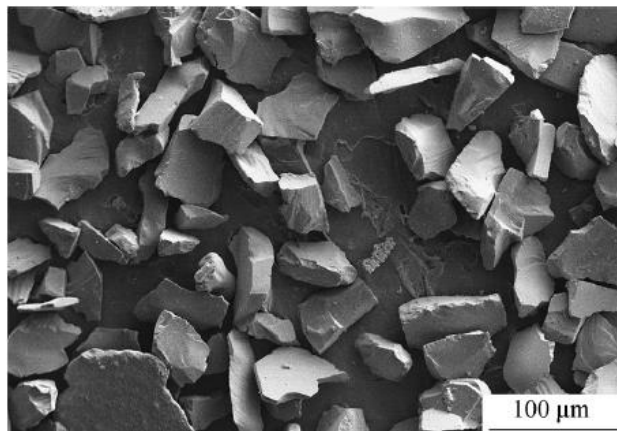
Figure 6. SEM micrograph of SiC reinforcement used in casting processes [23].

2.4.1. Powder Metallurgy. Powder metallurgy techniques have seen wide success in many monolithic and composite applications. This processing method allows fabrication versatility in creating complex geometries with a near net shape and high homogeneity [11]. The implementation of the powder metallurgy process for AlSiC$_p$ can be observed in functionally graded materials (FGM). Functionally graded materials consist of multiple layers that can vary in volume fraction to serve different actions at each layer [24,25]. A study performed by Übeyli et al. discusses the development of FGMs as armor material for defense applications. The goal was to produce an AlSiC$_p$ FGM that would have a hard outer layer that erodes the projectile and a tough inner layer that absorbs the remaining kinetic energy. However, it was shown that the increase in SiC reinforcement produced a more brittle pMMC with a lower fracture toughness [25]. Regardless, powder metallurgy proved to be an effective method to produce multiple layers of varying SiC reinforcement because of its ease in fusing the layers during the sintering process.
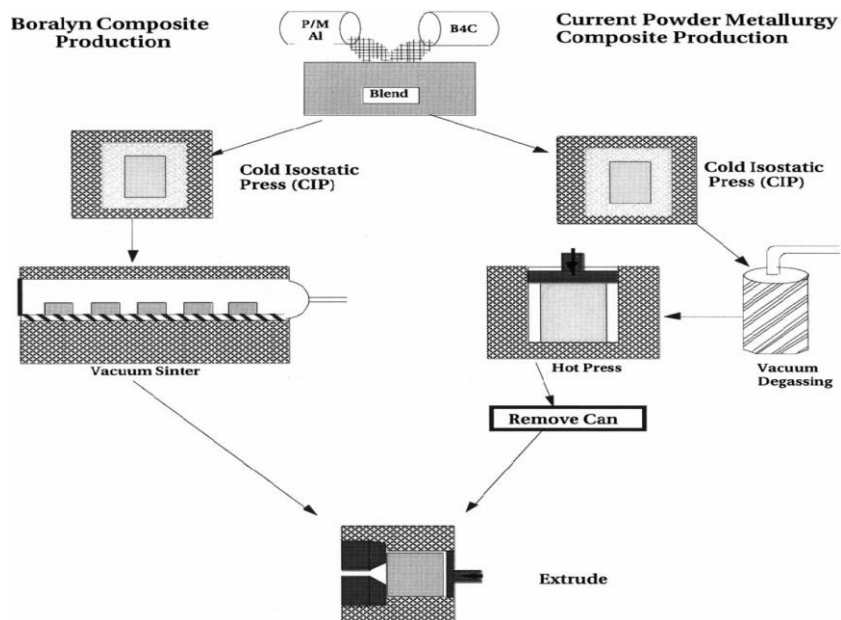
Figure 7. Powder metallurgy process [11].

The powder metallurgy process is a solid-phase process that can be broken down into three steps, as shown in Figure 7. The first step in the powder metallurgy process is to blend the aluminum alloy powder and SiC particles together in a planetary ball mill to obtain a homogenous mixture. The planetary ball mill includes multiple steel balls that is agitated via impellers attached to a shaft. This taps and vibrates the powder placed in the mill which breaks up the hard agglomerates through impact forces and shear forces. This process is carried out for many hours under argon gas until the powder is cold welded and has a uniform distribution. This helps reduce the chances of segregation which can weaken the material's strength [25–27]. The reason this process is done under argon gas is because argon gas is non-reactive and mitigates any excess chemical compounds from forming. It was found in a study by Canakci et al. that increasing the milling time increased the deformation and work hardening of the powders which increases the strength of the $AlSiC_p$. However, the milling process comes at a cost of reinforcement fracture which may not be desired.

The second step in the powder metallurgy process is to form cold pressed samples, otherwise known as green samples. A compacting die is cleaned with acetone so that the powders do not get contaminated and then lubricated with zinc stearate for easy removal. Then the milled powder is placed into the die and cold pressed under low temperature and high pressure. The amount of pressure varies depending on the application but previous studies have it set in the range of 100-250 MPa [25–27]. This step is important to prepare a pre-compressed green sample to allow for better bonding between the Al alloy and SiC particles during the sintering process. Additionally, the tendency to shrink during sintering decreases with an increase in apparent density [26].

The last step in the powder metallurgy process is to form the final product which are hot pressed and sintered. Another compacting die is coated with zinc stearate to help lubricate the die and for easy removal of the samples. The cold pressed samples are placed into the die and compressed at high temperatures and high pressures under argon gas. The studies vary in terms of temperature and pressure but most experiments ran the hot pressing above 500°C and above 300 MPa to allow for better consolidation of the samples and reduce porosity [24,25,27]. The argon gas is non-reactive and prevents any excess chemical compounds from developing that could have developed through the thermodynamic driving force.
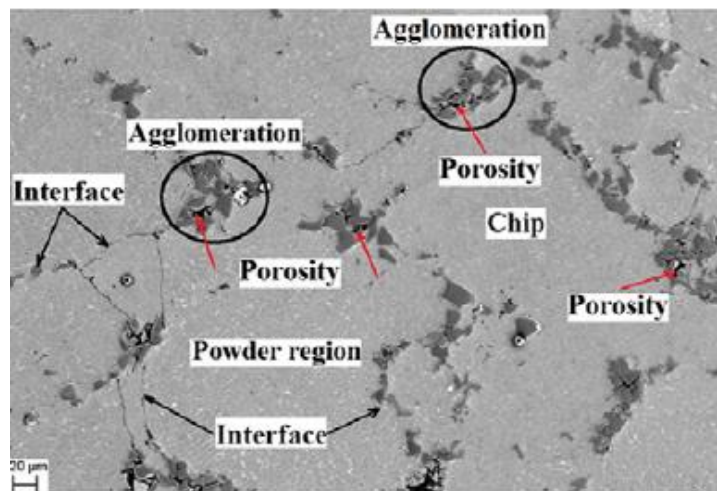
Figure 8. SEM micrograph of hot pressed AlSiC$_p$ 5% vol. showing agglomerations and pores [27].

Although the samples are hot pressed and consolidated, studies have found that agglomerations of SiC particles and pores could not be avoided, as shown in Figure 8. It is well known that pores and agglomerations can cause a significant reduction in strength, load carrying capacity, and hardness of the material. This reduction is due to the ease of crack initiation at the pores [24,27]. One method of counteracting this reduction in strength

is to add more SiC particles which is well known for increasing the hardness of the pMMC [27]. However, the increase in SiC reinforcement has the tendency to create more agglomerations which creates more pores [25]. Erdemir et al. found that increasing the SiC content from 30% to 60% saw an increase in pore content from 0.5674% to 2.0272%. These agglomerations form because of weak compressibility of the hard SiC particles. Cankci et al. discusses the difficulty of the densification of the powders in rigid dies in terms of sliding and rearrangement of the particles. With the addition of more SiC particles, the ability of the powders to slide and rearrange becomes more difficult because the reinforcement does not plastically deform.

Two methods of improving the strength of $AlSiC_p$ that Übeyli et al. and Yao et al. examined were precipitation aging and nanoparticle strengthening, respectively. It was discovered that the hardness can be increased by precipitation aging. However, overaging can still occur which can weaken the pMMC due to the coarsening of the grains. Fortunately, the aging treatment had a positive effect on the bending strength but was irrelevant in terms of SiC content. This means the precipitation strengthening occurred because of the Al alloy and not the SiC particles [24]. However, precipitation aging can also lead to creating excess chemical compounds such as Al_4C_3 which is known to cause an embrittling effect. The next method of improving the strength of $AlSiC_p$ is through SiC nanoparticles. It is well known that refining the grains of pMMCs will increase the strength significantly. The goal Yao et al. had for their study was to restrict the grain growth by the dragging effect of the SiC nanoparticles. This increased the ultimate tensile strength and decreased the elongation to fracture. The reason for these increases can be attributed to grain boundary strengthening and dislocation strengthening due to the pinning of

dislocations by the SiC nanoparticles [28]. However, it is well known that finer particles tend to agglomerate leading to higher porosity and weaken the pMMC [27].

Cankci et al. also examines the possibility of recycling Al alloy chips into the powder metallurgy process. The study was aimed at reducing the fabrication costs while maintaining a structurally sound pMMC. The results were concluded to be acceptable for many applications at varying volume fractions of recycled Al alloy chips and Al alloy powders. These results were an attempt to reduce the cost of fabrication via powder metallurgy and make it a more cost effective operation.

2.4.2. High-Pressure Infiltration.

2.4.2.1. *Conventional Infiltration.* The high-pressure infiltration process is advantageous compared to other processing methods because it allows the infiltration of a metal melt through a preform of fibers, whiskers, or porous bed of loose particles with minimal contact time. The contact time between the Al alloy melt and SiC reinforcement is essential to minimize because it reduces the interfacial reactions that can form Al_4C_3 which is prone to weaken the material's strength through an embrittling effect. This also eliminates the need for coating on the reinforcement and reduces gas porosity. In some cases, the setup for high-pressure infiltration can be considered easier for producing pMMCs because it uses pressurized air to infiltrate the melt into the preform [11,29].
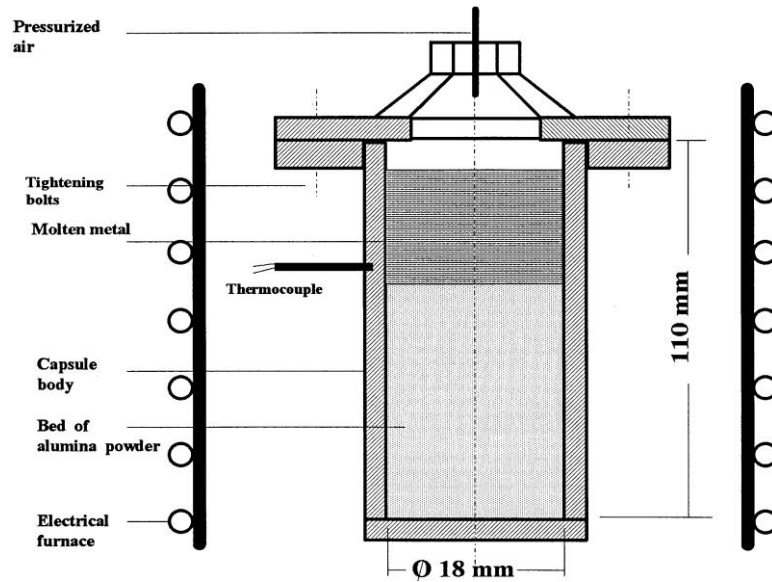
Figure 9. Fabrication schematic of conventional high-pressure infiltration process [29].

A fabrication schematic of the high-pressure infiltration process though conventional methods is shown in Figure 9. Before the process begins, the steel casings are coated with a mixture of graphite, sodium silicate, and water and then dried in a muffle furnace. This preparation is important to ensure the preform and melt do not stick to the casing. Then, the first step is to tap pack the preform of SiC particles into the steel capsule and preheat it under argon gas. The next step is to pour the Al alloy melt on top of the SiC preform. The preheating of the capsule under argon gas ensured the Al alloy melt did not solidify on contact and did not produce excess chemical compounds. The last step is to enclose the capsule and use high-pressurized air to allow the Al alloy melt to infiltrate through the SiC preform. The amount of pressure and time used vary from 1 to 140 MPa and 30 to 60 s, respectively, depending on the size of the steel capsule [29,30]. The infiltration time can be reduced by increasing the pressure and as stated earlier, can be good for minimizing interfacial reactions. However, too much pressure can cause preform deformation and delamination when the pressure exceeds the elastic compression strength

of the SiC preform. Moreover, too little pressure can cause shrinkage voids due to insufficient infiltration of the Al melt through the SiC preform [31].

The samples from Assar et al. show that the distribution of particles were not uniform and in fact created a gradient of SiC particles across the length of the samples. The samples are split into 3 regions, where the first region shows complete infiltration with no pores, the second region showed some pores but with uniform distribution of reinforcement, and the last region had agglomerations with many pores. It could be concluded that the infiltration is easier near the pressurized air but is harder to penetrate the farther it is from the source. Additionally, it was found that a decrease in particle size tended to increase porosity due to the difficulty of the melt infiltrating through the narrower spaces [29]. This result can also be applied to an increase in SiC content as the Al alloy melt will have a harder time infiltrating. Next, Beffort et al. examined the alloying effects from the Al alloy during the infiltration process. It is known that Mg in the Al alloys tends to enhance the wetting behavior of the SiC particles and form $MgAl_2O_4$ or MgO at the interface of oxidized SiC particles which protect it from excess reactions. Additionally, Mg, Zn, and Cu have been proven to provide solid solution strengthening and allow for secondary heat treatment. However, the addition of Mg has also been shown to create excess chemical compounds such as Al_4C_3 and Mg_2Si which weaken the material through the embrittling effect [30].

2.4.2.2. ***Centrifugal Infiltration.*** The centrifugal high-pressure infiltration process is very similar to the conventional method. They both aim to infiltrate the SiC preform with the Al alloy melt through high-pressure. The difference between the two, is that the centrifugal method uses a centrifuge system that creates high-pressure through rotational motion, as shown in Figure 10. This system aims to eliminate porosity that was seen in the conventional process. The first step in this process, is to pack the SiC preform in a steel mold and place it in the runner/mold system. Then, the second step is to preheat the centrifuge system and pour the Al alloy melt into the runner. Similar to the conventional process, the preheating of the system allows the metal to not solidify on contact. Last, the centrifuge system is closed and rotated at 2700 rpm. This creates a centrifugal force that allows the Al alloy melt to infiltrate the SiC preform [32].
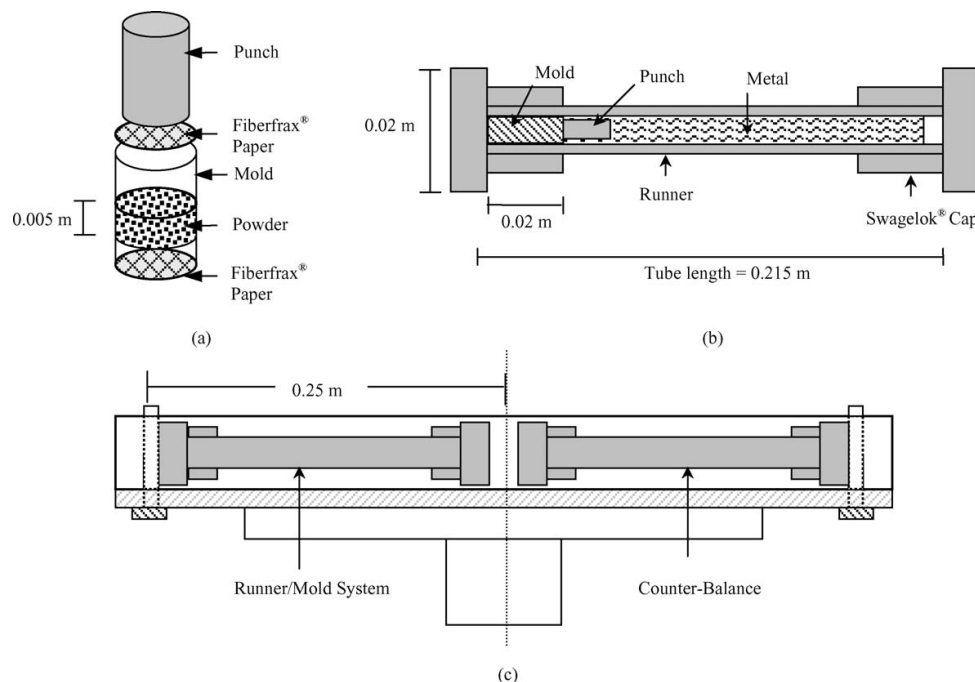
Figure 10. Fabrication schematic of centrifugal high-pressure infiltration process [32].

The samples that were created showed no porosity and showed full infiltration of the melt into the preform. However, it had reinforcement-free channels which formed in some of the samples, as shown in Figure 11. These un-reinforced channels show dendritic structures from the Al alloy which are forming because there are no SiC particles to pin the grain boundaries [32]. The un-reinforced channels can be explained due to the high pressured formed by the centrifuge system and deforming and delaminating the preform [31].
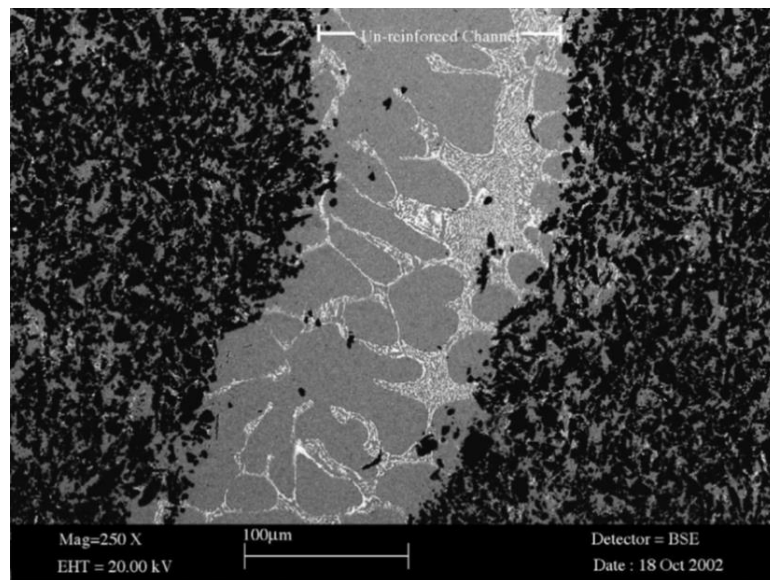
Figure 11. SEM micrograph showing un-reinforced channel with dendritic structure [32].

2.4.3. Stir Casting. Based off a study done in 1999, the cost of stir casting was one-third to half of all competing processing methods and was expected to fall to one-tenth. This processing method is promising for pMMCs because of its simplicity, flexibility, and potential to produce in large quantities [33]. The processing parameters that are considered in this processing method is the viscosity of the liquid metal, heat transfer rate, wettability, stirring method, agglomeration of the reinforcement before and after mixing, and mold shape and temperature [34].
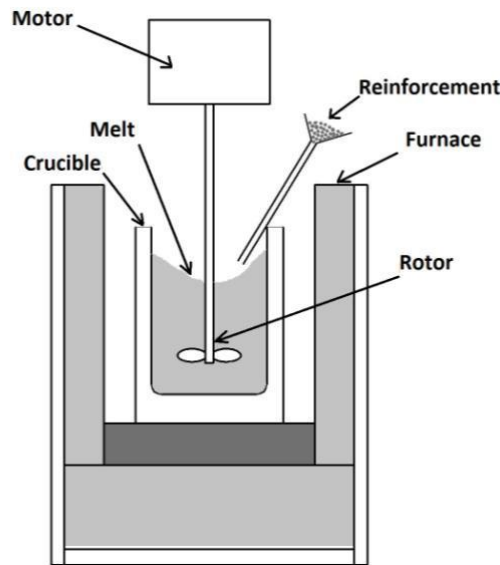
Figure 12. Fabrication schematic of stir casting process [35].

The fabrication schematic of the stir casting process is shown in Figure 12, and can be broken up into three steps. Before processing the $AlSiC_p$, a coating is applied in the crucible to avoid contamination. First, the Al alloy melt is added to the heated crucible and stirred by a mechanical stirrer to form a vortex under argon gas. The addition of argon gas prevents the formation of oxides that can react with the SiC particles or Al alloy matrix which can

weaken the pMMC. Next, the SiC particles are added in at a fixed rate on the outside of the vortex. If the SiC particles are fed in too quickly, they can clump up and create agglomerations and pores. As a result, it is essential to maintain a constant rate of SiC particle addition. Moreover, the vortex formed from the constant stirring is important to maintain to transfer the particles into the liquid metal and maintain a state of suspension of the SiC particles. A minimum stirring time is also needed allow ceramic particles to incorporate into the aluminum melt. Higher stirring temperatures can also be used to increase the incorporation rate but leads to higher risk of shrinkage porosity and Al_4C_3 formation. Once all of the SiC particles are fed into the crucible, the stirring is stopped and poured into a pre-heated mold [23,33,35,36]. There are also cases in which the mold was hydraulically pressed to minimize porosity [1].

2.4.4. Casting Processes Comparison.

Table 2. Comparative analysis of different processing methods [33].

Method	Range of Shape and Size	Metal Yield	Range of Volume Fraction	Damage to Reinforcement	Cost
Powder Metallurgy	Wide range, restricted by size	High	-	Reinforcement fracture	Expensive
High-Pressure Infiltration	Limited by preform shape, tends to be small	Low	Up to 0.45	Severe damage	Moderately expensive
Stir Casting	Not limited by size	Medium	0.4 to 0.7	Little damage	Moderate

The discussion of the processing methods is necessary to understand the advantages and disadvantages of each method. This comparative analysis can be seen in Table 2. For Powder metallurgy, complex geometries can be created but with limited size. Powder metallurgy also has a tendency to fracture the reinforcement which may be undesired and can lead to agglomerations. The cost for producing products is also very high. High-

pressure infiltration has potential to create large sizes with complex geometries but is limited by the preform shape and has severe damage to the reinforcement. The cost of high-pressure infiltration is moderately expensive, but has potential to grow. Stir casting is the most cost effective of all the three processing methods, as it is the most simple and flexible method that can create the largest casting sizes. Additionally, it has little damage to the reinforcement which can lead to repeatable results.

By taking the comparisons of each casting process, it can be concluded that stir casting is the most promising casting method. It is the most cost effective process that is able to produce large batches with high consistency. Therefore, the workpiece samples that will be used in this research will be from stir casted $AlSiC_p$.

2.5. Machining Processes of $AlSiC_p$

Casting processes do not provide the necessary geometrical precision and surface integrity that a product requires. Machining has the ability to create complex geometries with high precision and accuracy with a good surface finish that casting processes cannot produce with near net shape forming or modified casting methods [12,13,15,16]. In order to evaluate the machining process, the cutting parameters such as feed rate, width of cut (WOC), depth of cut (DOC), or cutting speed can be varied and compared to cutting forces, tool wear, power consumption, or surface finish [37].

However, $AlSiC_p$ has been known to be a difficult material to machine because of its hard ceramic reinforcement. These particles can form alien distribution of dislocations that pile up near the machined surface and cause work hardening. This creates high cutting forces and extreme tool wear. Paired with the sliding of the abrasive particles along the

face of the cutting tool, rapid tool wear can occur and raise the cost of machining [14,15,38,39]. Excessive tool wear is a challenge for machining processes because it can cause excessive heat which worsens the tool life and compromises surface integrity via burr formation [40]. Additionally, higher volume fractions of reinforcement is known to cause a significant rise in temperature and consequently, increase tool wear rate and burr formation. Thus, there is a need to examine current machinability studies on AlSiC$_p$ and create a more efficient and economical machining method to offset the machining costs [39,41].

2.5.1. Turning of AlSiC$_p$. Turning operations, also known as orthogonal cutting, is a common machining process that only uses a single point of contact to remove material. Orthogonal cutting incorporates a fixed cutting tool with a rotating workpiece, as shown in Figure 13. The cutting tool is fed into the workpiece perpendicular to the cutting direction, which causes plastic deformation and chip formation. A majority of research related to the machinability of AlSiC$_p$ is performed via orthogonal cutting on CNC lathe machines. These studies can be found in [11,12,14,15,38,40,42].
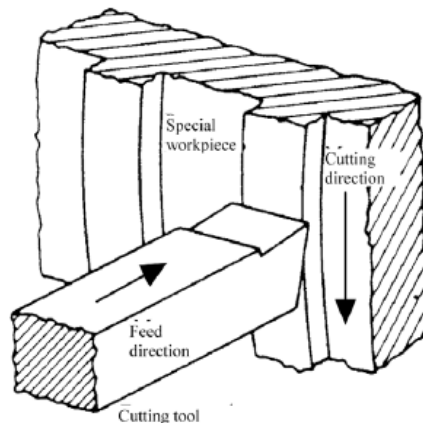
Figure 13. Orthogonal cutting diagram with cutting tool being fed perpendicular to the cutting direction [43].

The study of orthogonal cutting of AlSiC$_p$ is imperative to understand the cutting interactions that could occur for milling operations. Most researchers have agreed that the dominant wear mechanisms when machining AlSiC$_p$ is from abrasion and adhesion. Abrasive wear can be categorized as two-body abrasion and three-body abrasion. Two-body abrasion is described as a softer surface rubbing on a harder rough surface while three-body abrasion is caused by the sliding of a hard particle in between two surfaces [12,39]. Figure 14 shows both of these abrasive wear mechanisms.
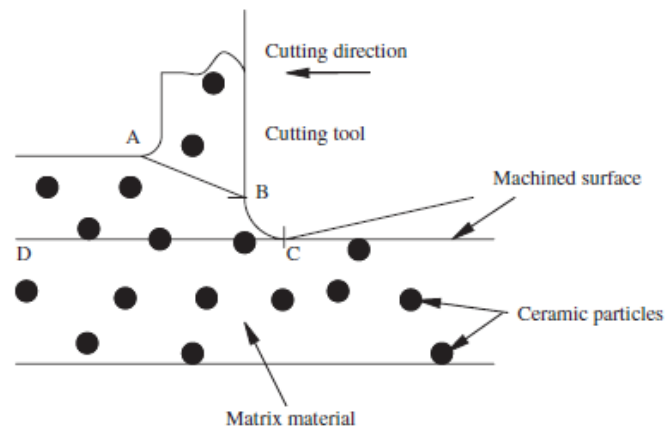
Figure 14. Cutting edge sliding across pMMC surface and interacting with metal matrix and reinforcement [44].

El-Gallab et al. found that the SiC particles tended to abrade the rake face of the cutting tools and cause grooves. Li et al. explains that this grinding effect is from the cutting tool moving the hard reinforcement rather than cutting or breaking them. This would lead to flank wear and eventual tool failure. Adherence occurs when there is a build-up of material on the cutting tool at high temperatures and pressures. However, adhesion is not

as dominant of a wear mechanism as abrasive wear [39]. Both of these wear mechanisms can be seen in Figure 15.
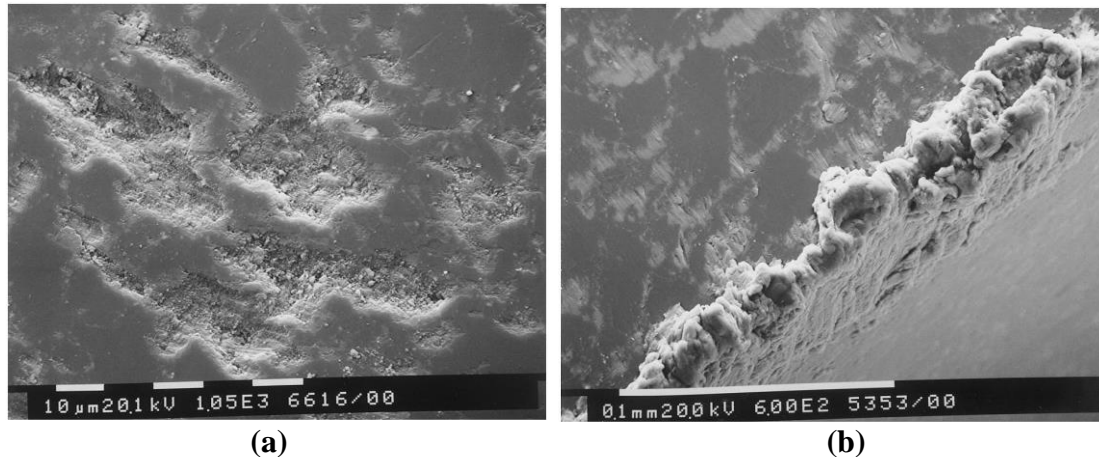
Figure 15. Tool wear mechanisms (a) abrasive wear forming grooves (b) adhesive wear forming BUE [14].

A main concern when machining AlSiC$_p$ is the effects of different cutting parameters on machining productivity. The general consensus among researchers is that an increase in cutting speed, feed rate, and depth of cut (DOC) increases flank wear and adversely affect machining productivity. This is due to the increase in contact area and increase in grinding rate from the abrasive particles [14,40,42]. Manna et al. describes doubling the cutting speed and DOC to have also doubled the rate of tool wear, respectively. Moreover, increasing DOC was proven to increase cutting forces and surface roughness values. Additionally, at large depth of cuts, there were higher chances of adhesion wear from BUE. This wear mechanism is exacerbated at low cutting speeds and feed rates. However, increasing cutting speed was shown to have the opposite effect on cutting forces and surface roughness values. Kannan et al. describes this phenomenon as

thermal softening which causes a reduction in average dislocation density. The heat generated from the high cutting speeds allows for the relaxation of the work hardening.

The findings presented in previous works can be used to investigate the machinability of $AlSiC_p$ through the milling process. With an increase in applications of pMMCs, the variety of $AlSiC_p$ that will be available will be a major challenge to explore. The current work presented via orthogonal cutting mainly consists of low volumes of ceramic reinforcement. It is well known that an increase in reinforcement content or size will increase tool wear. This is due to the abrasive nature of the hard SiC particles [38,42]. Thus, there is a need to examine higher volume fractions of reinforcement by end milling to expand the potential applications.

2.5.2. Non-Conventional Machining of $AlSiC_p$. The difficulty of machining pMMCs has been a major concern that has hindered the expansion of applications for $AlSiC_p$. One method that researchers have examined to circumvent the abrasive and adhesive wear mechanisms is through non-conventional machining processes. These processes include abrasive water jet machining, electro discharge machining, and laser cutting. These types of machining processes are promising because they achieve material removal rate through indirect contact.

Abrasive water jet machining uses high-pressurized water mixed with varying sizes of abrasive particles to abrade away the workpiece material and create the desired shape. The main mechanism for MRR is a combination of scooping induced ductile shear and plowing action of abrasive particles [45]. The performance of AWJ depends on the water supply pressure, nozzle diameter, nozzle stand-off distance, abrasive type, abrasive flow

rate, and abrasive particle size. The main benefit of AWJ over conventional machining methods is being able to maintain low temperatures with no thermally affected zones at high feed rates. This is especially promising for creating intricate shapes in brittle and hard materials where fracture occurs more easily than ductile materials [45–47]. However, previous studies from Müller et al. have shown rough surfaces when cutting $AlSiC_p$ at high feed rates. This was confirmed at University of the Pacific by Vargas et al., where AWJ machining produced striations with a arithmetic surface roughness value (R_a) of 12.75 μm, as shown in Figure 16a. These striations could be explained due to the cutting lag and step removal which is most common in thick materials being cut at high feed rates. There is also a loss of energy by the water jet in thick materials because of particles deflecting off the workpiece [45,46]. Still, even when lowering the feed rate to allow for more penetration, AWJ machining tended to produce a taper due to the long exposure of the water jet and slow feed rate [47]. Hamatani et al. observed that for thicker materials, the top surface tended to be rounded or damaged while the bottom surface had burr formation. They also noticed a temperature increase of the ceramic during machining. AWJ machining is also limited in the shapes it can create.
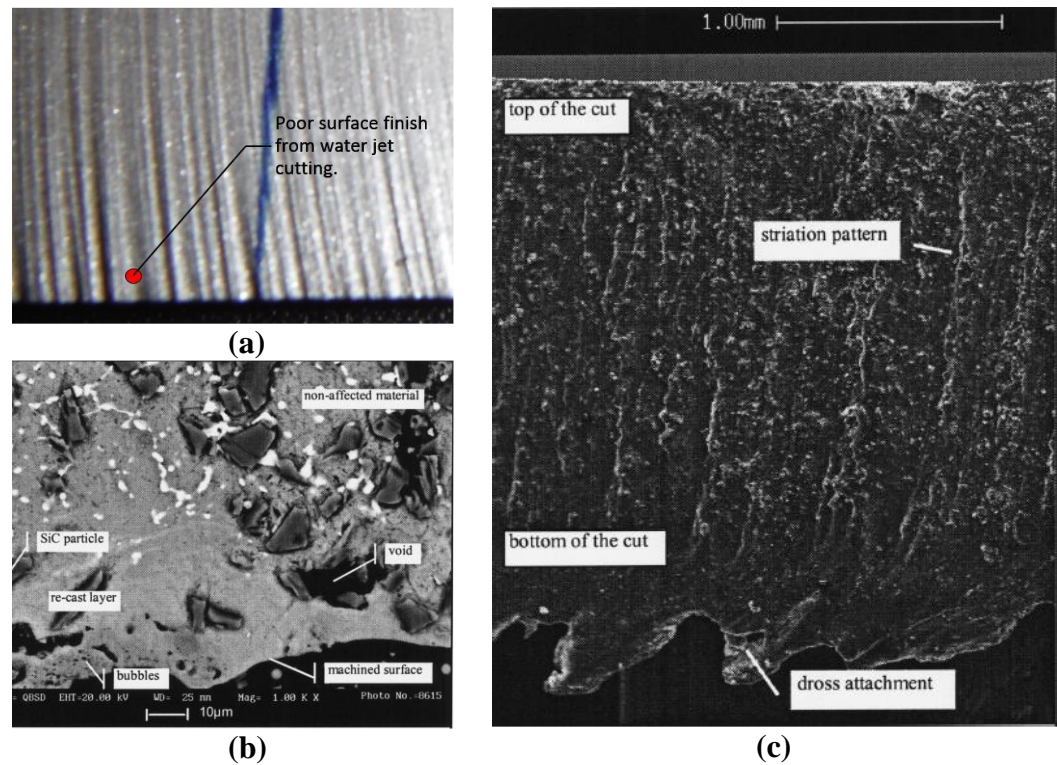
Figure 16. (a) AWJ machining of AlSiC$_p$ with R$_a$ = 12.75 μm (b) EDM of AlSiC$_p$ with surface damage (c) Laser cutting with striations and burr formation [17,46].

Electro discharge machining has been popularized in the automotive, aerospace, biomedical, mold, and tool and die industries. It has undergone many variations like ultrasonic vibration, dry, powder mixed, water, and micro-EDM [11]. The EDM process is advantageous because the electrode does not make direct contact with the workpiece [48]. In fact, Singh et al. has shown that AlSiC$_p$ at a 10% volume fraction of reinforcement can be machined by EDM. However, the EDM process is slow due to the low electrical conductivity, low thermal conductivity, and high thermal resistance of the SiC particles. An increase in SiC content has shown to decrease the feed rate because of the higher resistance in the workpiece [46]. In order to increase the MRR, a higher discharge current and pulse duration can be applied, but this can increase thermal loads which create molten

material that re-solidify and re-cast. This re-casted layer changes the microstructure and produces cracks and surface damage, as shown in Figure 16b [46,49]. Electro discharge machining has also been known to remove material quickly in the beginning but slow down at the later stages due to entrapment of SiC particles in the spark gap. This also compromises the dimensional stability of the product [49].

Laser cutting is known to have a high degree of accuracy by producing a narrow width of cut. A majority of laser cutting uses CO_2 lasers with a wavelength of 10.6 μm. However, laser cutting tends to produce striations from interment flow of the molten material. Laser cutting has also had difficulty machining thicker materials as the lower portion is melted and swept downwards due to the vaporization of the molten matrix. This excessive heating also changes the microstructure of the $AlSiC_p$ [46]. Figure 16c shows the surface damages done by laser cutting. In most cases, secondary machining will be needed to improve the surface integrity. Consequently, Przestacki et al. recognized this problem and experimented with a combination of orthogonal cutting with laser assisted machining (LAM). They concluded that an increase in the pMMCs temperature had a tendency to decrease the yield strength below the fracture strength which allowed for easier material removal by plastic deformation. The cutting tools still experienced flank wear by abrasion and adhesion, but was higher without LAM [50].

Non-conventional machining methods have seen success in many industries but is limited when machining $AlSiC_p$. The surface quality is generally poor with surface damages across the workpiece. The types of geometries that can be created from these machining processes are also limited when in comparison to end milling.

2.5.3. End Milling of AlSiC$_p$. The end milling process is a versatile machining operation that is widely used in the automotive, aerospace, and die and mold industries because it can create simple flat surfaces or complex geometries [51]. The end milling process differs from orthogonal cutting because it is a material removal process that uses multi-tooth cutting tools. These cutting tools create an interrupted cut with non-uniform chip loading and cutting force variations, which make it a complex process to analyze [37,52–54]. This research aims to concentrate on the end milling process because it can expand the applications of AlSiC$_p$ across all the different industrial sectors by creating a variety of complex geometries with high dimensional stability.

Even though end milling is an important machining process, little research has been performed on AlSiC$_p$ with high volume fractions. Most researchers have focused on ceramic reinforcement with less than 30% volume fraction and with small SiC particle sizes. It is unclear what effects high percentage of ceramic reinforcement will have on wear mechanics [16,55]. Vargas et al. had performed slot milling experiments on AlSiC$_p$ with 30% volume fraction and found that machinability at high volume fractions was viable but was met with extreme tool wear. However, their experiments had focused on conventional methods of end milling. Today, most industries focus on Computer Integrated Manufacturing (CIM) utilizing Computer Aided Manufacturing (CAM) software that is able to produce complex geometries with high machining efficiency. These programs could increase machining productivity by reducing manual input and increasing material removal rate [56]. More recently, CAM softwares have included HSM strategies that increase MRR and extend tool life. These strategies can be applied to AlSiC$_p$ to improve the machining efficiency.

2.5.3.1. ***Conventional Milling.*** The end milling process evolved from orthogonal cutting, where there was a need to machine parts with a rotating cutting tool rather than a rotating workpiece. Conventional end milling operations include a rotating cutting tool being fed into the workpiece with linear tool paths to create the desired geometry. The amount of material removed depends on WOC and DOC which forms the contact area. Figure 17 provides a simplified illustration of this milling process.
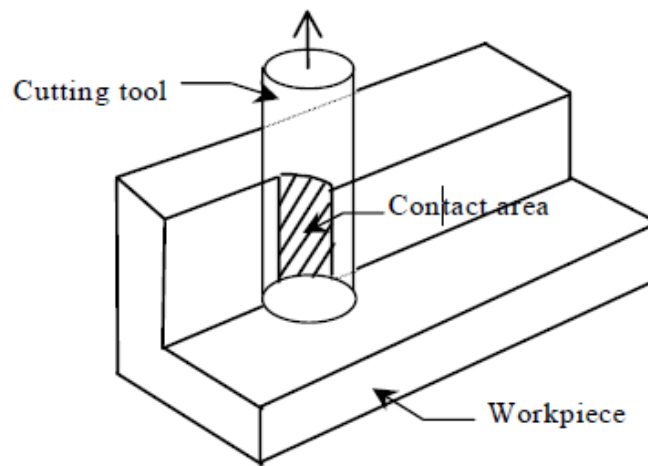
Figure 17. End milling diagram with DOC and WOC forming the contact area [57].

Research on the end milling process of AlSiC$_p$ is limited. However, studies have produced similar results to orthogonal cutting. Similar to orthogonal cutting, abrasive and adhesive wear are the dominant wear mechanisms. Based off previous studies, the main parameters that affect the wear mechanisms are cutting speed, feed rate, depth of cut, and SiC content. Increasing the SiC content, feed rate, and DOC had increased the tool wear [37]. Arokiadass et al. had found that SiC content had the greatest effect on flank wear followed by feed rate and DOC. Additionally, an increase in cutting speed produced higher tool wear due to the cutting edge being thermally softened from heat generation. However,

lower cutting speeds tended to form larger and unstable BUE due to the higher pressure and friction from higher chiploads [37]. This BUE could be detrimental to machining because it produces grooves which creates more adhesion and abrasion.
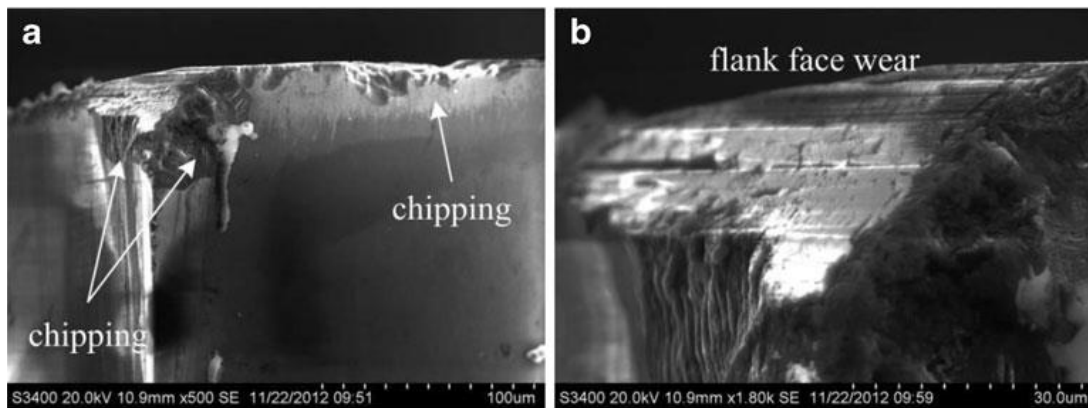
Figure 18. PCD cutting tools (a) tool chipping (b) flank wear on rake face [55].

In some cases, edge and corner breakage can occur in brittle tool materials like PCD tools [16]. Bian et al. had observed microdefects, microcracks, and pits after machining due to microfractures. They also observed large defects due to SiC particles being cut or pulled out. The alternating stress from the end milling process was concluded to induce tool and workpiece vibrations which caused chipping and cleavage on the tool tip. This was especially prominent in diamond cutting tools because of their low impact toughness, as shown in Figure 18 [55].

In order to reduce the temperature and pressure from milling $AlSiC_p$, Huang et al. experimented with wet machining. Coolant has the benefit of reducing the temperature and pressure on a cutting tool, which is a major challenge because of the heat generated from the particles rubbing. Moreover, coolant helps flush away chips and abrasive powder which

prevents re-cutting and help minimize abrasive wear. They concluded that the flank wear on the wet cutting experiments were slightly larger than the dry cutting experiments. This led to a faster rate of increase in cutting forces when using coolant [16].

(a) Tool Wear: 98.85 mm²   **(b) Tool Wear: 151.16 mm²**
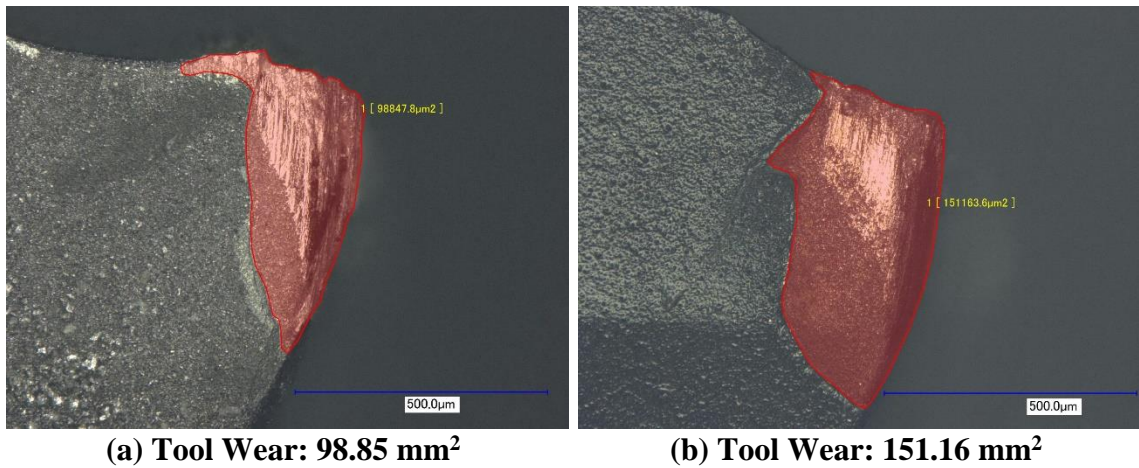
Figure 19. CVD diamond coated end mills (a) Tool wear from dry cutting experiments (b) Tool wear from wet cutting experiments [17].

Similar cutting experiments were performed at University of the Pacific by Vargas et al. with CVD diamond coated cutting tools. They had varied cutting speed, feed rate, and depth of cut while performing dry and wet cutting tests. It was concluded that decreasing DOC would lead to lower cutting forces. However, flank wear was observed for all of their experiments. When running the endurance cutting tests under dry and wet cutting conditions, it was found that similar to Huang et al., the wet cutting conditions had a higher tool wear, as shown in Figure 19. The flank wear for wet machining was nearly double the tool wear of dry machining. Moreover, coating delamination was observed, which led to early tool failure.

2.5.3.2. ***Trochoidal Milling***. Trochoidal milling was originally made for producing slots using uniform circular movements with simultaneous forward movements to keep force constant and to reduce vibrations [18,53,58]. Figure 20a illustrates the cutting motion of trochoidal milling. The cutting engagement angle, which is shown in Figure 20b, is kept constant during the machining operation. The engagement angle is defined as the contact area that is engaged in the workpiece during the cutting process. Sharp corners and slots can increase the engagement angle which will increase cutter load and cause tool fatigue and damage. This is a serious problem in hard materials like AlSiC$_p$ [59,60].

(a)   **(b)**
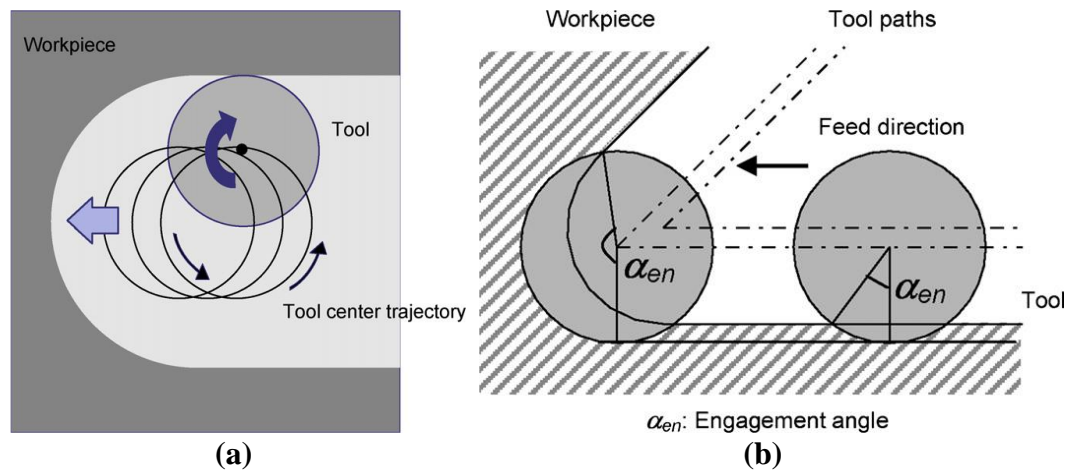
Figure 20. (a) Trochoidal tool path with linear movement combined with circular motion (b) Effects of engagement angle at different locations [59].

A majority of CAM softwares adopt conventional tool paths like zigzag and peripheral, which are generated by offsets of the input boundary to be machined. This is an issue because this tool path has no concern for the machining process and can create cutting problems associated with varying cutting engagement angles. This varies the cutter load and damages the tools. Figure 21 shows the difference between a conventional tool path compared to a trochoidal tool path. Conventional milling will have moments where the tool

is fully engaged and be more prone to risk of failure while trochoidal milling maintains constant low engagement. Trochoidal milling is a safer and faster alternative to conventional machining methods as it restricts cutting forces and allows for higher feed rates. Current CAM softwares like MasterCAM and CATIA have recognized the benefits of trochoidal milling [51,59,60].
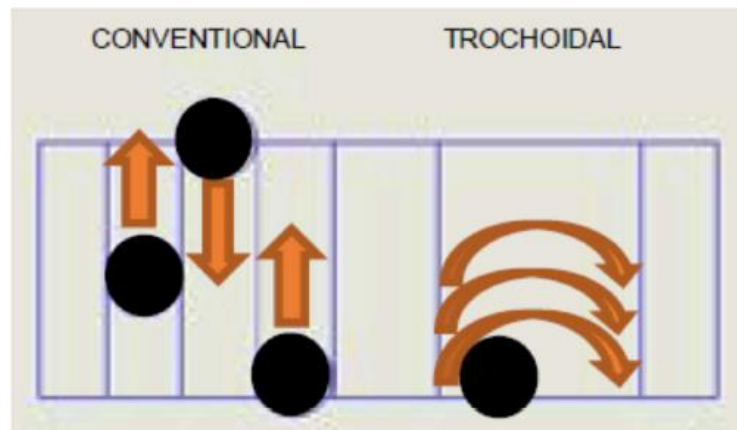
Figure 21. Tool path comparison between conventional and trochoidal machining [18].

Conventional strategies at critical regions tend to require an experienced operator to carefully design the machining conditions [59]. This is problematic in the aerospace industry where many components have pockets and ribs with thin walls, sharp corners, free-form surfaces, small holes, and narrow or deep groves [61]. Trochoidal milling eliminates the need for careful planning of machining conditions by maintaining constant chipload through consistent slicing of material [59].

Trochoidal milling has been applied to hard materials like titanium and Inconel 718 but has not been explored on $AlSiC_p$. When machining titanium and Inconel 718, it was discovered that the machining cycle times had increased but the tool wear decreased. This

meant that the overall productivity increased because cutting tools could last longer, which reduced the downtime for replacing cutting tools [18,53,58]. In fact, trochoidal milling has shown 3.5 to 4 times lower cutting forces than slot milling operations [62]. The chip evacuation was also improved, which increased surface integrity and lowered cutting temperatures [18]. This research will apply the trochoidal milling operation to $AlSiC_p$ to extend tool life and make end milling a more viable machining option.

2.6. Cutting Force Models and Simulations

Cutting force models and finite element analysis (FEA) simulations have been a valuable part of research and industry practice. The capabilities to predict cutting forces in milling is essential to predict power and torque requirements, vibrations, workpiece surface quality, geometrical accuracy, and develop ideal cutting parameters. In industry, these models and simulations help reduce the manufacturing costs by improving machining efficiency without consuming cutting tools or stock material [57,63]. These attempts were made on $AlSiC_p$ to better understand the cutting interaction between the cutting edge and abrasive particle.

A common cutting force model used to simulate chip formation in MMCs is the Merchant Model, as shown in Figure 22. This model was developed by Ernst and Merchant and allows for prediction of cutting forces during orthogonal cutting. The Merchant's diagram separates the forces into cutting force (F_c) and thrust force (F_t) which can be translated into a shear-stress diagram. The chip is considered as a separate body in equilibrium with two equal and opposite forces from the tool and the workpiece [44]. An assumption is made that the feed is relatively smaller than the depth of cut. This model has been used as the foundation for many cutting force models but does not factor in free

surface geometry or imperfect surfaces like the hard abrasive particles, which can cause variation in the results [64]. As a result, the Merchant model tended to overestimate their results when cutting aluminum metal matrix composites [43,65]. Pramanik et al. proposed using Griffith's theory to estimate the energy for particle fracture by the tool's cutting edge. However, workpiece material properties are needed to accurately model the cutting of pMMCs [63]. Cutting force models are especially limited when modeling the end milling process due to multi-tooth interrupted chipping, non-uniform chiploads, and cutting force variations [54].
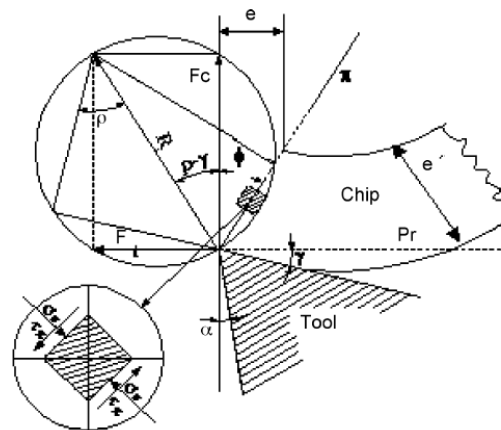
Figure 22. Merchant model schematic showing F_c, F_t, and shear-stress diagram [65].

Finite element analysis simulations offers a viable solution to the complex computations required for end milling pMMCs. The main challenge of modeling pMMCs versus traditional monolithic materials is the particle size, shape, and arrangement [64,66]. The effects of the reinforcement is necessary to understand tool wear development and surface quality. During machining, the tool will interact with the particle and de-bond it from the metal matrix [64]. Figure 23 illustrates the possible tool-particle scenarios that

may occur during machining. The particle may either be along the cutting edge, above the cutting edge, or below the cutting edge. Along the cutting edge, fracture may initiate de-bonding at the interface. The particles will move up with the chip and cause tool wear, and compressive loads in the reinforcement and the cutting tool. Above the cutting edge, particles interact with the tool and cause high compression loads which may initiate particle fracture. Then the particle moves up along the tool while interacting with its surrounding particles. Below the cutting edge, the tool passes over the particle, causing residual compressive stresses and indentations in the workpiece.
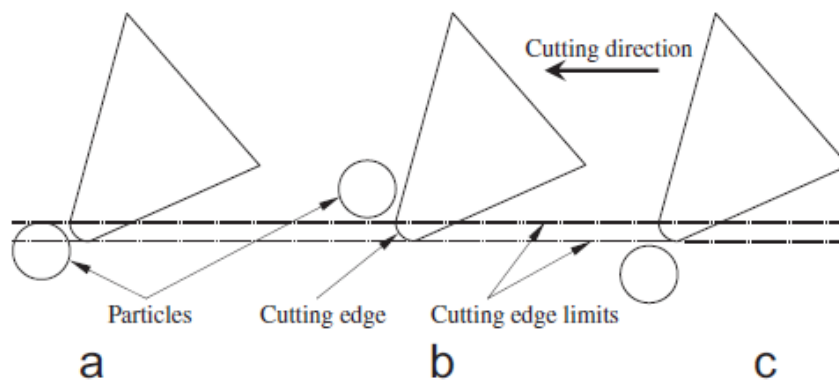
Figure 23. Tool-particle interaction (a) along the cutting edge (b) above the cutting edge (c) below the cutting edge [64].

With the tool-particle interactions defined, FEA simulations could be created to simulate cutting into pMMCs. Umer et al. attempted to simulate the tool-particle interaction in pMMCs using ABAQUS, as shown in Figure 24. They concluded that the tool-particle interaction varied depending on the inputs to the finite element models. They had also assumed the particles were round, isotropic, and perfectly elastic material. This is not the case for real SiC particles which are rectangular in shape and vary in size.
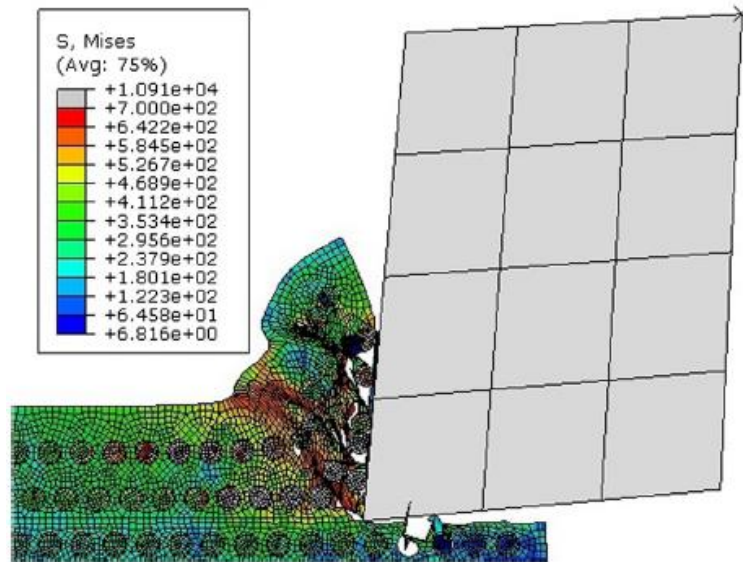
Figure 24. FEA simulation of tool-particle interaction in pMMCs [66].

Cutting force models and FEA simulations can offer an insight to a general trend in tool-particle interactions but is limited on the inputs of the user. This research chooses not to concentrate on cutting force models or simulations but to experimentally study the machinability effects of $AlSiC_p$.

2.7. Cutting Tools

Cutting tools are an essential component to a machining process. For cutting tools, the tool material is the most important parameter when machining $AlSiC_p$. High speed steel and carbide tools have seen great success and wide use in the automotive and aerospace industries. Carbide end mills have even machined difficult to cut materials like hardened steel and titanium. Carbide cutting tools are especially popular in the aerospace industry for creating complex pockets and ribs [61,67]. Huang et al. describes carbide cutting tools to show promise for being less expensive and ideal for roughing $AlSiC_p$ at low volume fractions of reinforcement. However, when HSS or carbide is used to machine $AlSiC_p$ at

high volume fractions of reinforcement, rapid tool wear is met because the SiC reinforcement is significantly harder than the tool material [37,68]. These tools experience rapid tool wear in a short time span. Durante et al. found that when machining AlSiC$_p$ with 20% SiC content, coated carbide tools became dull in seconds [69]. Vargas et al. concluded that carbide produced a better surface finish but created burrs which is known to have a large economic impact in industry.

Tool wear is a serious concern when machining aluminum alloy reinforced with SiC particles, as wear can be up to 7 times more severe than cutting conventional aluminum-silicon alloys [41]. Thus, diamond cutting tools are a must for machining this type of material. Diamond is the hardest and most abrasion-resistant substance that is chemically inert with most materials. Diamond cutting tools are also considered the most cost-effective choice for machining pMMCs [70–72].

2.7.1. Polycrystalline Diamond Cutting Tools. Polycrystalline diamond (PCD) cutting tools are known to be harder than coated and uncoated carbide tools [11]. The higher hardness and lower chemical affinity to pMMCs have given a clear advantage to PCD cuttings tools [13]. Coelho et al. describes PCD cutting tools to last nearly 6 times longer than HSS and carbide tools. Moreover, even though monocrystalline diamond cutting tools have a higher hardness, PCD tools are more easily fabricated making them a more viable cutting tool selection. In order to create PCD tools, PCD blanks with a carbide and cobalt substrate is coated with synthetic diamond grits and allowed to grow in a high temperature and high pressure environment. Once the diamond-to-diamond bonding is finished, the blanks are sliced via EDM and brazed together to form the desired tool geometry [41,73].

Although PCD cutting tools have been recommended to machine $AlSiC_p$, the high cost of these tools have made them a challenge in reducing machining costs. In some cases, experimental tests could not be continually repeated due to the high capital costs of the tools [41]. The cost of PCD cutting tools tended to cost 5-10 times more than contemporary carbide tools with TiN or TiC coating [69]. Thus, there is a need to examine other diamond cutting tools that can be more cost effective, like CVD diamond coated cutting tools.

2.7.2. CVD Diamond Coated Cutting Tools. Chemical vapor deposition technology has developed dramatically within the last 30 years. The CVD process has become more prominent in industry where longer tool life is desired. The tool coating has been proven to influence cutting performance durability, where TiAlN had increased tool life by 1.35 times. Additionally, CVD has been successful because of its ability to coat any tool geometry with ease [67,74,75]. The CVD process can also be tailored for different applications by varying substrate material, coating material and morphology, film thickness, and uniformity. This makes the CVD process ideal for end mills where the cutting geometry can be complex.

The CVD process can be performed via the microwave plasma, hot filament, or plasma torch process. However, this research will focus on the hot filament process as it is the method used to create the CVD diamond coated end mills that will be used for the cutting experiments. First, a carbide end mill is used as a substrate for diamond growth. This is to ensure extra toughness and durability of the cutting tool. Next, the batch of carbide cutting tools are inserted a vacuum chamber, as shown in Figure 25a. Once in the vacuum chamber, the refractory metal wires are heated up to temperatures above 2000 °C and pressurized, as shown in Figure 25b. Methane gas is then fed into the chamber to allow for diamond-to-diamond bonding on the carbide cutting tools. Figure 25c shows the diamond film that was produced on the carbide cutting tools. This coating can be adjust to be thicker or thinner depending on the application [17,70,74]. Increasing the diamond coating was found to reduce coating cracking and improve abrasion resistance and extend tool life [75].
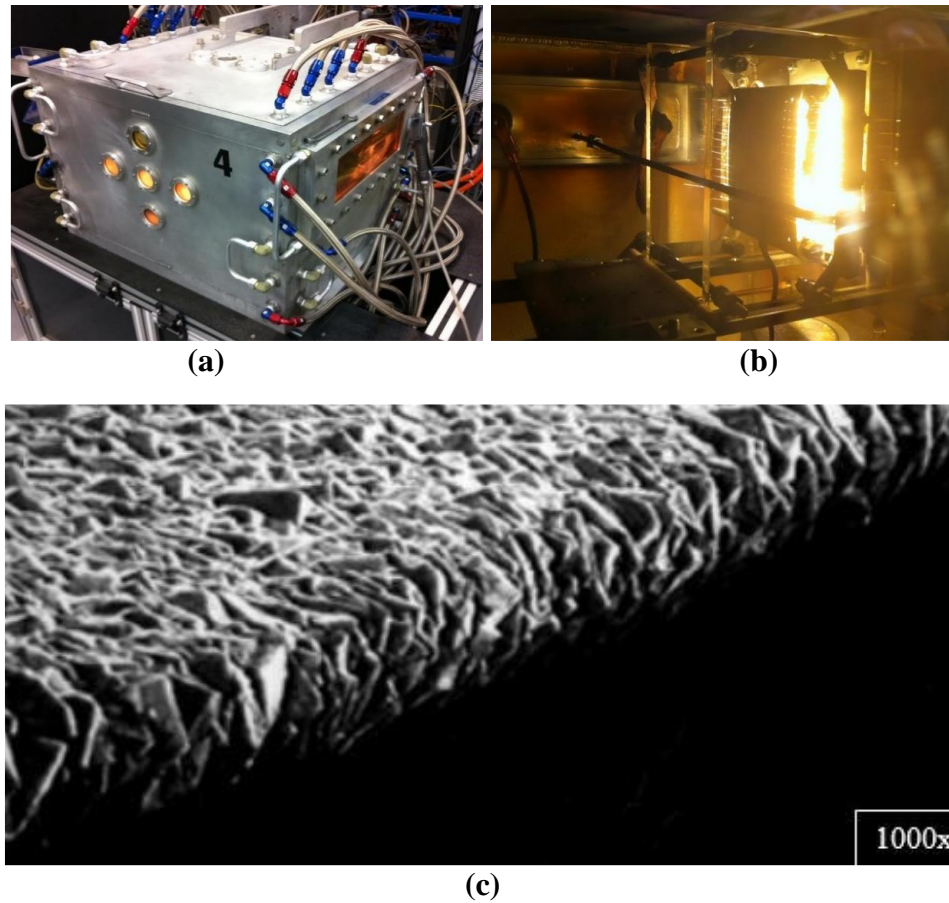
Figure 25. (a) Vacuum chamber used for the CVD process (b) Hot filaments in vacuum chamber (c) Close-up view of a Crystallume CVD diamond coated end mill with uniform coating [17].

CVD diamond coated cutting tools are ideal for machining $AlSiC_p$ because of their high hardness, high thermal conductivity, and chemical inertness. The increase in demand for more cost effective cutting tools and processing methods has driven CVD diamond coated tools to replace many PCD tools. However, CVD diamond coated cutting tools still cost more than HSS and carbide tools. Moreover, the adhesion of the coating becomes a major challenge to overcome. Delamination can lead to early tool failure. Other research related to CVD diamond coated end mills have been performed at University of the Pacific by Vargas et al. and Liu et al.. Both of their research have shown CVD diamond coated

end mills are a viable option for machining $AlSiC_p$. Thus, there is a need to provide an adequate machining strategy and set of cutting parameters to machine $AlSiC_p$ optimally.

Chapter 3: Experimental Methods

3.1. Determining Machining Conditions

A major component to machining $AlSiC_p$ is determining an appropriate set of machining conditions. High volume fractions of reinforcement are known to cause significant rise in temperature and increase tool wear. Without an appropriate set of machining conditions, burr formation and extreme tool wear will be met. Thus, it is important to understand the workpiece material, cutting tool, coolant, and cutting parameters to reduce the number of unnecessary experiments and produce optimal results.

3.1.1. Material Selection.
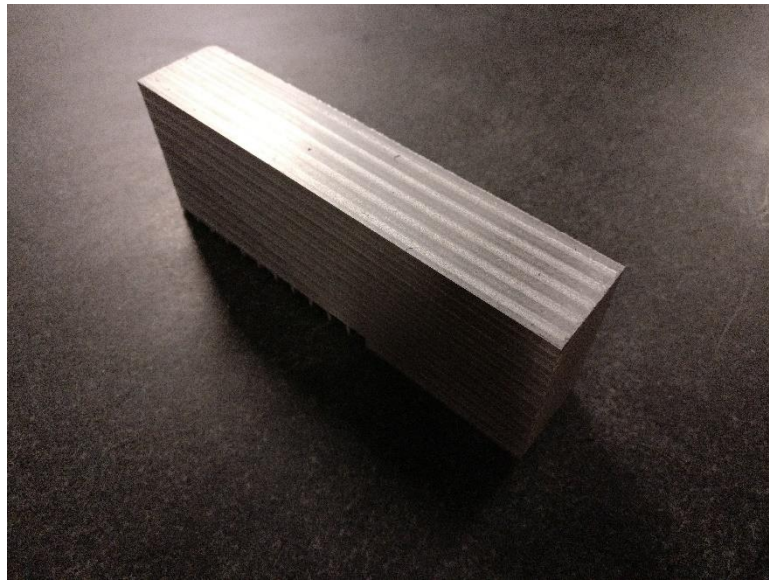
Figure 26. $AlSiC_p$ with 30% volume fraction provided courtesy of Ferrotec Corporation.

The material that will be used for this research will be provided by Ferrotec Corporation. The $AlSiC_p$ workpiece, shown in Figure 26, has a 30% volume fraction of

SiC reinforcement. This type of material has been stir casted and has a uniform distribution of particles, shown in Figure 27. The average particle size is 49.41 μm with a standard deviation of 17.51 μm, as shown in Figure 28. As mentioned previously, the sizes, shapes, and distribution of SiC particles is an important factor for ensuring a structurally sound product. Stir casted $AlSiC_p$ was chosen because it was deemed the most economical and ubiquitous type available in the market. The material properties via stir casting can be found in Table 1 of **Section 2.2**.
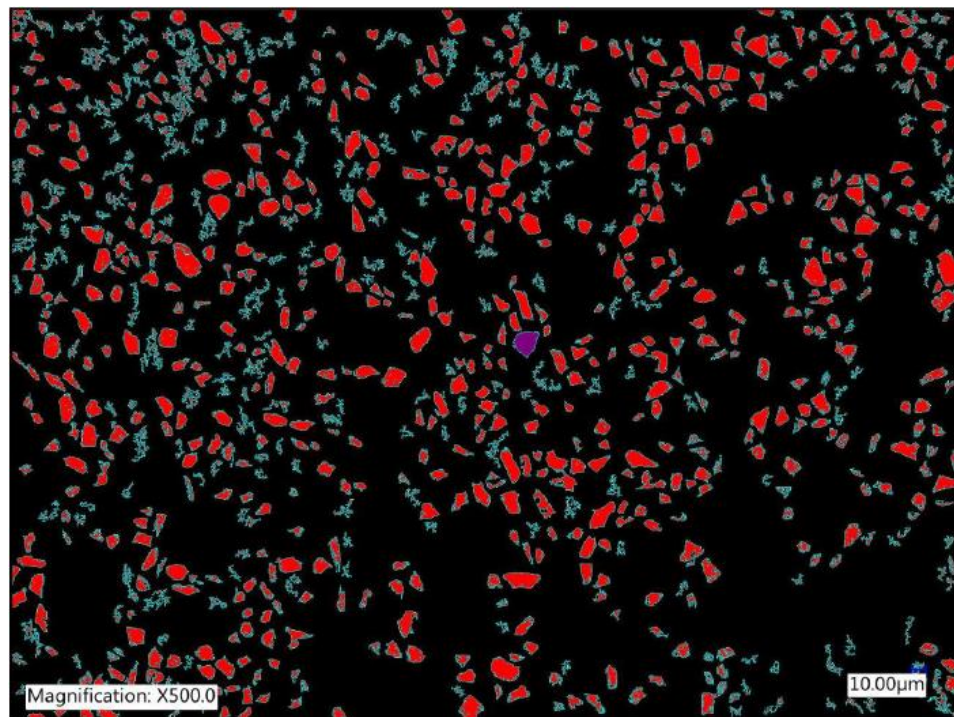
Figure 27. $AlSiC_p$ 30% with uniform particle distribution taken by Keyence VHX-6000 Digital Microscope.
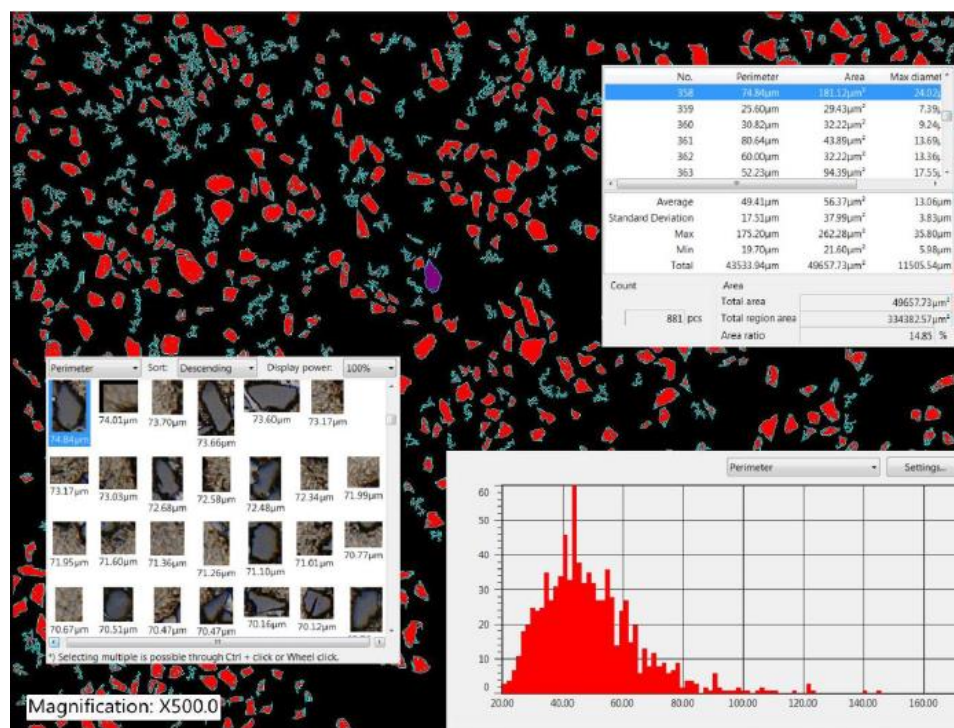
Figure 28. AlSiC$_p$ 30% with an avg. particle size of 49.41 μm and standard deviation of 17.51 μm.

3.1.2. Cutting Tool Selection.

Table 3. Crystallume CVD diamond end mill tool geometry data measured via micrometer and Keyence VHX-2000 Digital Microscope.

Crystallume CVD Diamond End Mill							
Tool No.	*Diameter (mm)*	*Corner Radius (μm)*	*Edge Radius (μm)*	*Radial Rake Angle (°)*	*Helix Angle (°)*	*Flutes*	*Coating Thickness (microns)*
Avg.	6.33	32	35	2	35	4	40

The cutting tool selection is an important factor to consider when machining AlSiC$_p$. Rapid tool wear will occur if tool material and tool geometry is not properly selected. When considering the cutting tool selection, it is important to consider the issues highlighted by Vargas et al. First, the end mills they had used had the following characteristics: 6.35 mm cutting diameter, 50 μm corner radius, 7° radial rake angle, 30° helix angle, and diamond coating thickness of 20 microns. Second during their cutting

experiments, flank wear was dominant from abrasive wear mechanisms. Last, delamination of tool coating was observed during wet cutting conditions. Thus, it can be concluded that the following changes must be made: decrease the radial rake angle and increase the diamond coating thickness. By decreasing the radial rake angle, the cutting edge stability can be increased [76]. As stated previously, a thicker diamond coating is known to increase tool life and have better adhesion to the cutting tool. Moreover, diamond cutting tools are the most effective tool material to use against AlSiC$_p$.
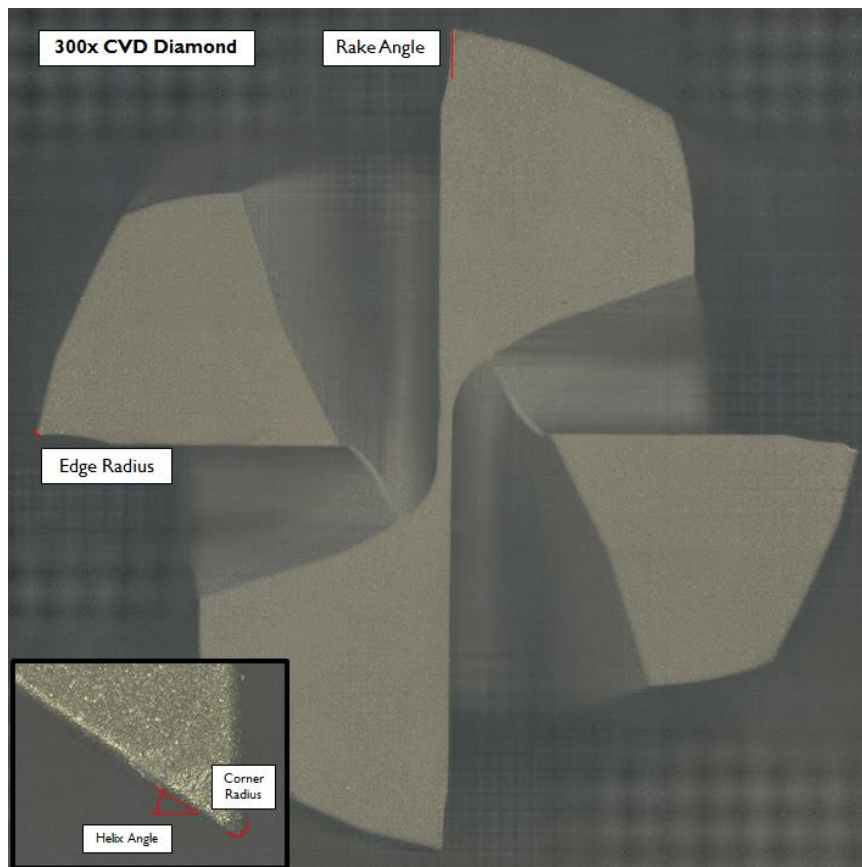
Figure 29. Crystallume CVD diamond coated end mill tool geometry schematic.

This research will be using CVD diamond coated end mills with a 40 micron diamond coating, provided by Crystallume. After receiving the cutting tools, the tool

geometry was measured for quality assurance. Figure 29 shows the areas on the cutting tool that represents the edge radius, corner radius, helix angle, and rake angle. Figure 30 shows the use of a micrometer and Keyence VHX-200 Digital Microscope to measure the cutting tool geometry. Table 3 shows the average end mill characteristics: 6.33 mm cutting diameter, 32 μm corner radius, 35 μm edge radius, 2° radial rake angle, 35° helix angle, and 4 flutes.

(a)

(b)   **(c)**
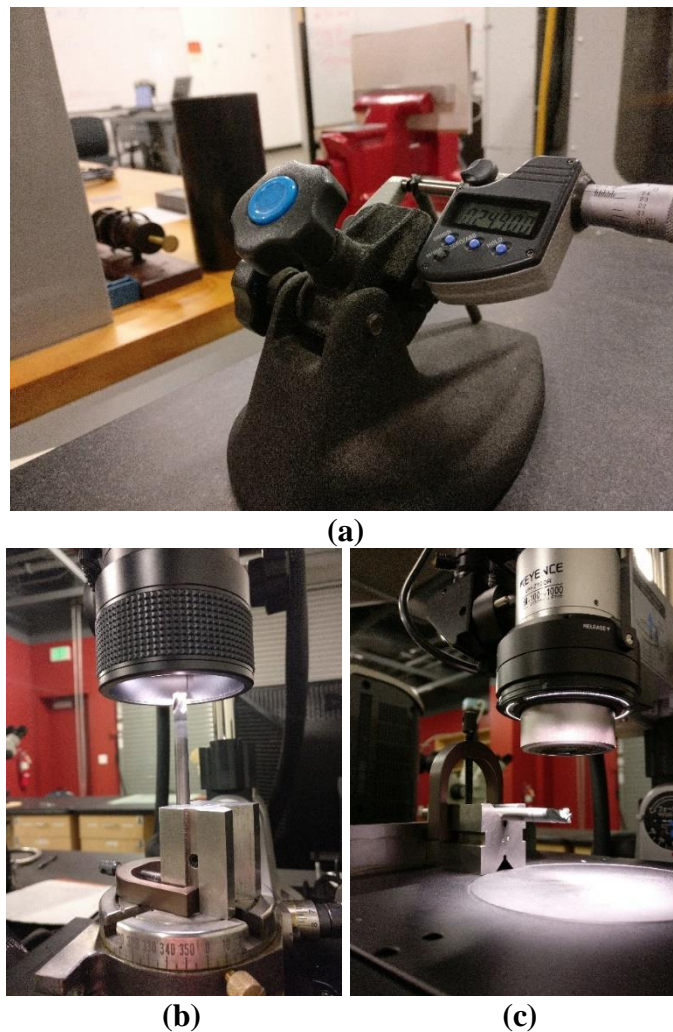
Figure 30. Various orientations to measure cutting tool geometry (a) micrometer measuring cutting tool diameter (b) top view measuring rake angle and edge radius (c) side view measuring corner radius and helix angle.

3.1.3. Coolant Selection. The coolant selection is a major factor in preventing built up edge and improving tool life. During, Vargas et al.'s experiment, an aggressive machining strategy produced severe BUE, as shown in Figure 31. Coolant has been recommended by El-Gallab et al. and Bains et al. when machining at high cutting speeds or feed rates. Cutting fluid has been shown to be effective on hard to cut materials like titanium. During long cutting operations, coolant helps flush away chips and abrasive powders and prevents re-cutting [16].

Figure 31. Severe BUE on CVD diamond end mills [17].

An external spray mist coolant system by Kool Mist will be used during cutting operations. HSM requires high pressure coolant to effectively clear chips off the workpiece. A spray mister is used instead of flood coolant because flood coolant is known to create an abrasive slurry and increase tool wear [17]. The Kool Mist spray mist allows for a concentrated flow of coolant onto the cutting edge without creating a pool of coolant. The Kool Mist external coolant system can be seen in Figure 32a. The coolant that will be used is a water-based coolant known as Formula "78", as shown in Figure 32b. This coolant has been known to be effective on hard to cut materials like Inconel and titanium.

(a)   **(b)**
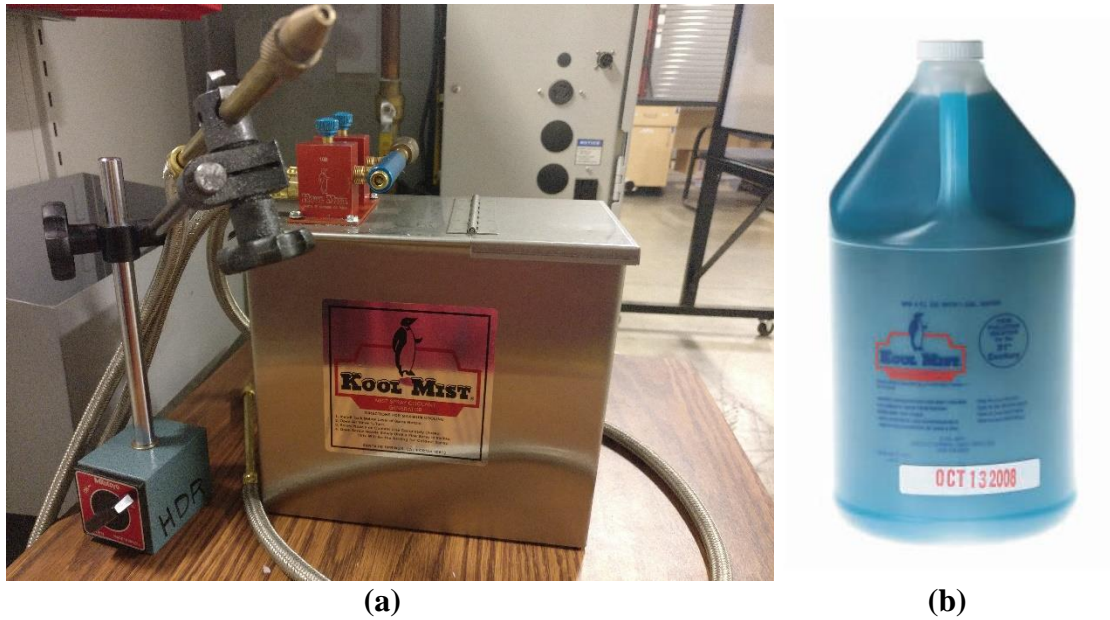
Figure 32. (a) Kool Mist external coolant system (b) Formula "78" water-based coolant.

3.1.4. Cutting Parameters. The cutting parameters that will be considered will play a direct role in optimizing tool life. Based off previous research at University of the Pacific by Vargas et al., the feed rate, cutting speed, depth of cut, and width of cut are major factors to consider for cutting parameters. It was determined that a large DOC is detrimental to tool life. Thus, the DOC will be kept constant for all experiments. An illustration of these parameters can be seen in Figure 33. For this research, the WOC will be labeled as engagement angle (α_e) to better illustrate the different trochoidal tool paths. The cutting parameters that will be used for this research is feed rate, engagement angle, and cutting speed.
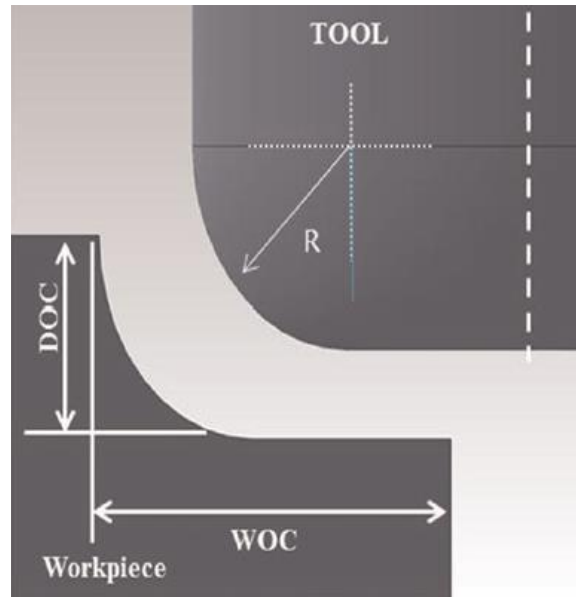
Figure 33. Illustration of depth of cut and width of cut for cutting experiments [70].

3.1.5. CNC Machine Setup. For this research, a Haas VF-1 Computer Numerical Control (CNC) vertical milling machine will be used for all cutting experiments, as shown in Figure 34. The Haas VF-1 specifications include a 20 HP Vector Dual Drive which can operate up to 10,000 r/min and 25.4 m/min. A CNC vertical milling machine will be critical for these cutting experiments as the trochoidal tool path will be created via CAM software. This complex tool path requires a CNC machine that can interpret the Numerical Control (NC) codes generated by the CAM software.

The Cat 40 Taper Tool Holder will be used in conjunction with the VF-1 milling machine. Figure 35 shows the tapered tool holder with a 6.35 mm diameter hole. This tool holder has a set screw on the side that can be screwed down to secure the cutting tool inside the tool holder. The tool holder is then secured into the Haas VF-1 milling machine via vacuum suction.

Figure 34. Haas VF-1 CNC vertical milling machine used for all cutting experiments.

Figure 35. Cat 40 Taper Tool Holder with 6.35 mm diameter hole.

3.2. Creating Design of Experiment

      3.2.1.　Taguchi Method. Taguchi Method will be applied to this research to study the effects of each cutting parameter in relation to the cutting forces, surface roughness, and material removal rate. The Taguchi method was developed by Genichi Taguchi to improve manufactured goods and other engineering applications. It was developed after World War II, when the Japanese manufacturers were struggling to survive with limited resources. It was due to the Taguchi Method that the Japanese manufacturing processes were able to vastly improve through cost savings [77].

      The Taguchi Method is split into three categories: system design, parameter design, and tolerance design. System design is where the cutting parameters are defined to achieve a goal. Parameter design is where the cutting parameters are given preferred values to create robustification. This is the stage where an orthogonal array is used to create a design of experiment. An orthogonal array allows for an optimization of parameters with the minimum amount of combinations possible. This allows performing experiments to be more practical and cost effective. Tolerance design is where the process is optimized through S/N ratio and ANOVA. This stage reduces the variations found in the experiment. There are three equations used to find the S/N ratio, but first, the mean and standard deviation has to be found:

$$\bar{y} = \frac{1}{n}\sum_{i=1}^{n} y_i \qquad\qquad \textbf{Eq. 1}$$

$$S = \sqrt{\sum_{i=1}^{n} \frac{(y_i - \bar{y})^2}{n-1}} \qquad\qquad \textbf{Eq. 2}$$

Thus, the following functions can be used to optimize specific S/N ratios:

Smaller the better (for making the system response as small as possible):

$$SN_S = -10\log\left(\frac{1}{n}\sum_{i=1}^{n}y_i^2\right)$$ **Eq. 3**

Nominal the best (for reducing variability around a target):

$$SN_T = 10\log\left(\frac{\bar{y}^2}{s^2}\right)$$ **Eq. 4**

Larger the better (for making system response as large as possible):

$$SN_L = -10\log\left(\frac{1}{n}\sum_{i=1}^{n}\frac{1}{y_i^2}\right)$$ **Eq. 5**

3.2.2. Analyzing Vargas's Data.

Table 4. Relationship between MRR, Tool Wear, Ra, and Cutting Conditions by Vargas et al.

Test No.	Rank	MRR, cm^3/min	MRR / Tool Wear Ratio	Tool Wear mm^2	R_a, μm	Speed, r/min	Fr, mm/min	DOC mm
1	9	1.61	0.27	5.87	0.82	3500	254	1
2	3	3.23	0.97	3.32	0.73	6500	254	2
3	6	4.84	0.66	7.23	1.14	9500	254	3
4	5	9.68	0.86	11.27	1.77	3500	508	3
5	8	3.23	0.62	5.24	1.01	6500	508	1
6	2	6.45	0.98	6.56	0.79	9500	508	2
7	7	9.68	0.65	14.90	2.93	3500	762	2
8	1	14.52	1.82	7.96	1.28	6500	762	3
9	4	4.84	0.93	5.18	0.89	9500	762	1

The premise of this research was based off another study performed at University of the Pacific by Vargas et al.. In order to set up a design of experiment, it is necessary to understand the data found by Vargas et al.., as shown in Table 4. Their cutting tests focused on maximizing machining productivity by varying cutting speed, feed rate, and depth of cut and measuring the material removal rate per tool wear (MRR/Tw). They concluded that test number 8 had the best MRR/Tw. However, their data did not show the significance of each cutting parameter in relation to MRR/Tw.

Taguchi Method can be applied to this data and analyze the significance of the feed rate, cutting speed, and DOC on MRR/Tw. Equation 5 will be used to maximize the largest response possible, as shown in Table 5. The S/N ratio will then be averaged based off their respective factors and factor levels. The data is shown in Table 6 and plotted in Figure 36.

Table 5. Signal-to-Noise ratio of MRR/Tw for Vargas et al.'s cutting experiments.

Test No.	$(S/N)_L$ (dB)
1	-11.373
2	-0.265
3	-3.609
4	-1.320
5	-4.208
6	-0.149
7	-3.755
8	5.201
9	-0.593

Table 6. Average Signal-to-Noise ratio for each factor: Feed Rate, Cutting Speed, and DOC.

Fr		Speed		DOC	
Sum	*Avg. S/N*	*Sum*	*Avg. S/N*	*Sum*	*Avg. S/N*
-15.246	-5.082	-16.448	-5.483	-16.174	-5.391
-5.677	-1.892	0.728	0.243	-4.169	-1.390
0.853	0.284	-4.351	-1.450	0.272	0.091
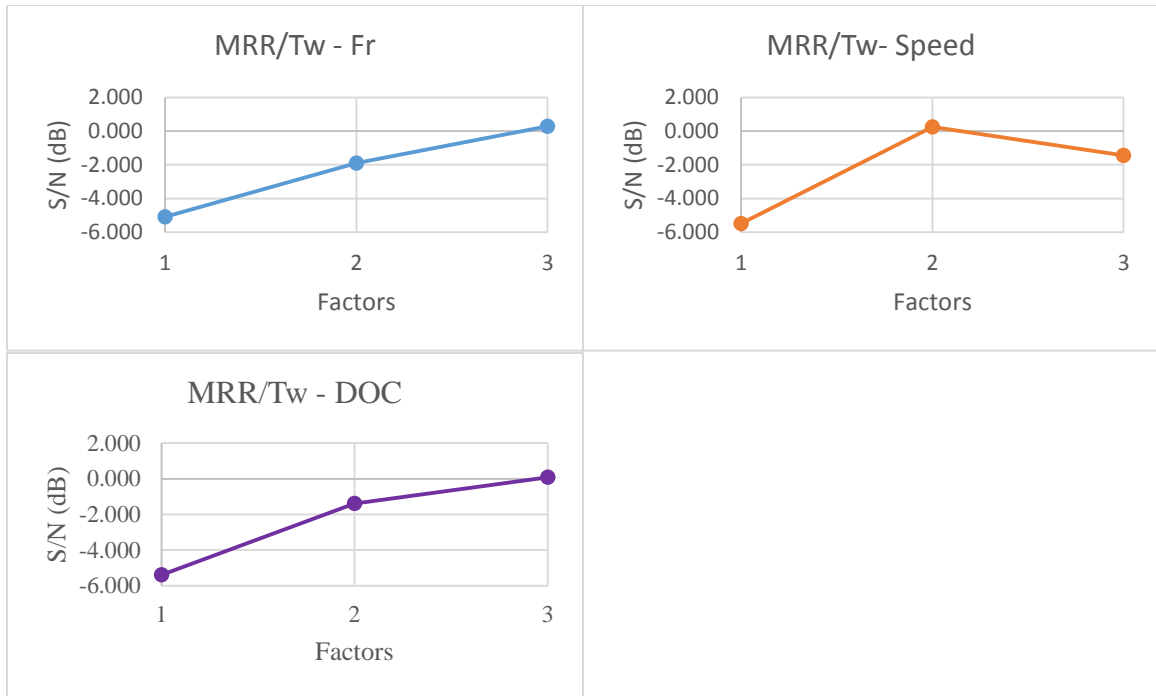
Figure 36. S/N ratio vs Factor Levels of each cutting parameter: Feed Rate, Cutting Speed, and DOC.

From the S/N ratio plots, it can be determined that the most optimal parameters to maximize machining productivity for Fr, Speed, and DOC is 3, 2, and 3, respectively. In terms of their values, the optimal parameters are 762 mm/min, 6500 r/min, and 3 mm. This confirms Vargas et al.'s results, as these parameter match with test number 8, which had the highest machining productivity. Next, an ANOVA can be created to understand the significance of each cutting parameter, as shown in Table 7.

Table 7. Analysis of Variance of MRR/Tw.

ANOVA for MRR/Tw					
Factors	*df*	*SS*	*MS*	Percentage (%)	% Rank
Fr	2	0.3848	0.1924	26.61%	2
V	2	0.4418	0.2209	30.54%	1
DOC	2	0.3847	0.1923	26.59%	3
Error	2	0.2351	0.1176	16.26%	4
Total	8	1.4464		100.00%	

This table shows that cutting speed had the greatest influence on machining productivity followed by feed rate and then DOC. Their percentages are 30.54%, 26.61%, and 26.59%, respectively. Thus, it can be concluded that DOC had the least influence on MRR/Tw. In fact, DOC may have been a major factor in increasing tool wear, which lowers MRR/Tw. For this research, DOC will be kept constant to maximize machining productivity and extend tool life.

3.2.3. Design of Experiment for Cutting Tests and Endurance Tests. After analyzing Vargas et al.'s data, a set of cutting parameters can be defined. Table 8 shows the feed rate (Fr), engagement angle (α_{en}), and cutting speed (V) being used as cutting parameter. These cutting parameters are varied from low to high: 254 mm/min to 1524 mm/min, 30° to 90°, and 3500 r/min to 9500 r/min. As mentioned in the previous section, the DOC will be kept low at 0.5 mm for all cutting tests. A low DOC will ensure lower cutting forces and longer tool life. The slots that will be machined are 9.525 mm in width and 0.5 mm in depth. Additionally, all cutting tests will be run under wet cutting conditions.

Table 8. Variables used as input for DOE.

Variables for Design of Experiment			
Factor Levels	*Parameters*		
	Fr (mm/min)	*α_{en} (°)*	*V (r/min)*
Low - 1	254	30	3500
Med - 2	762	60	6500
High -3	1524	90	9500

These variables are input into a standard L9 orthogonal array to create 9 sets of cutting tests. The standard L9 orthogonal array is shown in Table 9. The numbers ranging from 1

to 3 are the factor levels shown in Table 8. The design of experiment that will be used for the first set of cutting tests are shown in Table 10.

Table 9. L9 orthogonal array used to input variables.

L9 Orthogonal Array - OA(9, 3³, 3)			
Test #	*Parameter 1*	*Parameter 2*	*Parameter 3*
1	1	1	1
2	1	2	2
3	1	3	3
4	2	1	2
5	2	2	3
6	2	3	1
7	3	1	3
8	3	2	1
9	3	3	2

Table 10. DOE with cutting parameters ranging from low to high.

Design of Experiment			
Test #	*Fr (mm/min)*	*α_{en} (°)*	*V (r/min)*
1	254	30	3500
2	254	60	6500
3	254	90	9500
4	762	30	6500
5	762	60	9500
6	762	90	3500
7	1524	30	9500
8	1524	60	3500
9	1524	90	6500

The endurance cutting tests will not have a DOE at this stage of the research as the cutting results must first be analyzed via ANOVA and S/N ratio. After cutting analysis, a DOE can be created for a set of confirmation tests and then endurance tests.

3.3. Experimental Setup

The next section will discuss the experimental setup of machining $AlSiC_p$. This will include sample preparation, cutting tools, and coolant setup, NC code of trochoidal tool path, the dynamometer force acquisition system, measuring tool wear and burr height, and surface roughness measurements. The experiment will be separated into two sets: cutting test and endurance tests. All cutting experiments will be using a CVD diamond coated end mill under wet cutting conditions.

3.3.1. Sample Preparation, Cutting Tools, and Coolant Setup. An $AlSiC_p$ stock piece was cut into small samples of 50 mm x 50 mm x 10 mm for the first set of cutting tests, shown in Figure 38. The samples were cut with an OMAX 55100 abrasive water jet cutting machine at UC Davis, as shown in Figure 37. AWJ machining is known to cut through $AlSiC_p$ quickly and was the preferred method for creating samples.

Figure 37. OMAX 551100 abrasive water jet cutting machine at UC Davis.
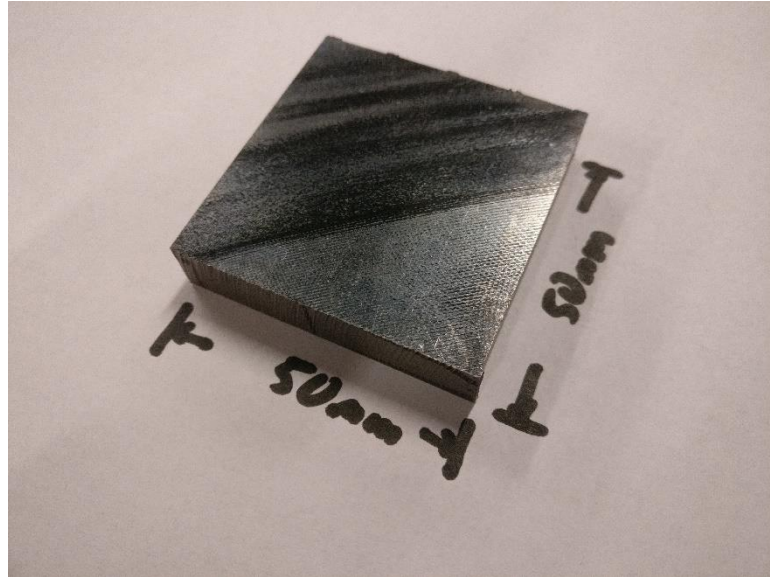
Figure 38. 50 mm x 50 mm x 10 mm AlSiC$_p$ sample.

The AWJ machine produced 3 AlSiC$_p$ samples with a rough surface finish and small taper. These variations were deemed small enough to not have an impact on cutting results. For the endurance tests, a 136.7 mm x 50.3 mm x 26.7 mm AlSiC$_p$ block will be used, as shown in Figure 39. This block was machined down prior to running experiments to ensure each side was flat and square.

Figure 39. 136.7 mm x 50.3 mm x 26.7 mm AlSiC sample for endurance cutting tests.

An inspection vice will be used to secure the workpiece in the Haas VF-1 CNC vertical milling machine. The vice is first inspected to be clear of any chips or debris. A 1x2x3 precision block is used in conjunction with an edge finder to locate the origin of the part. Then the $AlSiC_p$ samples are placed into the vice and clamped down during cutting operations. The first cutting test has two parallels on both sides to secure it in the vice, as shown in Figure 40. The Crystallume CVD diamond coated end mill is placed into a Cat 40 taper tool holder with the Kool Mist spray mist coolant nozzle aimed at the cutting edges. The Kool Mist coolant is magnetized onto the spindle with the external coolant tank secured via toe clamps.
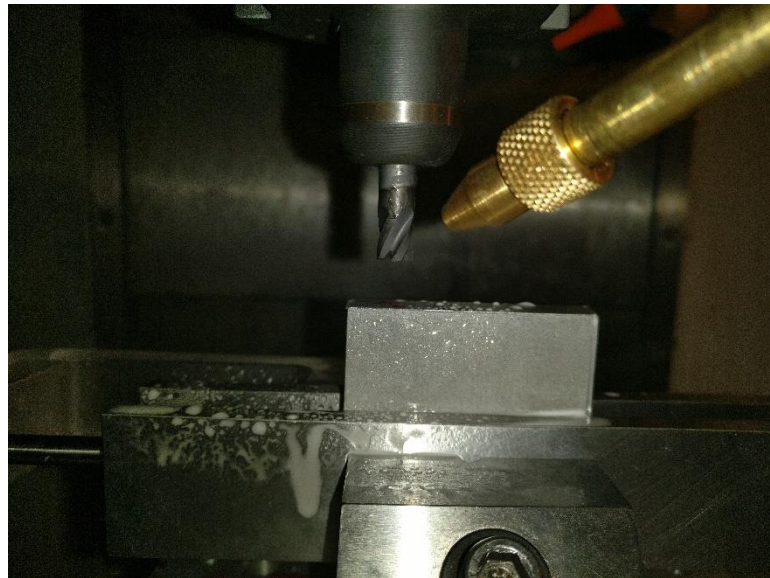
Figure 40. $AlSiC_p$ sample and CVD diamond coated end mill secured with Kool Mist coolant nozzle aimed at the cutting edges.

3.3.2. Trochoidal Tool Path and NC Code. The trochoidal tool path is generated by Esprit CAM 2017. This CAM software was developed by DP Technology and can develop NC codes for 3-axis to 5-axis CNC lathes and milling machines. CAM software is critical to machining productivity as it reduces the time needed to generate G codes and M codes. The combination of G codes and M codes make an NC code that can be interpreted by the CNC machine. This software was provided by University of the Pacific for the School of Engineering and Computer Science.
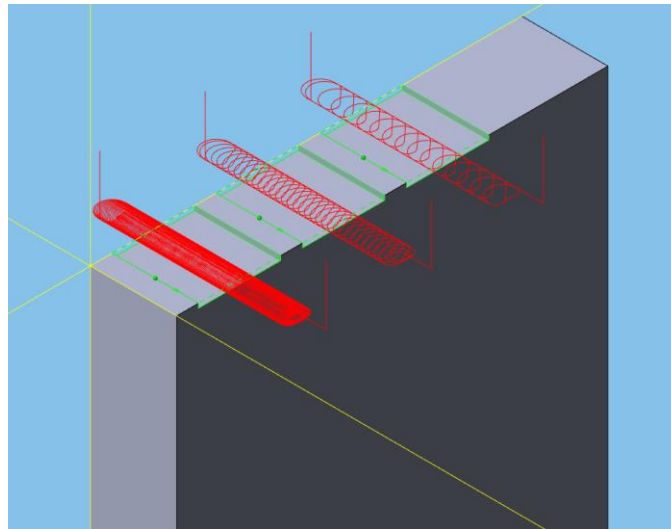
Figure 41. Three sets of trochoidal tool paths generated by Esprit CAM 2017 for cutting tests.

In the Esprit software, a 3D model can be uploaded into the workspace. For the first cutting tests, a model with the sample dimensions and three slots are inserted into Esprit, as shown in Figure 41. The slots are 9.525 mm in width, 0.5 mm in depth, and 10 mm in length. The intersecting yellow lines show the origin of the machining operations. This origin point is the one defined by the edge finder and precision block in the last section. The slots can then be selected and recognized as pocket features. These features help Esprit

define the type of operation that can be performed. Once the slots are defined, a pocket machining operation is selected and the cutting parameters can be inputted. In this case, the trochoidal machining strategy is selected and the feed rate, engagement angle, cutting speed, and DOC is given to the machining operation. A trochoidal tool path is then generated, as shown in Figure 41. The endurance tests are similar to the cutting tests, but a pocket is created on the entire top surface of the samples rather than just in slots, as shown in Figure 42. This is to simulate machining large pockets for an extended period of time.
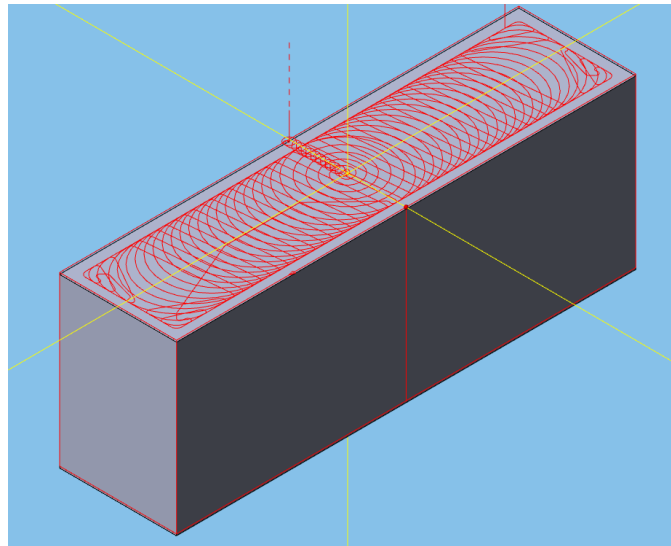
Figure 42. Trochoidal tool path generated by Esprit CAM 2017 for endurance tests.

3.3.3. Dynamometer Force Acquisition System. The cutting forces will be measured by a Kistler Dynamometer Acquisition System Type 5697A paired with a Dual Mode Amplifier Type 5010, as shown in Figure 43. The DAQ Type 5697A has the ability to sample at high rates and can be connected to a PC via USB 2.0 port. The Dual Mode Amplifier Type 5010 converts the DAQ sensor signals to dynamic forces.

(a)
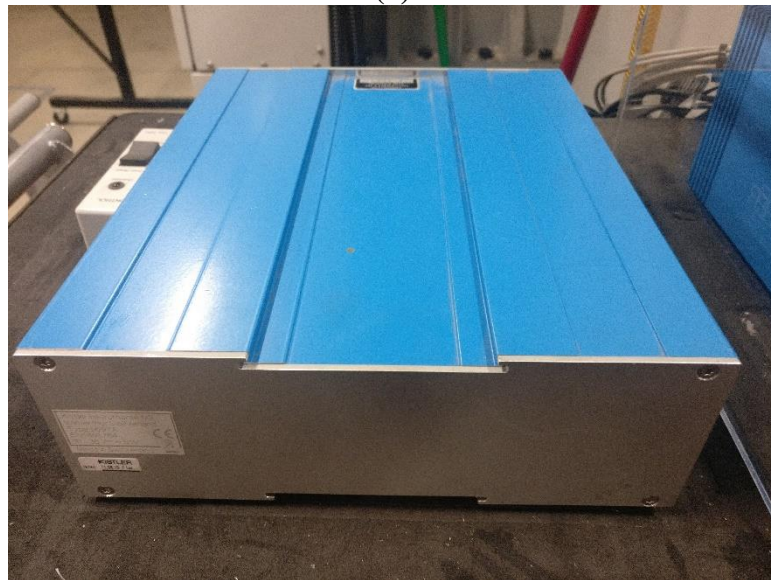
(b)

Figure 43. (a) Dual Mode Amplifier Type 5010 (for 3 channels) (b) DAQ System DynoWare Type 5697A.

The Kistler 3-Component Force Link, as shown in Figure 44, will be used to measure the Fx, Fy, and Fz cutting forces. This component is linked to the Kistler DAQ device and will have the inspection vice mounted onto it. The 3-Component Force Link will be bolted down onto the table of the Hass VF-1 CNC vertical milling machine.
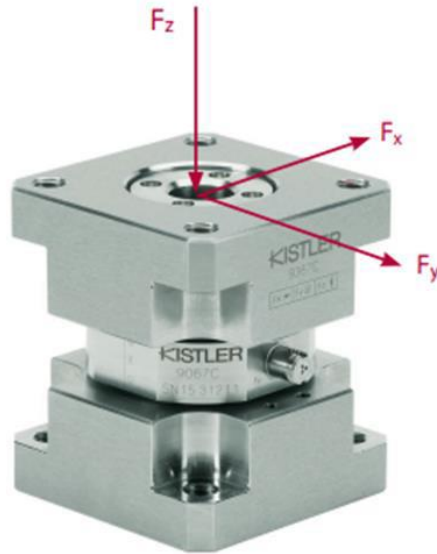
Figure 44. Kistler 3-Component Fx, Fy, and Fz Type 9367C.

3.3.4. Measuring Tool Wear and Burr Height. For this research, the Keyence VHX-2000 Digital Microscope will be used to measure tool wear and burr height, as shown in Figure 45. The quality of the cutting tools will be examined before and after cutting tests. The surface integrity of the machine surface will also be examined for any surface damage.

Figure 45. Keyence VHX-2000 Digital Microscope.

3.3.5. Surface Roughness Measurements. The surface roughness will be measured by a Mitutoyo SURFTEST SJ-301 surface roughness tester, as shown in Figure 46. The arithmetic average roughness (Ra) and maximum roughness (Rz) values will be measured and recorded on a precision granite work table to ensure all samples are flat and even. If the samples are not flat in relation to the surface roughness tester, the measured values will be incorrect. The specifications of the SURFTEST SJ-301 are the following: measuring force 0.75 mN, tip radius 2 μm and a tip angle of 60°. The surface roughness tester is equipped with a retractable standard drive unit that transverses across the sample's surface.

(a)

(b)

Figure 46. (a) Overview of Mitutoyo SURFTEST SJ-301 surface roughness tester (b) Retractable standard drive unit measuring sample's surface.

3.4. Dynamometer Calibration and Overall Setup

The last step for experimental setup is to calibrate the Kistler dynamometer with the DynoWare software. Before running the cutting tests, the DynoWare software is tuned to have the same transducer sensitivity and scale as the Dual Mode Amplifier. Once the settings have been set, an aluminum block of known weight is placed onto the 3-Component Force Link (22.5 N). The weight of the block and the force readings are compared to ensure the dynamometer is operating correctly.

The computer with the DynoWare software is placed in close proximity to the machine. The 3-Component Force Link is bolted down to the Haas VF-1 table and the Spray Mist coolant tank is secured on the side via toe clamps, as shown in Figure 47. Afterwards, the sample rate and measuring time can be inputted for each cutting test. The machine is now ready to be used for the cutting tests.
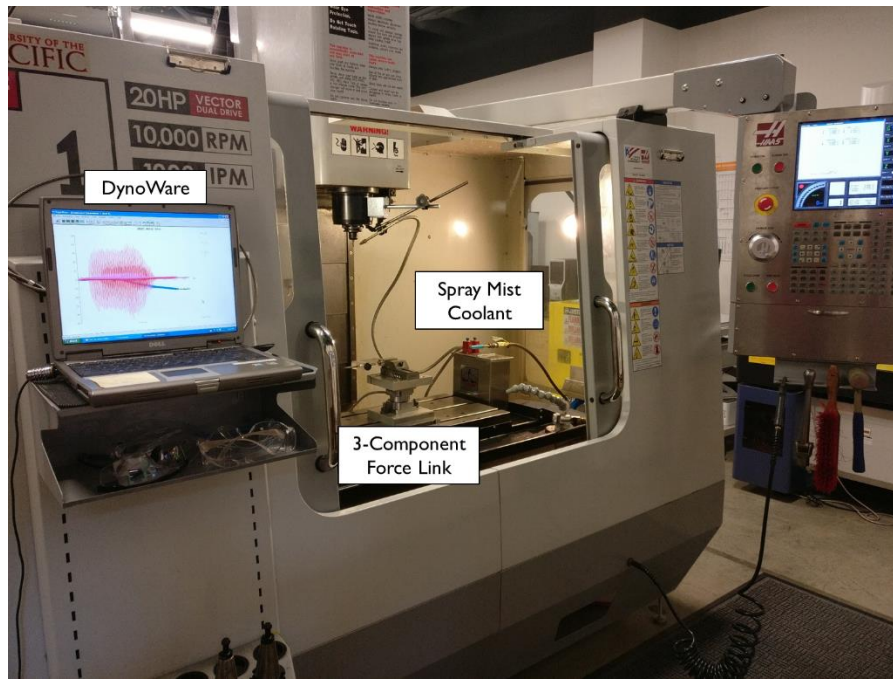
Figure 47. Overall experimental setup showing DynoWare software, Spray Mist Coolant, and 3-Component Fore Link.

Chapter 4: Results and Discussion

4.1. Introduction

This section will divide the cutting experiments into three parts: cutting tests, confirmation tests, and endurance tests. The first cutting tests will be using the DOE created in **Section 3.2.3**. These cutting tests will use CVD diamond coated end mills to create 9.525 mm x 0.5 mm x 10 mm slots. The relationship between the cutting forces, surface roughness, chipload, and MRR will be used to reduce tool wear and burr formation. ANOVA and S/N ratio will be applied to find the optimal cutting parameters. Three sets of cutting parameters based off a combination of MRR, surface roughness, and cutting forces will be used to create 3 sets of confirmation tests. These cutting tests will confirm the optimal cutting parameters for increasing machining productivity and extending tool life. Last, the cutting parameters found in the confirmation tests will be used for the endurance tests. These endurance tests will be applying trochoidal milling to entire face of the workpiece to simulate large pocket operations. The cutting tests are carried out until tool failure is observed. All cutting experiments will be ran under wet cutting conditions.

4.2. Cutting Tests

The cutting tests discussed in this section will be using the DOE described in **Section 3.2.3**. During the cutting tests, the end mill used for experiment 7 was found to have prior tool damage. This tool damage is shown in Figure 48a. As a result, the end mill experienced excessive crater wear after the cutting tests, as shown in Figure 48b. The end mill used in experiment 3 is used again to perform cutting test 7. The CVD diamond coated

end mill was checked for any prior tool wear to ensure accurate results. The remaining

cutting test results will be discussed in the following sections.

(a)	**(b)**
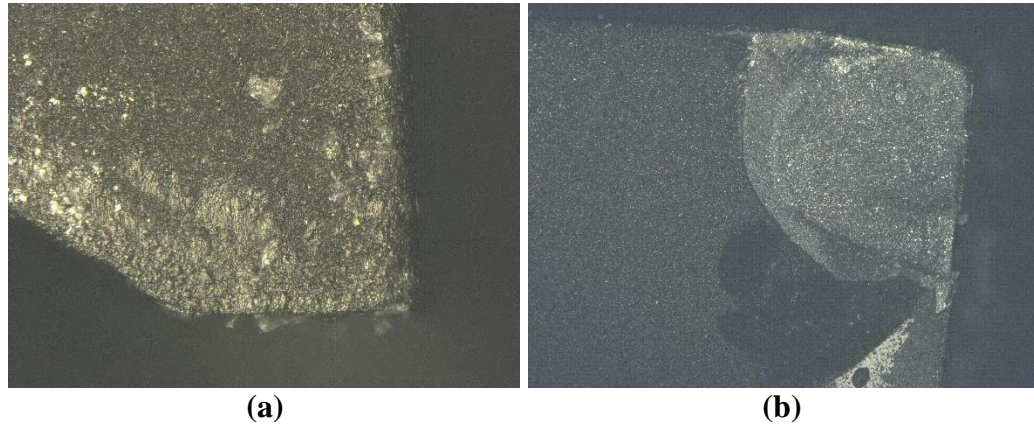
Figure 48. (a) Tool damage on CVD diamond coated end mill prior to cutting test 7 (b) Crater wear from prior tool damage after cutting test 7.

      4.2.1. Kistler Raw Cutting Force Results. The Kistler DynoWare software is

used to gather the raw cutting force data for all cutting experiments. The DynoWare

software gathers data within a specified time interval. A sample of the raw cutting force

data produced by the DynoWare is shown in Figure 49. The raw data provides an overview

of the cutting forces but does not provide insight into the significance of the cutting

parameters. The cutting force data will need further post processing to analyze the cutting

interaction between the CVD diamond coated end mills and AlSiC$_p$.
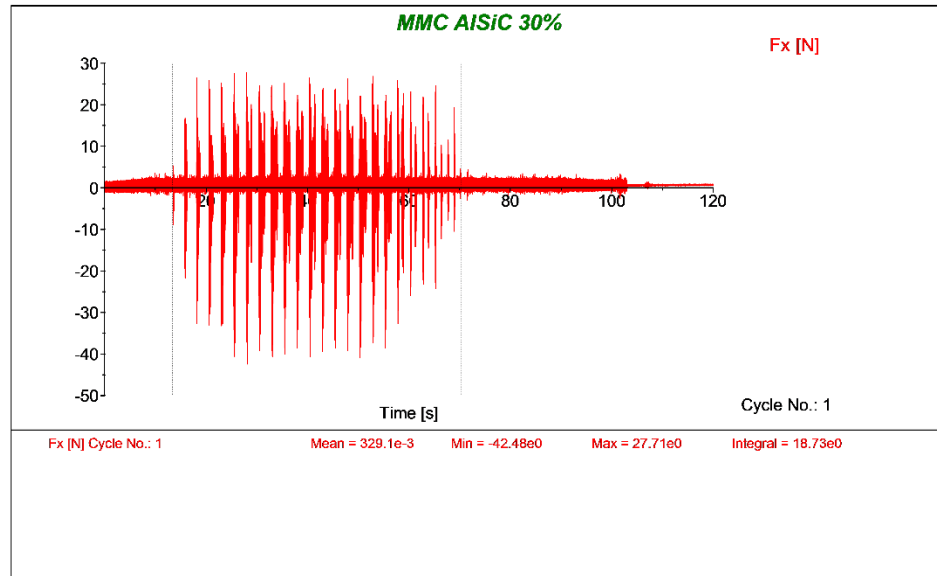
Figure 49. Sample of raw cutting force data in the x-direction from Kistler DynoWare.

4.2.2.   Cutting Force Results Discussion. Excel will be used as a post processor for the raw cutting force data. Rather than focus on the entire time interval, the cutting forces can be analyzed in smaller portions to understand the cutting interaction. The cutting force data is taken into 10 second intervals, as shown in Figure 50. These plots of the Fx and Fy cutting forces show the cutting interaction of the CVD diamond coated end mills and AlSiC$_p$ for multiple trochoidal tool passes. The Fz component is omitted due to the coolant pressure creating noise in the z-direction. This noise could alter the significance of the Fz component as the actual cutting force is small in comparison to Fx an Fy.
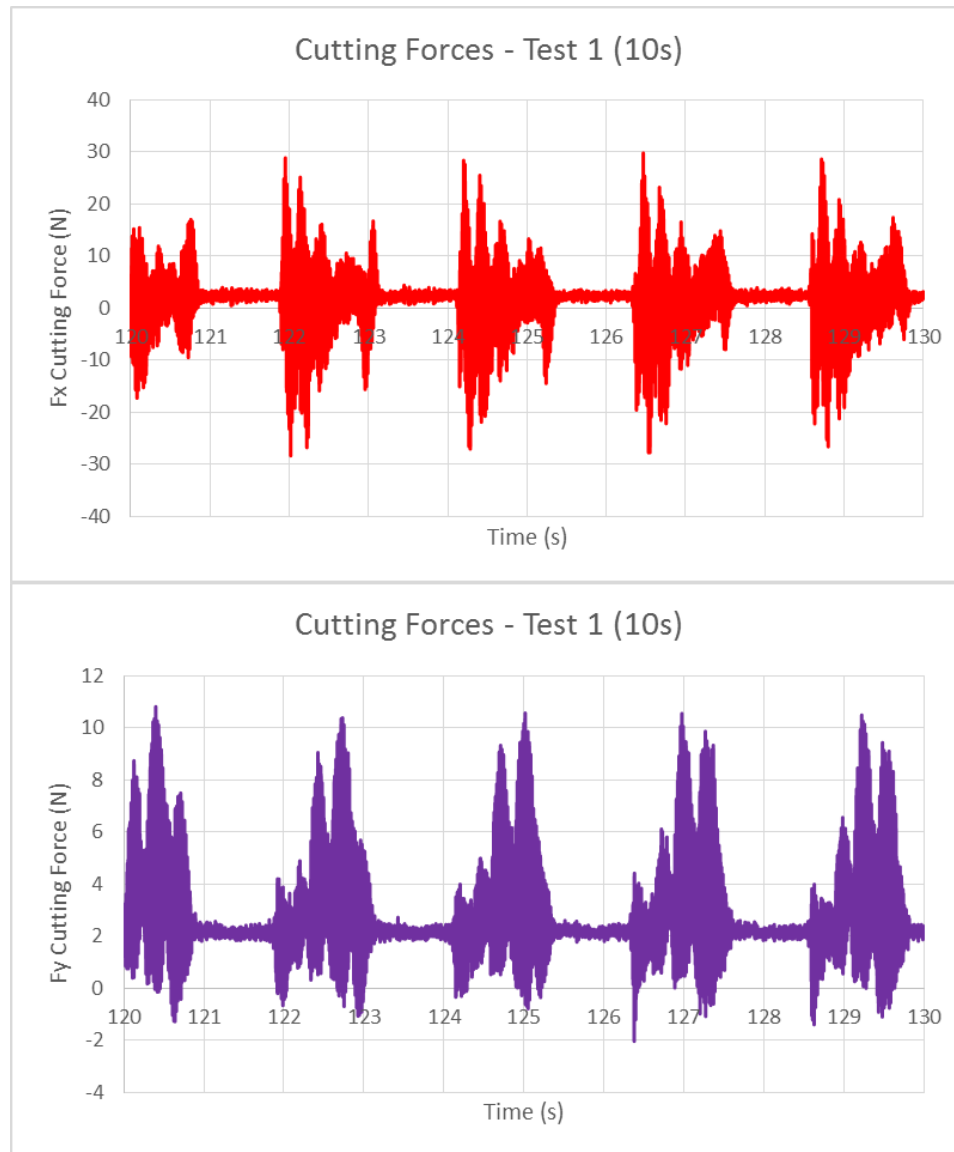
Figure 50. Sample of cutting force data in a 10 second time interval (Fx and Fy).

From the cutting force data in Figure 50, it can be concluded that each machining pass is similar. The cutting force data can be truncated further to one trochoidal pass for easier analysis, as shown in Figure 51. These plots show the cutting interaction of the CVD diamond end mill against the AlSiC$_p$ in higher clarity than the original raw cutting data.
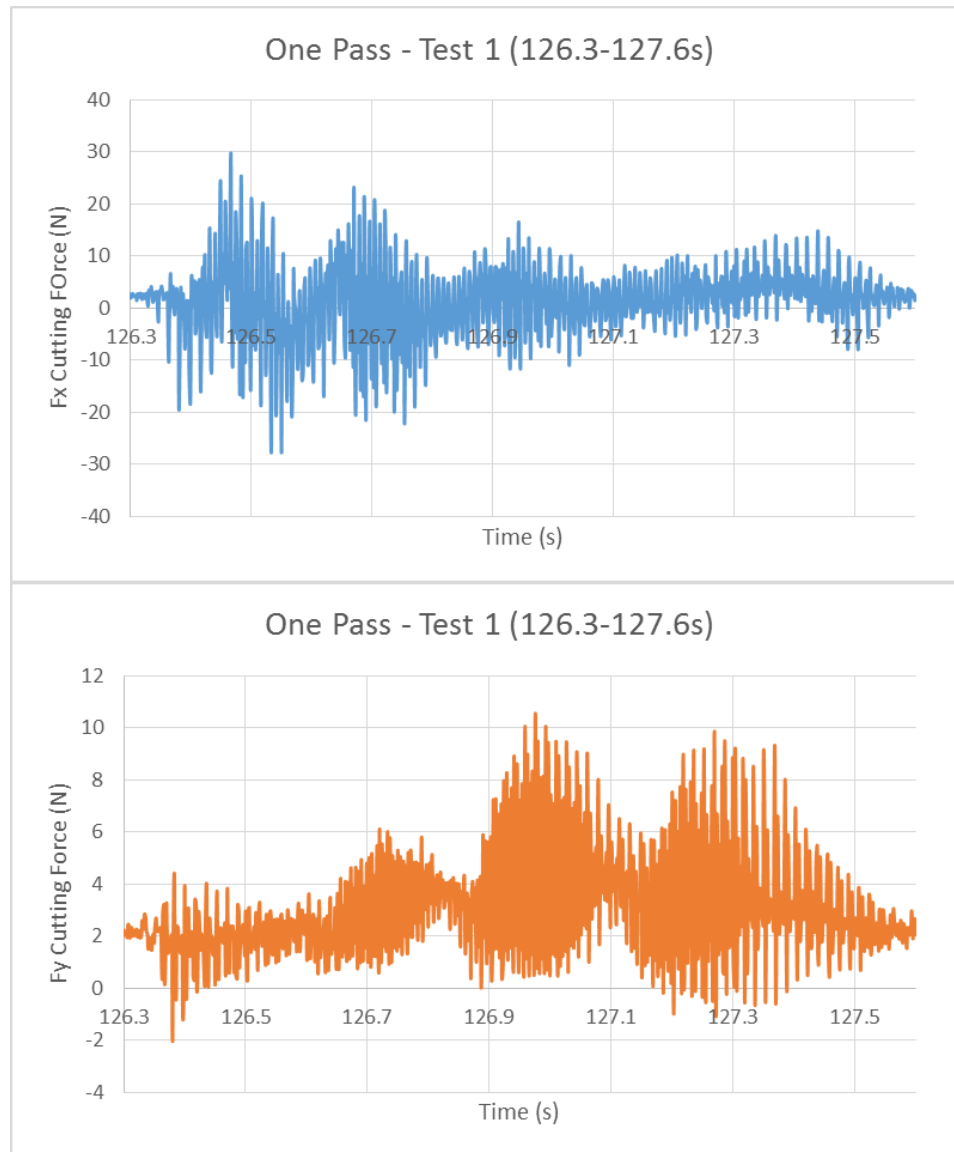
Figure 51. Sample of cutting force data for one trochoidal pass (Fx and Fy).

The average and max cutting forces are found for all 9 cutting experiments and tabulated into Table 11. The cutting force data for one trochoidal pass with CVD diamond coated end mills are compared to their cutting parameters. Fx represents the cutting force in the normal direction, Fy represents the cutting force in the cutting direction, and Fxy represents the combined cutting force. The average cutting forces in the x and y-direction were relatively similar for all 9 cutting experiments. However, Fx was greater than Fy when

examining the max cutting forces. The greatest max cutting force was found in experiment 5 with 118.20 N, 15.41 N, and 119.20 N, for Fx, Fy, and Fxy respectively. It can be expected that if there was tool damage or tool wear, it would occur in experiment 5. This will be examined in the tool wear section.

Table 11. Average and max cutting force results for Cutting Test compared to cutting parameters.

Test No.	Avg. [1P] (N)			Max Cutting Forces (N)			Parameters		
	Fx	*Fy*	Avg Fxy	*Fx*	*Fy*	*Fxy*	*Fr (mm/min)*	α_{en} *(°)*	*V (rpm)*
1	1.56	3.00	3.38	29.79	10.80	31.68	254	30	3500
2	0.27	2.33	2.34	40.68	16.88	44.04	254	60	6500
3	0.45	2.54	2.58	35.64	9.06	36.78	254	90	9500
4	0.16	1.57	1.58	33.14	11.78	35.17	762	30	6500
5	1.56	3.59	3.91	**118.20**	**15.41**	**119.20**	762	60	9500
6	7.77	9.10	11.97	76.78	30.88	82.76	762	90	3500
7	0.08	0.08	0.11	61.37	2.01	61.40	1524	30	9500
8	5.26	4.44	6.88	82.03	29.97	87.33	1524	60	3500
9	7.97	8.04	11.32	116.30	30.98	120.36	1524	90	6500

The cutting force data for the average and max cutting forces can be plotted to observe a trend in cutting forces relative to each cutting test. These plots are shown in Figure 52 and Figure 53. The highest average cutting force is found in experiment 6 while the highest max average cutting force is in experiment 5 and 9. A possible explanation for the difference in peaks may be due to the CVD diamond coated end mills cutting larger SiC particles. These particle interactions can drastically affect max cutting forces. These variation can be a major issue when optimizing the cutting parameters.
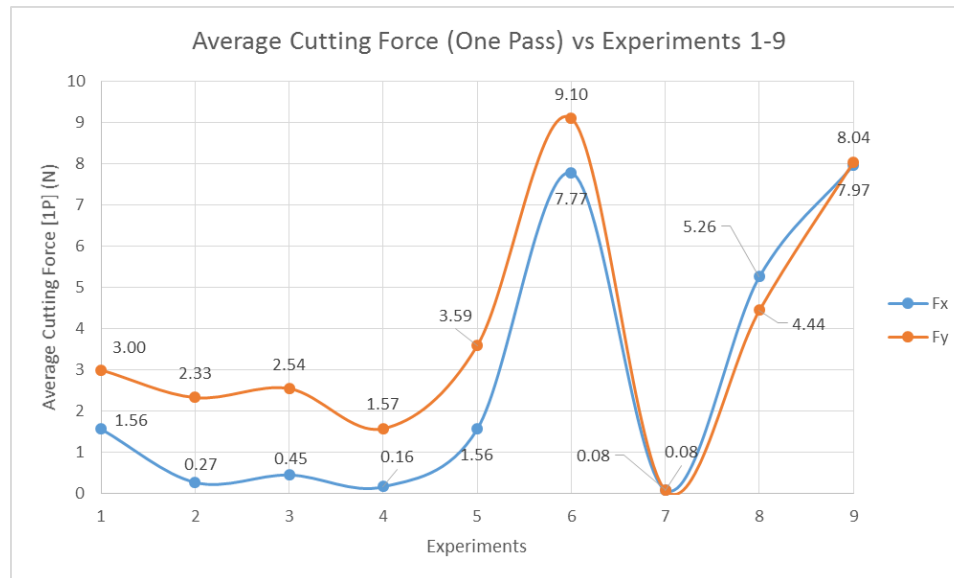
(a)
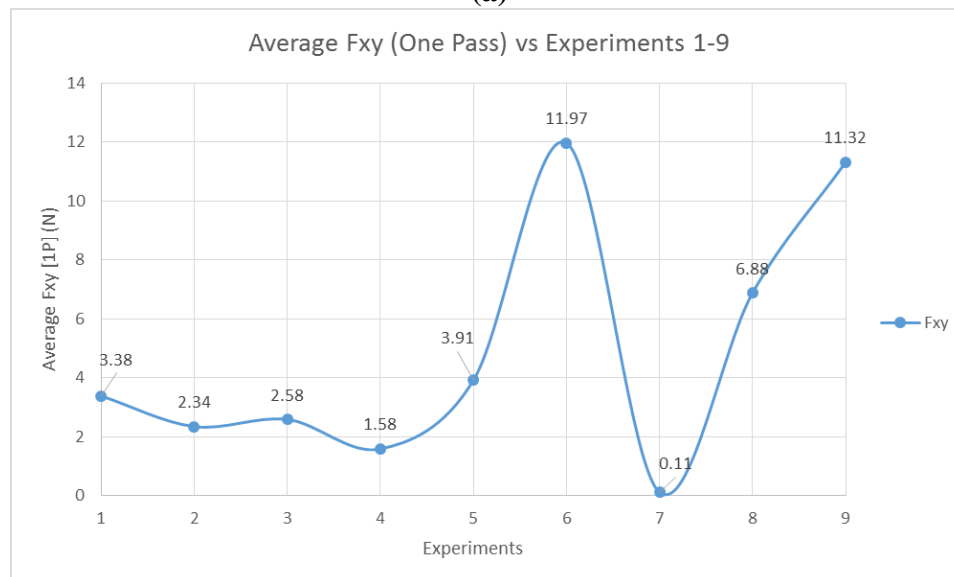
(b)

Figure 52. Average cutting force graphs for one trochoidal pass (a) Fx and Fy (b) Fxy.
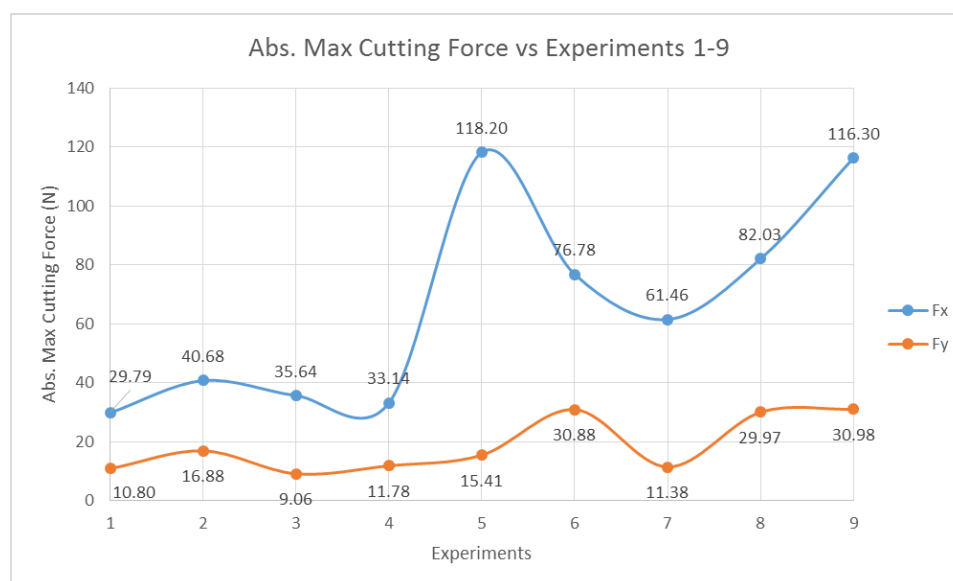
(a)
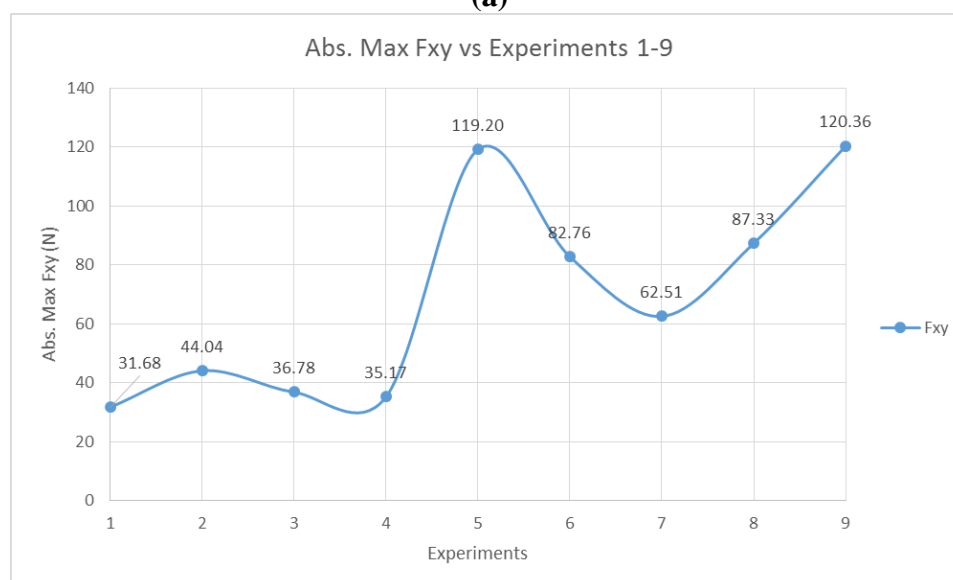
(b)

Figure 53. Max cutting force graph (a) Fx and Fy (b) Fxy.

In order to determine whether to optimize the cutting parameters based off the average or max cutting forces, an analysis of variance can be performed. The ANOVA for average Fxy and max Fxy is shown in Table 12 and 13. This data will study the significance of each cutting parameter and determine which set of cutting forces will be used for further analysis.

Table 12. ANOVA for average Fxy cutting forces for one trochoidal pass.

ANOVA for Avg. Fxy (One Pass)							
Factors	*df*	*SS*	*MS*	*F-Ratio*	*P-Value*	*Percentage*	*% Rank*
Fr	2	20.53	10.26	2.15	0.318	14.24%	3
α_{en}	2	73.29	36.64	7.66	0.115	50.82%	1
V	2	40.82	20.41	4.27	0.190	28.31%	2
Error	2	9.57	4.78			6.63%	4
Total	8	144.20	18.03			100.00%	

Table 13. ANOVA for max Fxy cutting forces.

ANOVA for Absolute Max Fxy							
Factors	*df*	*SS*	*MS*	*F-Ratio*	*P-Value*	*Percentage*	*% Rank*
Fr	2	4563.73	2281.86	2.03	0.330	45.92%	1
α_{en}	2	3059.56	1529.78	1.36	0.424	30.79%	2
V	2	62.81	31.41	0.03	0.973	0.63%	4
Error	2	2251.44	1125.72			**22.66%**	3
Total	8	9937.54	1242.19			100.00%	

The influence of each cutting parameter is ranked from 1 to 4 based off their effect on the cutting forces. The engagement angle had the greatest influence on the average cutting forces, as shown in Table 12. The feed rate had the greatest influence on the max cutting forces, as shown in Table 13. However, the difference between the two sets of data is the error percentage. The error is 6.63% for the average cutting forces and 22.66% for the max cutting forces. This error represents the noise variation in the cutting test. The noise variation could be from the experimental setup or other factors like the cutting interaction between the CVD diamond coated end mills and SiC particles.

The average cutting forces was chosen to be studied in relation to machining productivity. The lower error percentage shows that the average cutting forces can be more easily controlled by optimizing the cutting parameters. The following section will study the tool wear from these cutting forces.

4.2.3. Tool Wear Results Discussion. The tool wear analysis is an important step in optimizing the cutting parameters like feed rate, engagement angle, and cutting speed. The study of tool wear allows researchers to understand the effects of each cutting parameter on the cutting tool. Figure 54 shows some of the possible tool wear mechanisms found during the cutting tests. Experiment 1 and 6 shows signs of crater wear while experiments 4, 5, 8, and 9 shows BUE.

(a) Exp. 1   **(b) Exp. 4**

(c) Exp. 5   **(d) Exp. 6**

(e) Exp. 8   **(f) Exp. 9**
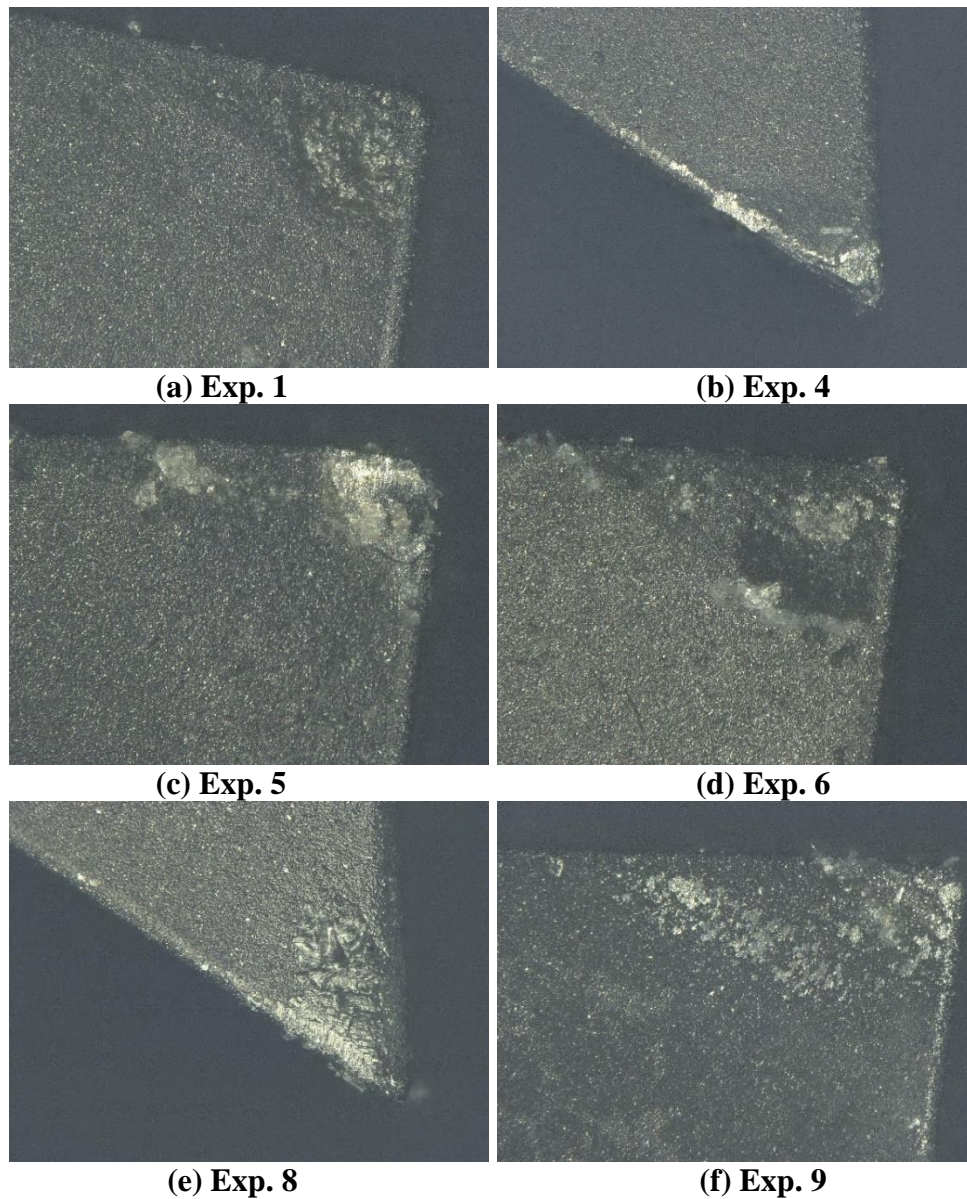
Figure 54. (a)(d) Crater wear (b)(e) Light BUE on cutting tip (c)(f) Light BUE on rake face.

A major concern when machining AlSiC$_p$ is maintaining tool geometry. Experiment 5 showed the highest max cutting force and will be analyzed for tool damage. Figure 55 shows the measured corner radius for all 4 cutting edges. There were no signs of tool damage and the corner radius was in pristine condition. The average corner radius was 31.3 μm.

| **(a) Corner 1: 30.9 μm** | **(b) Corner 2: 32.8 μm** |
| **(c) Corner 3: 35.0 μm** | **(d) Corner 4: 26.4 μm** |
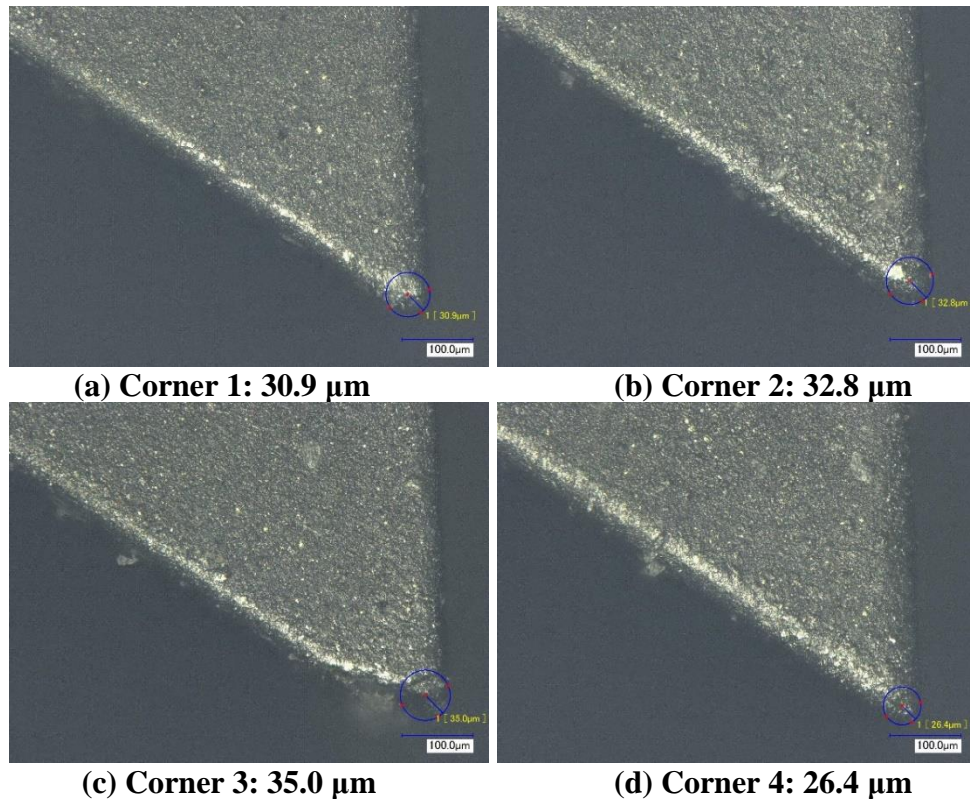
Figure 55. Corner radius measurement of cutting tool 5: average corner radius 31.3 μm.

When comparing the tool wear found in this research to Vargas et al.'s tool wear, it can be concluded that trochoidal milling has improved the tool life. When Vargas et al. performed their experiments, all their cutting tests had flank wear with the diamond coating stripped. The experiments performed in this research had the diamond coating intact and in nearly pristine condition.

4.2.4. Surface Roughness Results Discussion. The surface quality is a critical parameter to consider when making a product. The dimensional stability of a product can determine whether it will function properly. The average (Ra) and maximum (Rz) surface roughness values are given in Table 14 and 15. Each slot is measured 3 times at different locations and then averaged. All cutting tests showed low surface roughness values and is considered ideal for many applications. The surface roughness trend for Ra and Rz are similar and thus only Ra will be considered for the optimization of machining productivity.

Table 14. Average surface roughness values for experiments 1 to 9 (Ra).

Ra			
Test No.	*(μm)*		*Avg.*
1	0.70	0.77	0.85	0.77
2	1.04	1.05	0.76	0.95
3	0.62	0.55	0.55	0.57
4	0.72	0.91	0.95	0.86
5	0.77	0.74	0.51	0.67
6	0.90	0.92	0.85	0.89
7	0.74	0.59	0.96	0.76
8	1.11	1.15	1.14	1.13
9	1.14	1.31	1.46	1.30

Table 15. Maximum surface roughness values for experiments 1 to 9 (Rz).

Rz			
Test No.	*(μm)*		*Avg.*
1	5.50	6.73	5.83	6.02
2	7.21	7.22	5.84	6.76
3	5.18	4.98	5.55	5.24
4	5.63	6.24	7.32	6.40
5	6.12	6.76	4.71	5.86
6	6.89	7.02	7.06	6.99
7	5.32	5.23	8.26	6.27
8	8.24	8.79	8.23	8.42
9	8.27	9.58	9.89	9.25

4.2.5. Chip Load-Based Analysis. Chip load is a popular method for measuring and optimizing machining productivity. The chip load is the thickness of the material removed by each cutting edge during a cut. This can be found by dividing feed rate and cutting speed and then dividing it by the total cutting edges. The chip load data is shown in Table 16. The chip load is then re-organized from lowest to highest, as shown in Table 17. The average cutting forces and surface roughness values are given to compare the effects of chip load.

Table 16. Chip Load for experiments 1 to 9.

Chip Load	
Test No.	*(ipt)*
1	0.000714
2	0.000385
3	0.000263
4	0.001154
5	0.000789
6	0.002143
7	0.001579
8	0.004286
9	0.002308

Table 17. Chip Load from lowest to highest in comparison to cutting forces and surface roughness values.

	Avg. Cutting Forces [1P] (N)			Ra
Chip load	*Fx*	*Fy*	*Fxy*	*(μm)*
0.000263	0.45	2.54	2.58	0.57
0.000385	0.27	2.33	2.34	0.95
0.000714	1.56	3.00	3.38	0.77
0.000789	1.56	3.59	3.91	0.67
0.001154	0.16	1.57	1.58	0.86
0.001579	0.08	0.08	0.11	0.76
0.002143	7.77	9.10	11.97	0.89
0.002308	7.97	8.04	11.32	1.30
0.004286	5.26	4.44	6.88	1.13

The data is then plotted for Fxy vs Chip Load and Ra vs Chip Load, as shown in Figure 56 and 57. These graphs are valuable because they show the optimal chip load for this type of material. The lowest cutting forces was found to be around 0.00158 ipt while the lowest surface roughness values was found at 0.00263 ipt.
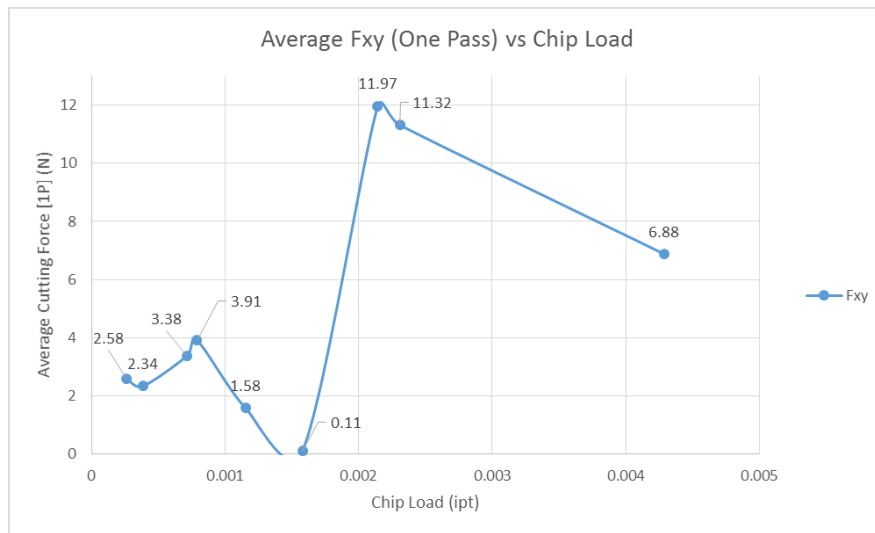
Figure 56. Average cutting forces over varying chip loads.
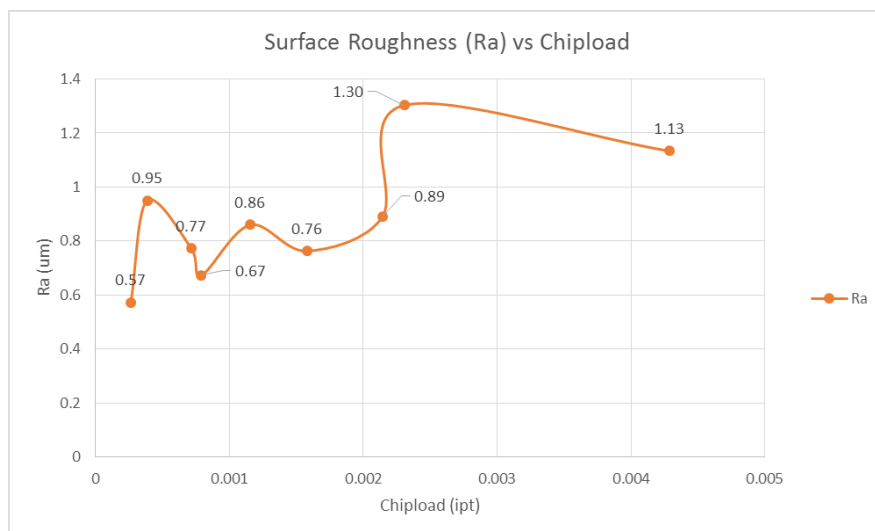
Figure 57. Surface roughness values over varying chip loads.

4.2.6.   Optimizing Cutting Parameters with ANOVA and S/N Ratio. Although

chip load is a common measurement used to determine how to cut a material, it is not an

accurate measurement of machining productivity. Material removal rate (MRR) is a better

measurement of machining productivity because it represents the volume removed per unit

time. The MRR is calculated by multiplying the depth of cut, width of cut, and feed rate,

as shown in Table 18. The width of cut is found by multiplying the diameter of the cutting

tool by the ratio of the engagement angle by 180°, where 180° represents the end mill being

full engaged.

Table 18. Surface roughness, average cutting force, and material removal rate values used for cutting parameter optimization.

	Ra	**Avg. Fxy**	**MRR**
Test No.	*μm*	N	*cm³/min*
1	0.773	1.26	0.134
2	0.950	2.21	0.269
3	0.573	3.05	0.403
4	0.860	4.09	0.403
5	0.673	5.05	0.806
6	0.890	6.07	1.210
7	0.763	7.04	0.806
8	1.133	8.08	1.613
9	1.303	9.09	2.419

The surface roughness, average cutting force, and material removal rate can be compared

to optimize the cutting parameters. These cutting results represent surface integrity, tool

life, and machining efficiency. However, in order to compare these results, the data has to

be normalized. The normalized data is shown in Table 19. This data scales the values from

0 to 1 and determines the fitness of each cutting test with respect to the cutting results.

Experiment 3 had the highest fitness value for Ra, experiment 7 had the highest fitness value for average Fxy and experiment 9 had the highest fitness value for MRR.

Table 19. Normalized data of surface roughness, average cutting force, and material removal rate.

Normalized Data			
	Ra	**Avg. Fxy [1P]**	**MRR**
Test No.	*Fitness Value (0-1)*	*Fitness Value (0-1)*	*Fitness Value (0-1)*
1	0.726	0.724	0.000
2	0.484	0.812	0.059
3	**1.000**	0.792	0.118
4	0.607	0.876	0.118
5	0.863	0.679	0.294
6	0.566	0.000	0.471
7	0.740	**1.000**	0.294
8	0.233	0.429	0.647
9	0.000	0.055	**1.000**

Next, a combination of MRR, Avg. Fxy, and Ra can be added together to find the cutting test that is most fit. A combination of MRR+AvgFxy+Ra, MRR+AvgFxy, and MRR+Ra is created and shown in Table 20. The first set of combinations represent the fitness value for machining efficiency, tool life, and surface integrity. The second set of combinations represent only machining efficiency and tool life. The last set of combinations represent machining efficiency and surface integrity. Experiment 7 was found to be the most fit for the first two combinations with 2.03 and 1.29, respectively, while experiment 5 was the most fit for the last set of combinations with 1.16.

Table 20. Combination of MRR, Avg. Fxy, and Ra for best fitness value.

	MRR-Based Fitness Value		
	MRR+AvgFxy+Ra	**MRR+AvgFxy**	**MRR+Ra**
Test No.	*Fitness Value (0-3)*	*Fitness Value (0-2)*	*Fitness Value (0-2)*
1	1.45	0.72	0.73
2	1.35	0.87	0.54
3	1.91	0.91	1.12
4	1.60	0.99	0.72
5	1.84	0.97	**1.16**
6	1.04	0.47	1.04
7	**2.03**	**1.29**	1.03
8	1.31	1.08	0.88
9	1.05	1.05	1.00

An analysis of variance is performed to determine the significance of each cutting parameter with respect to the three combinations stated earlier. The cutting speed was found to be the most significant cutting parameter for MRR+AvgFxy+Ra and MRR+Ra. The feed rate was the most significant cutting parameter for MRR+AvgFxy.

Table 21. Analysis of variance for MRR+Avg.Fxy+Ra. Shaded area represents the most significant cutting parameter.

	ANOVA for MRR+AvgFxy+Ra				
Factors	*df*	*SS*	*MS*	*Percentage*	*% Rank*
Fr	2	0.018	0.009	1.74%	4
α_{en}	2	0.196	0.098	18.75%	2
V	2	0.790	0.395	75.38%	1
Error	2	0.043	0.022	4.13%	3
Total	8	1.048	0.131	100.00%	

Table 22. Analysis of variance for MRR+Avg.Fxy. Shaded area represents the most significant cutting parameter.

	ANOVA for MRR+AvgFxy				
Factors	*df*	*SS*	*MS*	*Percentage*	*% Rank*
Fr	2	0.203	0.101	46.88%	1
α_{en}	2	0.064	0.032	14.85%	3
V	2	0.145	0.073	33.58%	2
Error	2	0.020	0.010	4.69%	4
Total	8	0.433	0.054	100.00%	

Table 23. Analysis of variance for MRR+Ra. Shaded area represents the most significant cutting parameter.

ANOVA for MRR+Ra					
Factors	*df*	*SS*	*MS*	*Percentage*	*% Rank*
Fr	2	0.062	0.031	17.96%	3
α_{en}	2	0.088	0.044	25.19%	2
V	2	0.185	0.093	53.32%	1
Error	2	0.012	0.006	3.53%	4
Total	8	0.347	0.043	100.00%	

The signal-to-noise ratio can be applied to these combinations to determine the optimal cutting parameters for each set of combinations. These cutting parameters can be used for confirmation tests to verify the results. Equation 5 will be used to maximize the largest signal and minimize the noise for each combination set. The S/N ratio of each combination is shown in Table 24.

Table 24. Signal-to-Noise ratio for each combination of cutting parameters.

	MRR+AvgFxy+Ra	**MRR+AvgFxy**	**MRR+Ra**
Test No.	$(S/N)_L$ *(dB)*	$(S/N)_L$ *(dB)*	$(S/N)_L$ *(dB)*
1	3.23	-2.80	-2.78
2	2.64	-1.20	-5.31
3	5.62	-0.83	0.97
4	4.09	-0.05	-2.79
5	5.28	-0.23	1.27
6	0.31	-6.55	0.31
7	6.17	2.24	0.29
8	2.34	0.64	-1.11
9	0.46	0.46	0.00

The average S/N ratio for all three combinations are found in Table 25-27 and the plots are given in Figures 58-60.

Table 25. Average Signal-to-Noise ratio for MRR+AvgFxy+Ra.

MRR+AvgFxy+Ra					
Feed Rate		Engagement Angle		Cutting Speed	
Sum	*Avg. S/N*	*Sum*	*Avg. S/N*	*Sum*	*Avg. S/N*
11.48	3.83	13.48	4.49	5.88	1.96
9.68	3.23	10.25	3.42	7.19	2.40
8.97	2.99	6.39	2.13	17.06	5.69
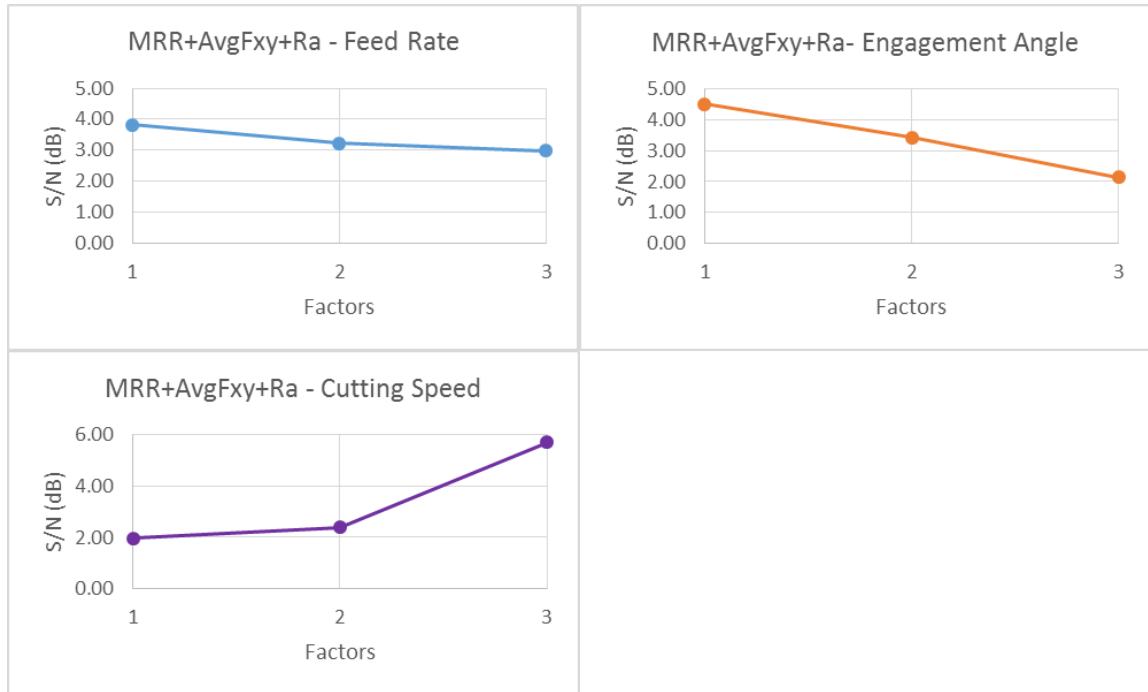
Figure 58. Plots of average S/N ratios for MRR+AvgFxy+Ra.

Table 26. Average Signal-to-Noise ratio for MRR+AvgFxy.

MRR+AvgFxy					
Feed Rate		Engagement Angle		Cutting Speed	
Sum	*Avg. S/N*	*Sum*	*Avg. S/N*	*Sum*	*Avg. S/N*
-4.83	-1.61	-0.62	-0.21	-8.71	-2.90
-6.83	-2.28	-0.80	-0.27	-0.79	-0.26
3.34	1.11	-6.91	-2.30	1.18	0.39
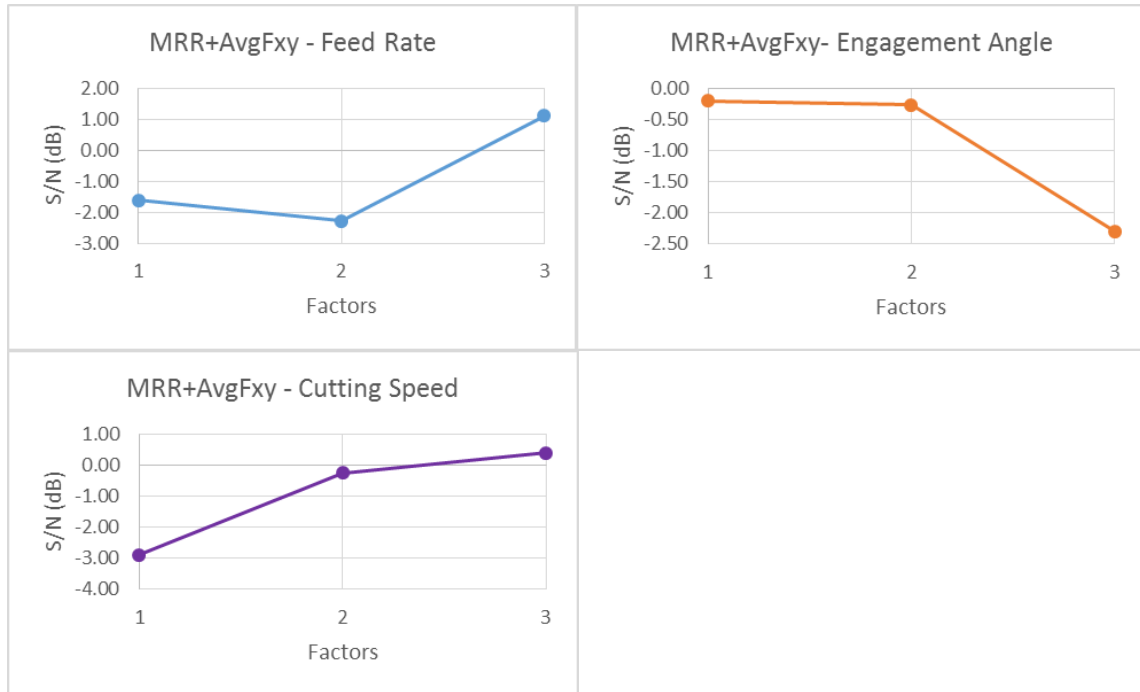
Figure 59. Plots of average S/N ratios for MRR+AvgFxy.

Table 27. Average Signal-to-Noise ratio for MRR+Ra.

MRR+Ra					
Feed Rate		**Engagement Angle**		**Cutting Speed**	
Sum	*Avg. S/N*	*Sum*	*Avg. S/N*	*Sum*	*Avg. S/N*
-7.12	-2.37	-5.29	-1.76	-3.58	-1.19
-1.21	-0.40	-5.15	-1.72	-8.10	-2.70
-0.82	-0.27	1.28	0.43	2.52	0.84
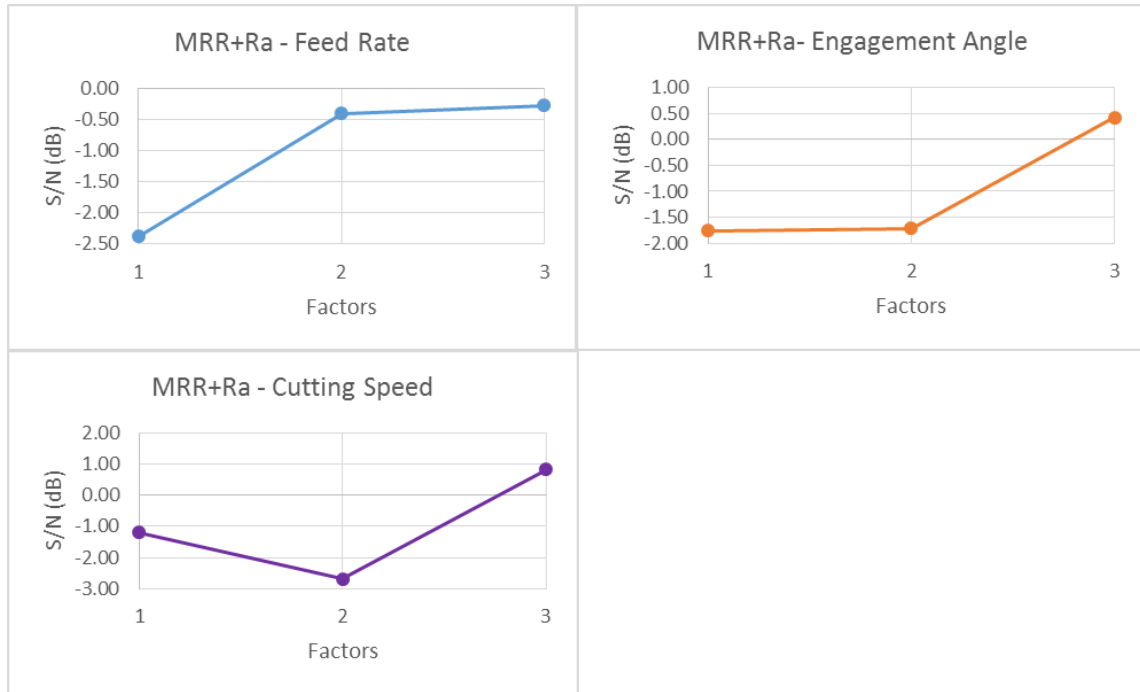
Figure 60. Plots of average S/N ratios for MRR+Ra.

The results from these S/N ratio plots show that the optimal cutting conditions are 254 mm/min, 30°, and 9500 r/min for MRR+AvgFxy+Ra, 1524 mm/min, 30°, and 9500 r/min for MMR+AvgFxy, and 1524 mm/min, 90°, and 9500 r/min for MRR+Ra.

4.3. Confirmation Tests

The optimal cutting parameters found in the last section will be used to confirm the results of the cutting tests. The design of experiment for the confirmation tests are found in Table 28.

Table 28. Design of experiment for confirmation tests.

Design of Experiment			
Test No.	*Fr (mm/min)*	α_{en} *(°)*	*V (r/min)*
1	254	30	9500
2	1524	30	9500
3	1524	90	9500

4.3.1. Cutting Results Discussion. The cutting results for the confirmation tests are given in Table 29. The cutting forces, surface roughness values, and material removal rate was found for comparative analysis.

Table 29. Surface roughness, material removal rate, and average cutting forces for confirmation tests.

Confirmation Cutting Tests					
	Ra	**MRR**	**Avg. [1P] (N)**		
Test No.	*Avg.*	*cm³/min*	*Fx*	*Fy*	*Avg Fxy*
1	0.20	0.134	0.482	1.759	1.824
2	0.72	0.806	0.928	0.877	1.277
3	0.70	2.419	3.923	4.379	5.879

The cutting forces are plotted and shown in Figure 61. The cutting force graphs confirm the optimization of cutting forces for experiment 1 and 2. The Fxy values were found to be 1.82 N and 1.28 N, respectively, which was lower than experiment 3 with 5.88 N. Experiment 3 had higher cutting forces because it did not consider optimizing cutting forces but rather material removal rate and surface roughness.

(a)
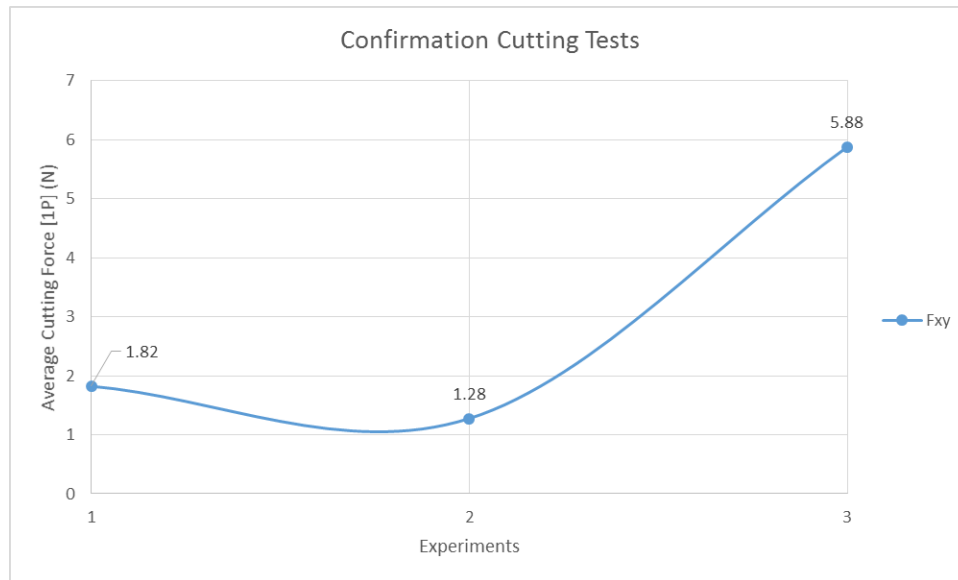
(b)

Figure 61. Average cutting force graphs for confirmation tests (a) Fx and Fy (b) and Fxy.

Similar to the cutting tests, the cutting results can be normalized to scale from 0 to 1, as shown in Table 30. The Ra value is highest for experiment 1 with 1.511 while Avg. Fxy is highest for experiment 2 and MRR is highest for experiment 3. Increasing MRR is known to increase cutting forces due to being a more aggressive machining process. As a result, MRR is highest for experiment 3 because it does not take into consideration cutting forces.

Table 30. Normalized data of surface roughness, average cutting forces, and material removal rate for confirmation tests.

Confirmation Tests Normalized Data			
	Ra	**Avg. Fxy**	**MRR**
Test No.	*Fitness Value (0-1)*	*Fitness Value (0-1)*	*Fitness Value (0-1)*
1	**1.511**	0.856	0.000
2	0.799	**0.902**	0.294
3	0.822	0.514	**1.000**

The normalized data is then added together based off the experiments' set of combinations, as shown in Table 31. When comparing these values to the values found in the cutting tests it can be concluded that confirmation tests were more optimized. For MRR+AvgFxy+Ra, the confirmation tests had 2.37 while the cutting test highest had 2.01. For MRR+Ra, the confirmation tests had 1.82 while the cutting test highest had 1.16. However, for MRR+AvgFxy, the confirmation test had 1.20 while the cutting test highest had 1.29. The reason for this is because the cutting parameters were the same for the confirmation and cutting test.

Table 31. Confirmation tests fitness values.

Confirmation Tests Fitness Value			
	MRR+AvgFxy+Ra	**MRR+AvgFxy**	**MRR+Ra**
Test No.	*1*	*2*	*3*
Fitness Value	**2.37**	**1.20**	**1.82**

4.3.2. Tool Wear and Burr Formation Results Discussion. The confirmation cutting results have shown that the cutting parameters have been optimized for machining productivity. However, there is a need to study the tool wear and burr formation from these confirmation tests. The confirmation test are invalid if excessive tool wear or burrs are observed because they indicate tool failure and loss of machining productivity.

The tool wear mechanisms found for the confirmation tests are shown in Figure 62. Experiment 1 experienced groove wear whereas experiment 2 and 3 experienced built up edge on the cutting tip. The BUE edge was more pronounced in experiment 3 than experiment 2. This is due to experiment 3 focusing on MRR+Ra and thus has a more aggressive machining strategy.

(a) Experiment 1: Groove Wear   **(b) Experiment 2: Built Up Edge**

(c) Experiment 3: Built Up Edge
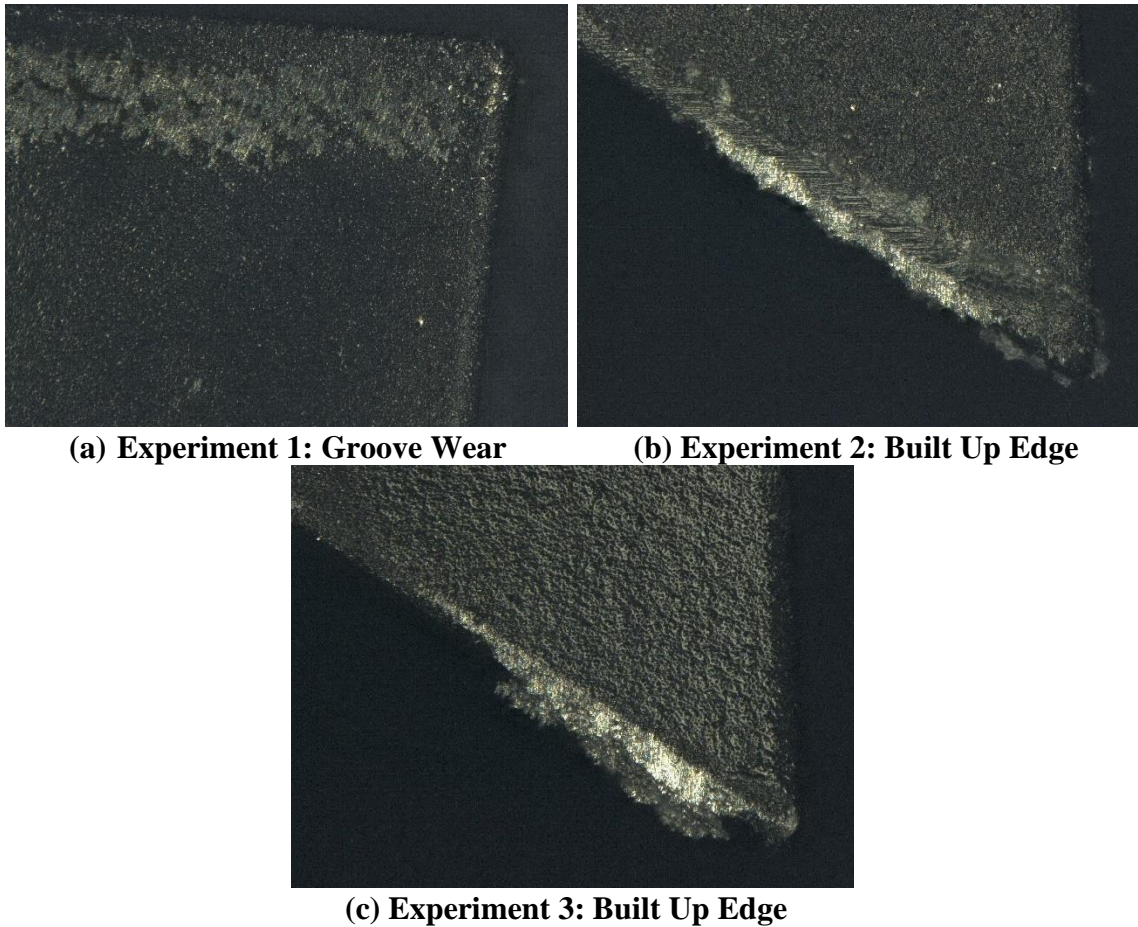
Figure 62. Confirmation tests tool wear mechanisms (a) groove wear (b)(c) built up edge.

The burr formation is an important feature to examine as burr removal is a non-productive and costly process. The surface topography of the $AlSiC_p$ was captured by the Keyence VHX-2000 Digital Microscope and is shown in Figure 63. These surface topographies show no burr formation. It can be concluded that these cutting conditions are viable options for creating larger products.

(a) Experiment 1　　　　　　　　　　　　　(b) Experiment 2
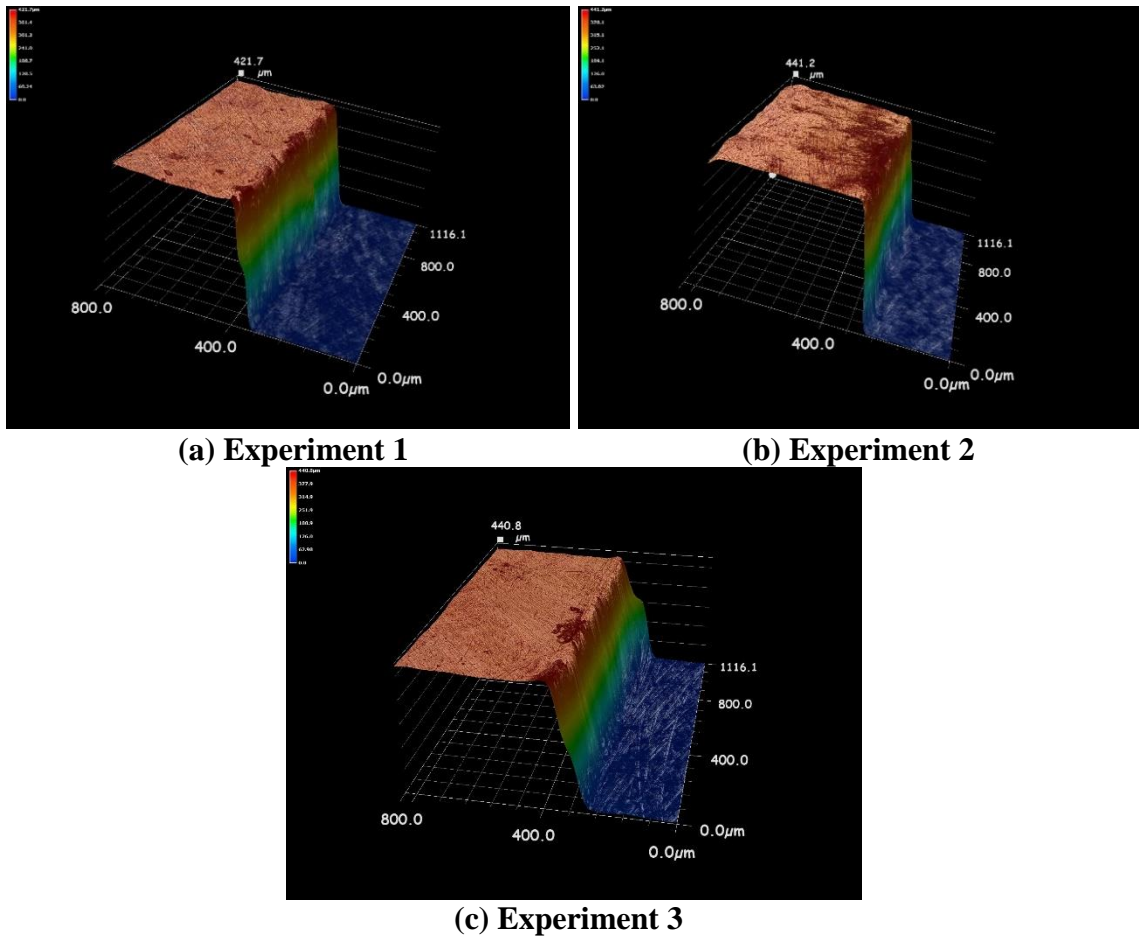
(c) Experiment 3

Figure 63. No burr formation found in all 3 confirmation experiments.

4.4. Endurance Tests

The endurance tests will focus on running the optimal cutting conditions found in the previous section. However, experiment 1 will be excluded from the endurance tests. It was concluded that because experiment 1 has a machining time that is 40 times longer than experiment 3, the cutting parameters would not be viable in the industry due to low machining productivity. Moreover, the recording of the cutting data is limited by the equipment, which would not be able to effectively capture the entire machining time of experiment 1.

4.4.1. Cutting Force Results Discussion. The cutting force for Fx, Fy, and Fxy

were averaged for each pass and is measured in terms of volume of removed material

(mm^3). The average cutting force results are shown in Figure 64. This plot shows the

exponential increase in average cutting forces as more material is removed. This correlates

with the amount of tool wear the CVD diamond coated end mills are experiencing.

However, this correlation did not entirely match up with observations during the

experiment. During the endurance tests, experiment 2 failed first before experiment 3.
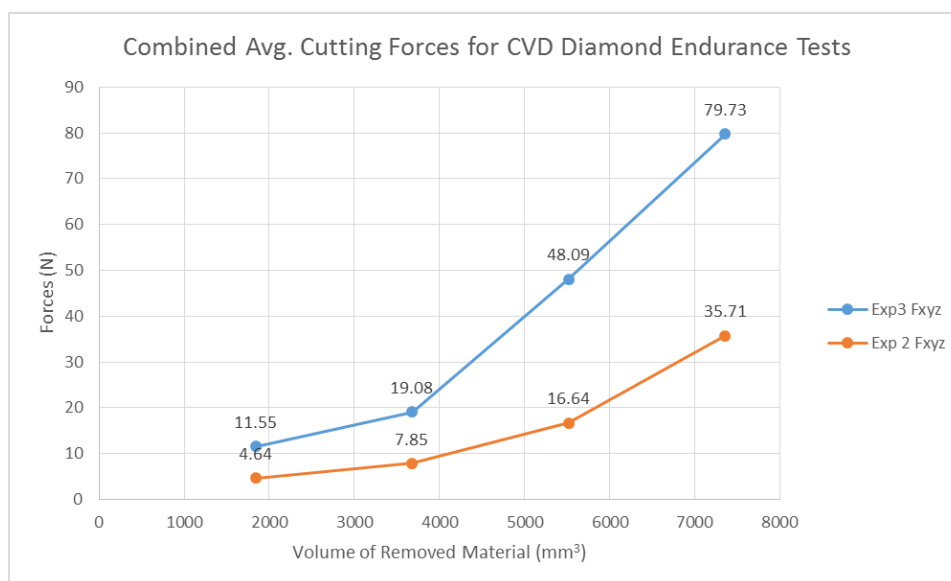
Figure 64. Average cutting forces for experiment 2 and 3 of endurance test.

In order to have a clearer representation of the tool wear development, the max

cutting forces must be examined. The max cutting forces can detail the rapid decline in tool

life due to the difficulty the cutting tool has with cutting the $AlSiC_p$. The max cutting forces

with respect to the volume of material removed is shown in Figure 65. In this graph, it is

clear that experiment 2 had a larger rate of tool wear and failed first. At the end of the

endurance tests, experiment 2 had a max cutting force of 769.44 N while experiment 3 had

a max cutting force of 743.53 N. One possible reason for this is because the machining time for experiment 2 was 5 times longer than experiment 3. This could lead to more cutting interaction time with the SiC particles and abrade the rake face of the CVD diamond coated end mills.
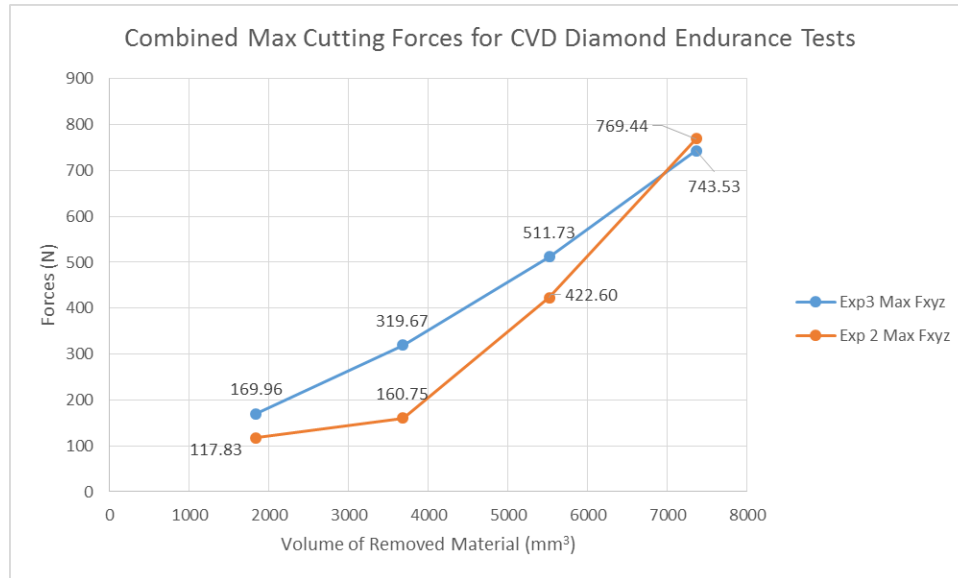
Figure 65. Max cutting forces for experiment 2 and 3 for endurance test.

4.4.2. Tool Wear and Burr Formation Results. The observation of tool wear and burr formation after the endurance tests is critical to understanding the dominant wear mechanisms and the feasibility of the cutting conditions. Figure 66a shows the tool damage produced after the endurance tests. The diamond coating was abraded away by the SiC particles and the carbide substrate is exposed. Moreover, the cutting tip shows signs of chipping and has been rounded. Figure 66b shows the burr formation on the edges of the AlSiC$_p$ block after the endurance tests.
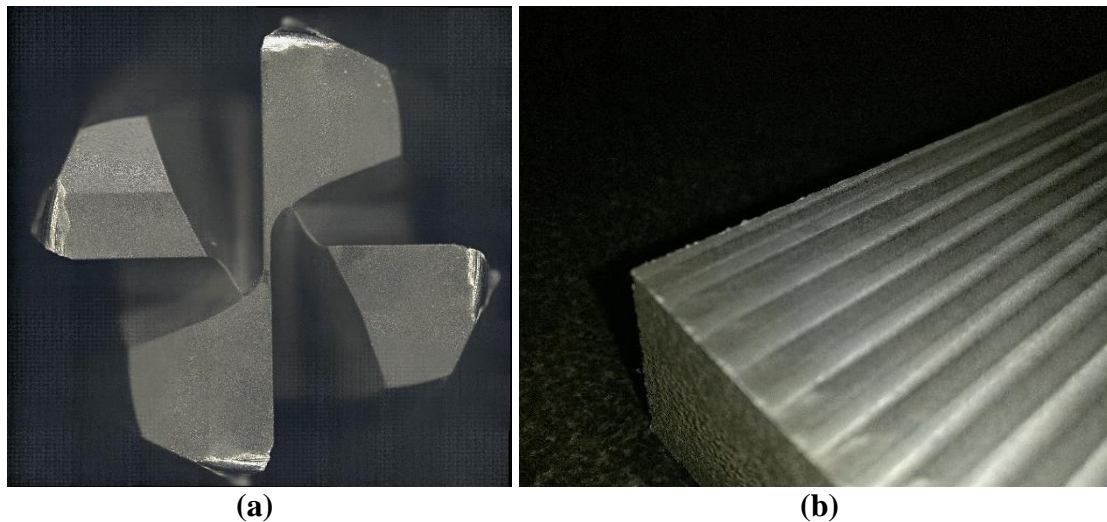
Figure 66. (a) CVD diamond coated end mill tool damage (b) AlSiC$_p$ burr formation after endurance test.

4.4.3. Tool Wear Development Discussion. The tool wear development is a critical factor when analyzing the improvement of tool life. The tool wear development from experiment 2 and 3 are compared to previous research to show the improvement of trochoidal milling under wet cutting conditions, as shown in Figure 67. The CVD diamond coated end mills have nearly half as much tool wear developed as previous research. Previous research had a tool wear of 0.151 mm^2, while this research had 0.092 mm^2 and 0.065 mm^2 of tool wear for experiments 2 and 3, respectively. Moreover, previous research had excessive tool coating delamination, while this research had gradual delamination of the diamond coating. The higher tool wear from experiment 2 correlates with the early tool failure found during the endurance tests. This is due to the longer machining time from experiment 2.

(a) Exp. 2: Tool Wear 0.092 mm^2　　　　(b) Exp. 3: Tool Wear 0.065 mm^2

(c) Prior Research: Tool Wear 0.151 mm^2
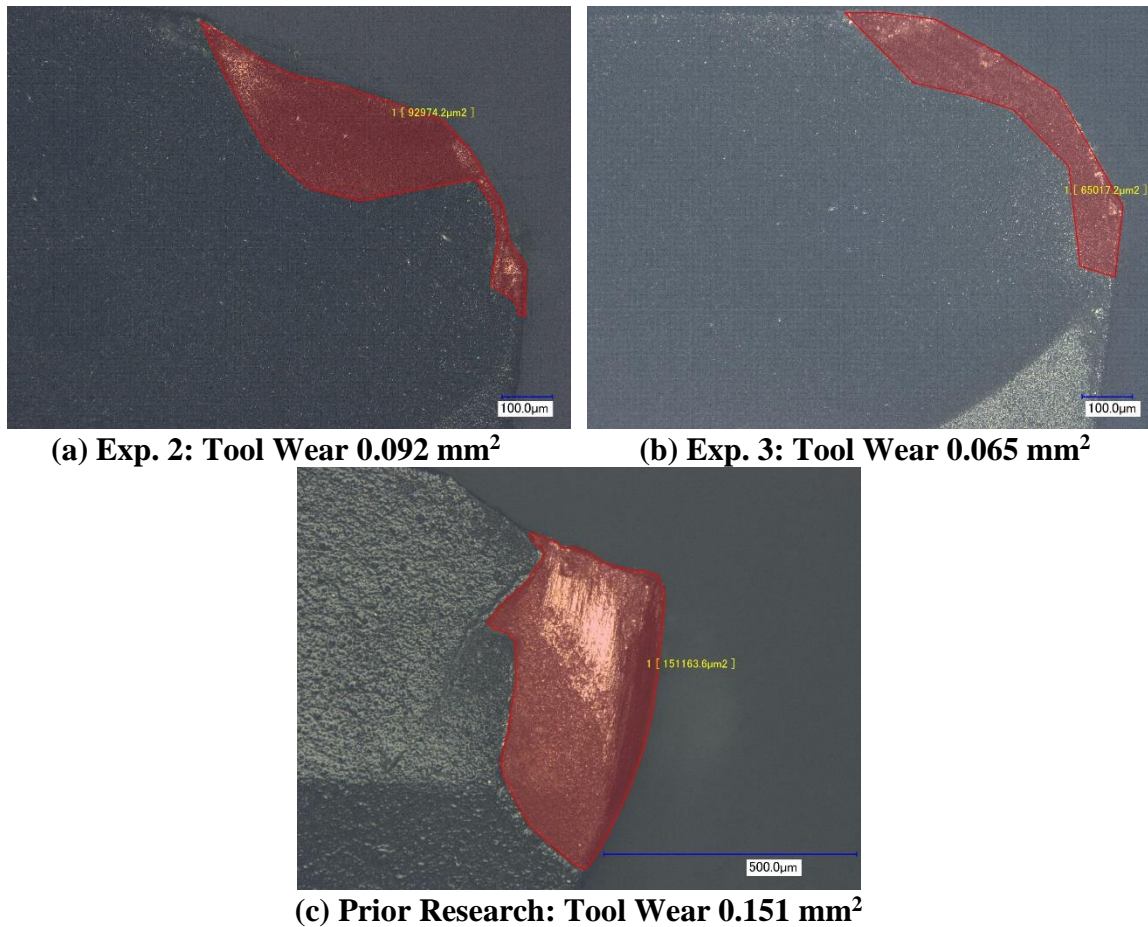
Figure 67. Tool wear development from experiments 2 and 3 compared to previous research.

4.4.4. Tool Damage Discussion. The tool damage represents the tool wear developed on the CVD diamond coated end mills, as well as the material that was lost due to chipping. In order measure the tool damage, an approximation can be made to find where the cutting tip used to be and measure the total area that was damaged by the SiC particles. The results are shown in Figure 68. Previous research was shown to have tool damage of 0.181 mm^2 while experiments 2 and 3 had tool damage of 0.195 mm^2 and 0.126 mm^2. Experiment 2 was found to have a higher tool damage because it had a longer machining time. This allowed for more abrasive wear to occur on the cutting tool.
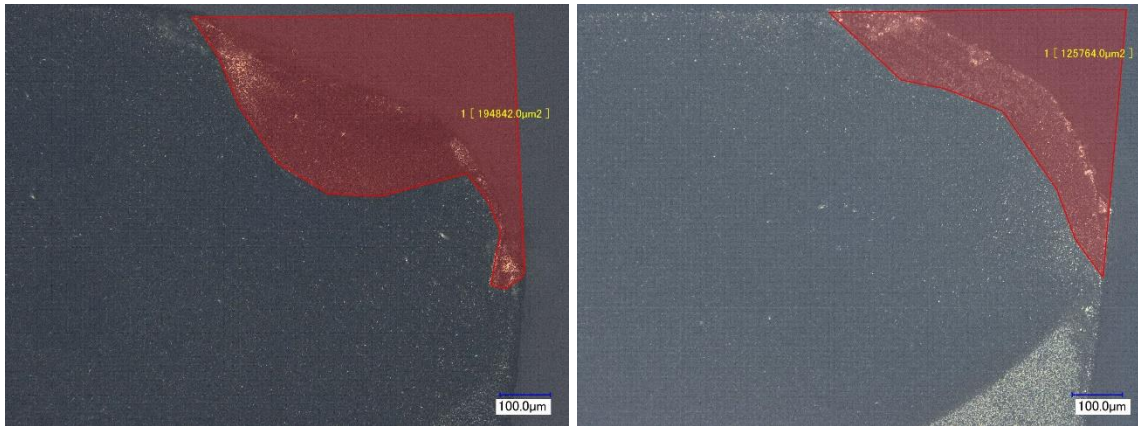
(a) Exp. 2: Tool Damage: 0.195 mm^2

(b) Exp. 3: Tool Damage: 0.126 mm^2
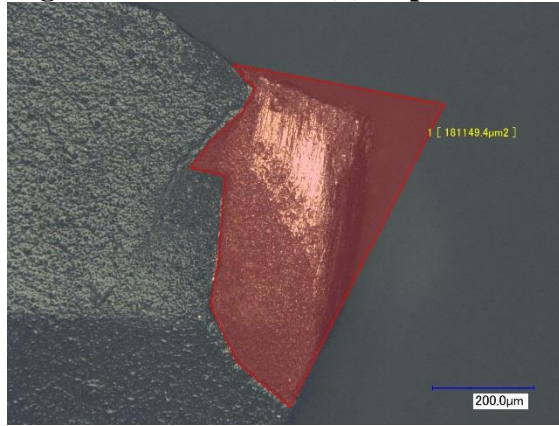
(c) Prior Research: Tool Damage: 0.181 mm^2

Figure 68. Tool damage from experiments 2 and 3 compared to previous research.

Chapter 5: Conclusion

5.1. Conclusions

The optimal cutting conditions were found to be 254 mm/min, 30°, and 9500 r/min for MRR+AvgFxy+Ra, 1524 mm/min, 30°, and 9500 r/min for MRR+AvgFxy, and 1524 mm/min, 90°, and 9500 r/min. However, the first set of cutting conditions were not considered because the machining productivity was too low to be considered in the industry. All cutting experiments had a low surface roughness value and had no burr formation. However, some tool wear mechanisms that were observed were the following: crater wear, built up edge, and groove wear. These tool wear mechanisms are mainly dependent on the interaction between the cutting tool and the SiC particles. It was confirmed that the longer the machining time, the more tool wear is developed. However, utilizing trochoidal milling under wet cutting conditions has proven to extend the tool life of CVD diamond coated end mills when compared to previous research. Trochoidal milling has shown to improve chip evacuation and maintain constant cutting temperatures and cutting forces. This led to a much slower development of tool wear.

5.2. Future Work

From this research, it could be concluded that square end mills is not an optimal tool geometry for machining AlSiC$_p$. Once tool wear develops on the cutting tip, the CVD diamond coated end mills were shown to chip away quickly. It may be beneficial to maintain a constant set of cutting parameters and vary the tool geometries instead. As an alternative, a ball end mill can be used to study the cutting interaction between the ball end mill's cutting edge and the SiC particles. The lack of a cutting tip could be promising for

tool life and make CVD diamond coated end mills a more viable option for machining high

volume fractions AlSiC$_p$.

REFERENCES

[1] Miracle, D. B., 2005, "Metal Matrix Composites – From Science to Technological Significance," Compos. Sci. Technol., **65**(15), pp. 2526–2540.

[2] Chawla, N., and Chawla, K. K., 2006, "Metal-Matrix Composites in Ground Transportation," JOM, **58**(11), pp. 67–70.

[3] Rawal, S. P., 2001, "Metal-Matrix Composites for Space Applications," JOM, **53**(4), pp. 14–17.

[4] Macke, A., Schultz, B., and Rohatgi, P. K., 2012, "Metal Matrix Composites Offer the Automotive Industry an Opportunity to Reduce Vehicle Weight, Improve Performance," Adv. Mater. Process., **170**, pp. 19–23.

[5] Pawar, P. B., and Utpat, A. A., 2014, "Development of Aluminium Based Silicon Carbide Particulate Metal Matrix Composite for Spur Gear," Procedia Mater. Sci., **6**, pp. 1150–1156.

[6] Zweben, C., 1998, "Advances in Composite Materials for Thermal Management in Electronic Packaging," JOM, **50**(6), pp. 47–51.

[7] Iwayama, I., Kuwabara, T., Nakai, Y., Ikeda, T., Koyama, S., and Okamoto, M., 2014, *New Heat Sink for Railroad Vehicle Power Modules*.

[8] Lee, H. S., Jeon, K. Y., Kim, H. Y., and Hong, S. H., 2000, "Fabrication Process and Thermal Properties of SiCp/Al Metal Matrix Composites for Electronic Packaging Applications," J. Mater. Sci., **35**(24), pp. 6231–6236.

[9] Mitic, G., Degischer, H. P., Lefranc, G., and Licht, T., 2000, "AlSiC Composite Materials in IGBT Power Modules," *Conference Record of the 2000 IEEE Industry Applications Conference. Thirty-Fifth IAS Annual Meeting and World Conference on Industrial Applications of Electrical Energy (Cat. No.00CH37129)*, pp. 3021–3027 vol.5.

[10] Färcaş, C., Ciocan, I., Petreuş, D., and Palaghiṫă, N., 2012, "Thermal Modeling and Analysis of a Power Device Heat Sinks," *2012 IEEE 18th International Symposium for Design and Technology in Electronic Packaging (SIITME)*, pp. 217–222.

[11] Bains, P. S., Sidhu, S. S., and Payal, H. S., 2016, "Fabrication and Machining of Metal Matrix Composites: A Review," Mater. Manuf. Process., **31**(5), pp. 553–573.

[12] Paulo Davim, J., and Monteiro Baptista, A., 2000, "Relationship between Cutting Force and PCD Cutting Tool Wear in Machining Silicon Carbide Reinforced Aluminium," J. Mater. Process. Technol., **103**(3), pp. 417–423.

[13] Ding, X., Liew, W. Y. H., and Liu, X. D., 2005, "Evaluation of Machining Performance of MMC with PCBN and PCD Tools," Wear, **259**(7), pp. 1225–1234.

[14] El-Gallab, M., and Sklad, M., 1998, "Machining of Al/SiC Particulate Metal-Matrix Composites: Part I: Tool Performance," J. Mater. Process. Technol., **83**(1), pp. 151–158.

[15] El-Gallab, M., and Sklad, M., 1998, "Machining of Al/SiC Particulate Metal Matrix Composites: Part II: Workpiece Surface Integrity," J. Mater. Process. Technol., **83**(1), pp. 277–285.

[16] Huang, S. T., Zhou, L., Yu, X. L., and Cui, Y., 2012, "Experimental Study of High-Speed Milling of SiCp/Al Composites with PCD Tools," Int. J. Adv. Manuf. Technol., **62**(5–8), pp. 487–493.

[17]   Vargas, A., Nguyen, T., and Liu, J., 2017, "Machinability Study on SiC Particle Reinforced Aluminum Alloy Composite (SiCp/Al) Material With CVD Diamond Coated End Mills," p. V002T02A003.

[18]   Patil, P., Polishetty, A., Goldberg, M., Littlefair, G., and Nomani, J., "SLOT MACHINING OF TI6AL4V WITH TROCHOIDAL MILLING TECHNIQUE," ResearchGate.

[19]   Foltz, J. V., and Blackmon, C. M., 1990, "Metal-Matrix Composites."

[20]   Chawla, N., and Shen, Y.-L., 2001, "Mechanical Behavior of Particle Reinforced Metal Matrix Composites," Adv. Eng. Mater., **3**(6), pp. 357–370.

[21]   Rahman, M. H., and Rashed, H. M. M. A., 2014, "Characterization of Silicon Carbide Reinforced Aluminum Matrix Composites," Procedia Eng., **90**(Supplement C), pp. 103–109.

[22]   Segurado, J., and LLorca, J., 2006, "Computational Micromechanics of Composites: The Effect of Particle Spatial Distribution," Mech. Mater., **38**(8), pp. 873–883.

[23]   Soltani, S., Khosroshahi, R. A., Mousavian, R. T., Jiang, Z.-Y., Boostani, A. F., and Brabazon, D., 2017, "Stir Casting Process for Manufacture of Al–SiC Composites," Rare Met., **36**(7), pp. 581–590.

[24]   Übeyli, M., Balci, E., Sarikan, B., Öztaş, M. K., Camuşcu, N., Yildirim, R. O., and Keleş, Ö., 2014, "The Ballistic Performance of SiC–AA7075 Functionally Graded Composite Produced by Powder Metallurgy," Mater. Des. 1980-2015, **56**(Supplement C), pp. 31–36.

[25]   Erdemir, F., Canakci, A., and Varol, T., 2015, "Microstructural Characterization and Mechanical Properties of Functionally Graded Al2024/SiC Composites Prepared by Powder Metallurgy Techniques," Trans. Nonferrous Met. Soc. China, **25**(11), pp. 3569–3577.

[26]   Bodukuri, A. K., Eswaraiah, K., Rajendar, K., and Sampath, V., 2016, "Fabrication of Al–SiC–B4C Metal Matrix Composite by Powder Metallurgy Technique and Evaluating Mechanical Properties," Perspect. Sci., **8**(Supplement C), pp. 428–431.

[27]   Canakci, A., and Varol, T., 2014, "Microstructure and Properties of AA7075/Al–SiC Composites Fabricated Using Powder Metallurgy and Hot Pressing," Powder Technol., **268**(Supplement C), pp. 72–79.

[28]   Yao, X., Zhang, Z., Zheng, Y. F., Kong, C., Quadir, M. Z., Liang, J. M., Chen, Y. H., Munroe, P., and Zhang, D. L., 2017, "Effects of SiC Nanoparticle Content on the Microstructure and Tensile Mechanical Properties of Ultrafine Grained AA6063-SiCnp Nanocomposites Fabricated by Powder Metallurgy," J. Mater. Sci. Technol., **33**(9), pp. 1023–1030.

[29]   Assar, A.-E. M., 1999, "Fabrication of Metal Matrix Composite by Infiltration Process—part 2: Experimental Study," J. Mater. Process. Technol., **86**(1), pp. 152–158.

[30]   Beffort, O., Long, S., Cayron, C., Kuebler, J., and Buffat, P.-A., 2007, "Alloying Effects on Microstructure and Mechanical Properties of High Volume Fraction SiC-Particle Reinforced Al-MMCs Made by Squeeze Casting Infiltration," Compos. Sci. Technol., **67**(3), pp. 737–745.

[31] Long, S., Beffort, O., Moret, G., and Thevoz, P., 2000, *Processing of Al-Based MMCs by Indirect Squeeze Infiltration of Ceramic Preforms on a Shot Control High Pressure Die Casting Machine*.

[32] Wannasin, J., and Flemings, M. C., 2005, "Fabrication of Metal Matrix Composites by a High-Pressure Centrifugal Infiltration Process," J. Mater. Process. Technol., **169**(2), pp. 143–149.

[33] Hashim, J., Looney, L., and Hashmi, M. S. J., 1999, "Metal Matrix Composites: Production by the Stir Casting Method," J. Mater. Process. Technol., **92**, pp. 1–7.

[34] Hashim, J., Looney, L., and Hashmi, M. S. J., 2002, "Particle Distribution in Cast Metal Matrix Composites—Part I," J. Mater. Process. Technol., **123**(2), pp. 251–257.

[35] Sijo, M. T., and Jayadevan, K. R., 2016, "Analysis of Stir Cast Aluminium Silicon Carbide Metal Matrix Composite: A Comprehensive Review," Procedia Technol., **24**(Supplement C), pp. 379–385.

[36] Moses, J. J., Dinaharan, I., and Sekhar, S. J., 2014, "Characterization of Silicon Carbide Particulate Reinforced AA6061 Aluminum Alloy Composites Produced via Stir Casting," Procedia Mater. Sci., **5**(Supplement C), pp. 106–112.

[37] Arokiadass, R., Palaniradja, K., and Alagumoorthi, N., 2012, "Prediction and Optimization of End Milling Process Parameters of Cast Aluminium Based MMC," Trans. Nonferrous Met. Soc. China, **22**(7), pp. 1568–1574.

[38] Kannan, S., Kishawy, H. A., and Deiab, I., 2009, "Cutting Forces and TEM Analysis of the Generated Surface during Machining Metal Matrix Composites," J. Mater. Process. Technol., **209**(5), pp. 2260–2269.

[39] Li, X., and Seah, W. K. H., 2001, "Tool Wear Acceleration in Relation to Workpiece Reinforcement Percentage in Cutting of Metal Matrix Composites," Wear, **247**(2), pp. 161–171.

[40] Manna, A., and Bhattacharayya, B., 2003, "A Study on Machinability of Al/SiC-MMC," J. Mater. Process. Technol., **140**(1), pp. 711–716.

[41] Coelho, R. T., Yamada, S., Aspinwall, D. K., and Wise, M. L. H., 1995, "The Application of Polycrystalline Diamond (PCD) Tool Materials When Drilling and Reaming Aluminium Based Alloys Including MMC," Int. J. Mach. Tools Manuf., **35**(5), pp. 761–774.

[42] Ozben, T., Kilickap, E., and Çakır, O., 2008, "Investigation of Mechanical and Machinability Properties of SiC Particle Reinforced Al-MMC," J. Mater. Process. Technol., **198**(1), pp. 220–225.

[43] Davim, J. P., 2007, "Application of Merchant Theory in Machining Particulate Metal Matrix Composites," Mater. Des., **28**(10), pp. 2684–2687.

[44] Pramanik, A., Zhang, L. C., and Arsecularatne, J. A., 2006, "Prediction of Cutting Forces in Machining of Metal Matrix Composites," Int. J. Mach. Tools Manuf., **46**(14), pp. 1795–1803.

[45] Kök, M., Kanca, E., and Eyercioğlu, Ö., 2011, "Prediction of Surface Roughness in Abrasive Waterjet Machining of Particle Reinforced MMCs Using Genetic Expression Programming," Int. J. Adv. Manuf. Technol., **55**(9–12), pp. 955–968.

[46] Müller, F., and Monaghan, J., 2000, "Non-Conventional Machining of Particle Reinforced Metal Matrix Composite," Int. J. Mach. Tools Manuf., **40**(9), pp. 1351–1366.

[47] Hamatani, G., and Ramulu, M., 1990, "Machinability of High Temperature Composites by Abrasive Waterjet," J. Eng. Mater. Technol., **112**(4), pp. 381–386.

[48] Ho, K. H., and Newman, S. T., 2003, "State of the Art Electrical Discharge Machining (EDM)," Int. J. Mach. Tools Manuf., **43**(13), pp. 1287–1300.

[49] Singh, P. N., Raghukandan, K., Rathinasabapathi, M., and Pai, B. C., 2004, "Electric Discharge Machining of Al–10%SiCP As-Cast Metal Matrix Composites," J. Mater. Process. Technol., **155–156**, pp. 1653–1657.

[50] Przestacki, D., 2014, "Conventional and Laser Assisted Machining of Composite A359/20SiCp," Procedia CIRP, **14**, pp. 229–233.

[51] Otkur, M., and Lazoglu, I., 2007, "Trochoidal Milling," Int. J. Mach. Tools Manuf., **47**(9), pp. 1324–1332.

[52] Heikkala, J., 1995, "Determining of Cutting-Force Components in Face Milling," J. Mater. Process. Technol., **52**(1), pp. 1–8.

[53] Pleta, A., Ulutan, D., and Mears, L., 2014, "Investigation of Trochoidal Milling in Nickel-Based Superalloy Inconel 738 and Comparison With End Milling," p. V002T02A058.

[54] Pleta, A., Ulutan, D., and Mears, L., 2015, "An Investigation of Alternative Path Planning Strategies for Machining of Nickel-Based Superalloys," Procedia Manuf., **1**, pp. 556–566.

[55] Bian, R., He, N., Li, L., Zhan, Z. B., Wu, Q., and Shi, Z. Y., 2014, "Precision Milling of High Volume Fraction SiC<Subscript>p</Subscript>/Al Composites with Monocrystalline Diamond End Mill," Int. J. Adv. Manuf. Technol., **71**(1–4), pp. 411–419.

[56] Radhakrishnan, P., Subramanyan, S., and Raju, V., 2008, *CAD/CAM/CIM*, New Age International Pvt. Ltd., Publishers, Daryaganj, INDIA.

[57] Lai W.-H., 2000, "Modeling of Cutting Forces in End Milling Operations," 淡江理工學刊, **3**(1), pp. 15–22.

[58] Polishetty, A., Goldberg, M., Littlefair, G., Puttaraju, M., Patil, P., and Kalra, A., 2014, "A Preliminary Assessment of Machinability of Titanium Alloy Ti 6AL 4V During Thin Wall Machining Using Trochoidal Milling," Procedia Eng., **97**, pp. 357–364.

[59] Ibaraki, S., Yamaji, I., and Matsubara, A., 2010, "On the Removal of Critical Cutting Regions by Trochoidal Grooving," Precis. Eng., **34**(3), pp. 467–473.

[60] Shixiong, W., Wei, M., Bin, L., and Chengyong, W., 2016, "Trochoidal Machining for the High-Speed Milling of Pockets," J. Mater. Process. Technol., **233**, pp. 29–43.

[61] Zhao, W., Wang, S., Han, Z., and He, N., 2015, "Cutting Performance Evaluation of End Mills for Titanium Aircraft Components," Procedia CIRP, **35**, pp. 1–7.

[62] Szalóki, I., 2012, "Can Trochoidal Milling Be Ideal?," p. .

[63] Gradišek, J., Kalveram, M., and Weinert, K., 2004, "Mechanistic Identification of Specific Force Coefficients for a General End Mill," Int. J. Mach. Tools Manuf., **44**(4), pp. 401–414.

[64] Pramanik, A., Zhang, L. C., and Arsecularatne, J. A., 2007, "An FEM Investigation into the Behavior of Metal Matrix Composites: Tool–particle Interaction during Orthogonal Cutting," Int. J. Mach. Tools Manuf., **47**(10), pp. 1497–1506.

[65] Davim, J. P., Silva, J., and Baptista, A. M., 2007, "Experimental Cutting Model of Metal Matrix Composites (MMCs)," J. Mater. Process. Technol., **183**(2), pp. 358–362.

[66]   Umer, U., Ashfaq, M., Qudeiri, J. A., Hussein, H. M. A., Danish, S. N., and Al-Ahmari, A. R., 2015, "Modeling Machining of Particle-Reinforced Aluminum-Based Metal Matrix Composites Using Cohesive Zone Elements," Int. J. Adv. Manuf. Technol., **78**(5–8), pp. 1171–1179.

[67]   Bakša, T., Kroupa, T., Hanzl, P., and Zetek, M., 2015, "Durability of Cutting Tools during Machining of Very Hard and Solid Materials," Procedia Eng., **100**, pp. 1414–1423.

[68]   Davim, J. P., 2002, "Diamond Tool Performance in Machining Metal–matrix Composites," J. Mater. Process. Technol., **128**(1), pp. 100–105.

[69]   Durante, S., Rutelli, G., and Rabezzana, F., 1997, "Aluminum-Based MMC Machining with Diamond-Coated Cutting Tools," Surf. Coat. Technol., **94**–**95**, pp. 632–640.

[70]   Liu, J., and Camfield, R., 2015, "Machinability Experimental Study of Sintered Alumina (Al2O3) Ceramics Material by Chemical Vapor Deposition Diamond Coating Milling Tools," Proc. Inst. Mech. Eng. Part B J. Eng. Manuf., **229**(9), pp. 1535–1546.

[71]   Andrewes, C. J. E., Feng, H.-Y., and Lau, W. M., 2000, "Machining of an Aluminum/SiC Composite Using Diamond Inserts," J. Mater. Process. Technol., **102**(1), pp. 25–29.

[72]   Chou, Y. K., and Liu, J., 2005, "CVD Diamond Tool Performance in Metal Matrix Composite Machining," Surf. Coat. Technol., **200**(5), pp. 1872–1878.

[73]   Davim, J. P., and Mata, F., 2008, "Chemical Vapour Deposition (CVD) Diamond Coated Tools Performance in Machining of PEEK Composites," Mater. Des., **29**(8), pp. 1568–1574.

[74]   Creighton, J. R., and Ho, P., 2001, "Introduction to Chemical Vapor Deposition (CVD)," Chem. Vap. Depos., **2**, pp. 1–22.

[75]   Qin, F., Chou, Y. K., Nolen, D., and Thompson, R. G., 2009, "Coating Thickness Effects on Diamond Coated Cutting Tools," Surf. Coat. Technol., **204**(6), pp. 1056–1060.

[76]   Vogtel, P., Klocke, F., and Lung, D., 2014, "High Performance Machining of Profiled Slots in Nickel-Based-Superalloys," Procedia CIRP, **14**, pp. 54–59.

[77]   Kumar, S., and Sahai, R., "(9) An Overview on Taguchi Method," ResearchGate.